# Asteroseismic modeling of delta Scuti stars: The cases of 44 Tau and HD 187547

Janne Højmark Mønster, 201405523
Aarhus University, Department of Physics and Astronomy

September 7, 2019

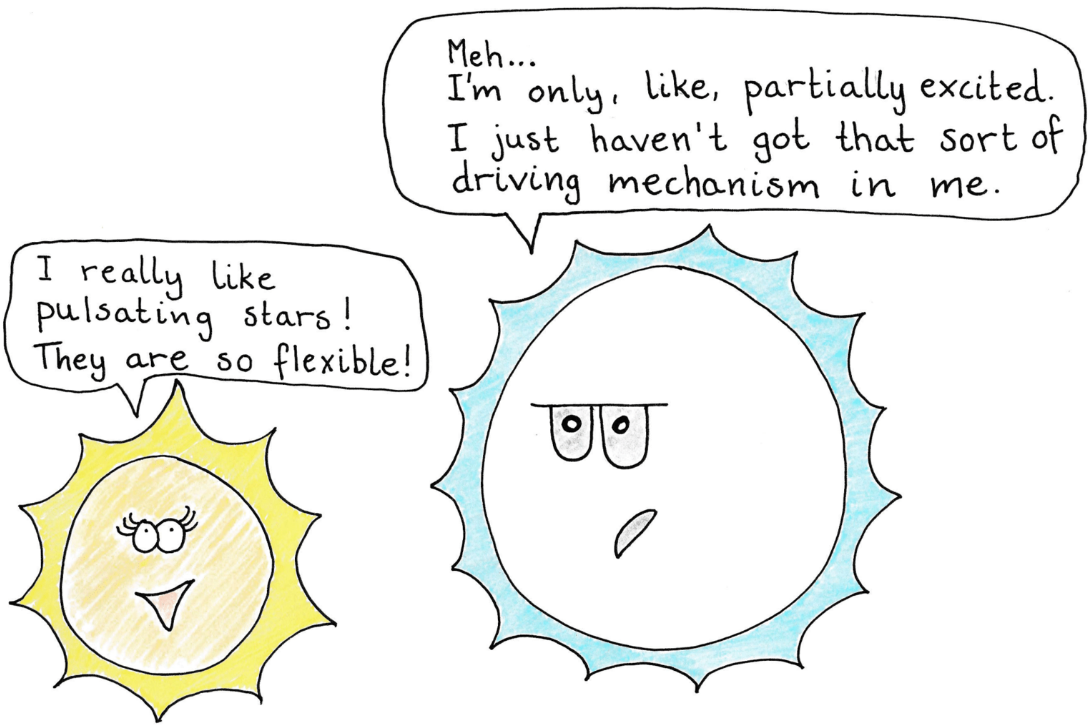

## Abstract

The $\delta$ Sct stars 44 Tau and HD 187547 are investigated through asteroseismic modeling with the aim to determine their evolutionary stages. Several multisite campaigns have been carried out for 44 Tau, which led to successful modeling of all modes. HD 187547 has also been observed, resulting in an estimated large frequency separation of $\Delta\nu = 3.5d^{-1}$. This star has an unusual pulsation pattern that is not yet understood. Modeling is needed in order to understand the processes in the star.

A grid of ∼1000 tracks is constructed using the stellar structure and evolution code `MESA`. The pulsations along the tracks are calculated with the pulsation code `GYRE`. For all tracks, the observed frequencies, effective temperature, surface gravity, and luminosity are compared to the theoretically produced values. Two different runs are carried out for HD 187547, to investigate whether the estimate of the large frequency separation of $\Delta\nu = 3.5d^{-1}$ is potentially the double value $\Delta\nu = 7d^{-1}$.

The results for 44 tau places it on the post-main sequence after hydrogen exhaustion. This is at a later stage than previous modeling has shown. However, the analysis conducted here has not taken mode identification into account and further investigation is needed to ensure that the frequencies are weighted correctly. For HD 187547 the results indicates that the star is a early to middle stage of the main sequence. For $\Delta\nu = 3.5d^{-1}$ the resulting best model is outside of the regime of $\delta$ Sct pulsations, contrary to the best model for $\Delta\nu = 7d^{-1}$. This suggests that the estimate of $3.5d^{-1}$ is too low to agree with the low measured luminosity measurements by the GAIA mission, and that the star is younger than previously anticipated.

# Acknowledgements

First and foremost, I would like to express my sincere gratitude to the people who have helped me through my research, making this thesis possible. A very special thanks my co-supervisor Victoria Antoci, who not only opened my eyes to the exciting field of asteroseismology, but made the project entirely possible. She has guided me to become a better researcher, and this thesis is a product of that. Also a big thanks to my main supervisor Günter Houdek who helped me during the enormous task of grasping the concepts behind numerical simulations and the theory of stellar structure and evolution.

I am also extremely grateful for the help provided by Earl Bellinger, without whom I would have probably still been stuck in a forloop. His knowledge in computer science has helped me on countless occasions to increase my coding skills. Thanks to Kuldeep Verma and Jakob Lysgaard Rørsted for helping me understand the complicated mystery of the computational tools used in this project. To Rasmus Handberg for always being ready to help and discuss the best ways of implementing the $\chi^2$, and to Amalie Louise who always takes her time to help with anything that needs helping.

This research would not have been carried out without the help of my office mates who have lend an ear to many frustrated hours of writing, coding and reattempting. Thanks to Simon Banerjee for always being ready to discuss problems, to Rasmus Lind Bjerre for putting a smile back onto my face when I was struggling and to Dorte Thrige Plauborg who has been my rock to lean on throughout the entire process. Finally, I wish to thank all my friends and my family for the support and understanding I have received. A heartfelt thanks to my boyfriend Emil Christensen who always kept understanding, supporting and loving me.

# Contents

# 1 Introduction

The field of astronomy is one of the oldest sciences in the world, attempting to answer any question on the universe an the celestial bodies within it. Throughout the years it has developed into several theoretical and observational branches studying every corner of the universe from the nearest objects such as the moon an the Sun to the very edges of the universe that are so far away that the human brain cannot grasp the sheer size of it. Since the early studies to present day, astronomy has developed substantially, yet many questions remain still unanswered. What does the universe consist of? How old is the universe? Why are we able to exist here on Earth? Some of these may not be answered ever, yet curiosity drives humans to continue researching.

One of the major components in the universe is the stars. New stars are born from the "ashes" of dead stars and learning how they are formed, evolve and die is fundamental for understanding the environment they evolve in. Such studies are within the field of *Stellar Structure and Evolution*. Describing the different type of stars is an immense task in itself and dividing them into categories and understanding them requires us to understand the processes that leads to differences in their stellar structures. The problem with this is, however, that the insides of stars is unreachable from an observational point of view. We cannot simply look inside the stars, and for a long time penetrating the barriers of stellar layers seemed unobtainable.

Records on observations of pulsating stars goes back nearly 500 years. It was not until 1980's that we fully understood the potential of pulsations. At his point, the field of *asteroseismology* was introduced by Christensen-Dalsgaard (1984) as "The science of using stellar oscillations for the study of the properties of stars, including their internal structure and dynamics". The term "asteroseismology" was however coined by Gough (1996).

The closest (and therefore most studied) star is the Sun. Knowledge provided from the Sun can be projected to other types of stars, and *helioseismology* (asteroseismology of the Sun) has provided valuable research in the field of Stellar Structure and Evolution. However, helioseismology is not yet developed enough to the reach the deepest layers of the Sun. Therefore, we need to turn to other types of stars and exploit their pulsational advantages to reveal the secrets inside the stars.

Before computers were invented, every observation and calculation were done analytically, which was a very time consuming task. However, we are now at a time where stellar evolution can calculated fully numerically and results compared to the expected parameters derived from observations. Stellar structure and evolution codes can further provide calculations of the pulsations in a star with a stellar pulsation code. This is crucial for stellar modeling as the pulsation frequencies acts as an additional constraint to the parameter space, and can help identify the processes inside pulsating stars, and thereby obtain knowledge on the pulsation mechanism, structure, convection, and evolutionary stage.

In this work the method of asteroseismic modeling is applied to two different $\delta$ Sct stars, 44 Tau and 187547. 44 Tau has already been modeled which led to and estimate of the evolutionary stage. By using a similar method in this work the procedure can further be applied to HD 187547. Asteroseismic modeling is particularly needed for this star since it represents some of the issues with the theory behind $\delta$ Sct stars. The goal of the asteroseismic modeling in this work is ultimately to analyze how well theory matches observations and using the results to discuss the remaining issues in the field and optimize the methods for any future work. The work can be utilized on other types of stars, so a deeper understanding of stellar structure and evolution in general can be achieved. Hence, we get one step closer to understanding one of the most fundamental parts of the universe.

The work is structured as follows: Chap. 2 gives an introduction to Stellar structure and evolution related to this work. Relevant numerical results are presented to demonstrate key aspects of the field. Chap. 3 introduces the theory behind asteroseismology, and how it can be applied to various types of star, depending on the structure of the star. In Chap. 4 the $\delta$ Sct stars are described in more detail with the focus being on their importance from an asteroseismic and modeling point of view. Specifically, the asteroseismic and observational background of 44 Tau and hd 187547 are introduced. The tools used for modeling these star are presented in Chap. 5, where the Stellar Structure and Evolution code `MESA` and Stellar Pulsation code `GYRE` and their main numerical aspects are presented. Chap. 6 described the entire process of modeling the stars and the methods applied to compare to observations. Main results and proposed future work is then discussed in Chap. 7 and final conclusions are given in Chap. 8.

This work has made use of data from the European Space Agency (ESA) mission Gaia (`https://www.cosmos.esa.int/gaia`), processed by the Gaia Data Processing and Analysis Consortium (DPAC, `https://www.cosmos.esa.int/web/gaia/dpac/consortium`). Funding for the DPAC has been provided by national institutions, in particular the institutions participating in the Gaia Multilateral Agreement.

# 2 Stellar Structure and Evolution

The field of stellar structure and evolution is wide and it is possible to study numerous aspects of it. In this section, a brief introduction to the theory of stellar structure and evolution is given. This is based on mainly Christensen-Dalsgaard (2008b) and Kippenhahn et al. (1990).

It is difficult to paint a general picture of a "star". There are numerous types of stars, varying in observable properties such as magnitude and effective temperature, but also indirect properties such as their inner structures. Assumptions and simplifications are therefore necessary in order to give a comprehensible representation of a star. First, and foremost, a star is always assumed to be in *hydrostatic equilibrium*, meaning that physics on a macroscopic level adapts to the surroundings on a timescale much faster than the *free-fall time* (i.e. the time it takes until the interstellar cloud has contracted to a single point. The star is also assumed to have none or little rotation such that it can be treated as spherically symmetric. Magnetic fields are commonly assumed to not be present in the star. These assumption are of course very crude, as we know that stars do indeed rotate and have magnetic fields. However, the assumptions provides us the possibility to give a rough estimate on the conditions in a star.

A star in hydrostatic equilibrium balances its own gravitation with the gas pressure. By looking at an infinitesimal small mass element $dm$ at a distance $r$ from the center, one can derive

$$\frac{dP}{dr} = -\frac{GM(r)}{r^2}\rho \tag{2.1}$$

where $G$ is the gravitational constant and $P$ is the pressure. This equation states that the pressure obtained from gas and radiation must be equal to that of gravitation in order to maintain hydrostatic equilibrium. A star is also assumed to follow the equation of mass-conservation

$$\frac{dM(r)}{dr} = 4\pi r^2 \rho, \tag{2.2}$$

where $M(r)$ is the mass of a spherical shell of radius $r$. Combining the two equations yields

$$-\frac{dP}{dM(r)} = \frac{G}{4\pi}\frac{M(r)}{r^4}. \tag{2.3}$$

From these equations it is possible to derive expressions for the minimum value of the central pressure $P_c$, the mean pressure $\tilde{P}$ and temperature $\tilde{T}$ for the case of a homogeneous star. Here, no knowledge on the composition is required, only the mass distribution.

The energy in a star is defined by the energy creation (and loss) in a certain layer. The conservation is then defined

$$\frac{dL}{dM(r)} = \eta = \eta_{nuc} - \eta_{\nu} - T\frac{\partial s}{\partial T}, \tag{2.4}$$

where $\eta_{nuc}$ is nuclear energy generation rate, $\eta_{\nu}$ is the neutrino loss rate and $T\frac{\partial s}{\partial T}$ is the gravitational energy rate describing energy that is released or absorbed by the contraction or expansion of the star. The energy can be transported through radiation. The temperature gradient required to carry the entire luminosity of a star by radiation can be written as

$$\frac{dT}{dr} = -\frac{3\rho}{64\pi^2\sigma}\frac{\kappa L}{r^4T^3}, \tag{2.5}$$

also called the equation of radiative transport. Here L is the luminosity, $\kappa$ is the opacity, $\rho$ is the density and $\sigma$ is the Stefan-Boltzmann constant. This equation is valid as long a the *diffusion approximation* is valid. This breaks down at the stellar surface. In this case the full, and much more complicated, equations of radiative transfer must be solved.

For a more thorough description of stellar structure, the properties of the matter need to be assessed. Describing the thermodynamical properties in detail is no simple task, but the fundamental assumption is that at any point in the star, the gas is assumed to be in *thermodynamic equilibrium*, which means that there are no net macroscopic flows. This approximation ensures that instead of considering detailed reactions between particles, the average properties of the gas can be described by local state variables. The relations between these specifies the *equation of state* (EOS) of the gas. It is also assumed that there is no change in the gas conditions over the distance of the mean-free-path of a particle located in the gas, or over the time between collisions. These assumptions are well applied in stellar interiors, but in order to describe conditions in the atmosphere, a more detailed description is needed.

Since temperatures in the interiors are high, most of the gas will be fully ionized, and thereby have no internal degrees of freedom. Interactions b (collisions) between particles can be neglected, hence the gas is an approximate *ideal gas* following the ideal-gas law

$$PV = Nk_BT, \tag{2.6}$$

where $N$ is the number of particles in a gas with volume V, and $k_B$ is Boltzmann's constant. From this, general relations between pressure and internal energy can be derived. Stellar structure and evolution solves both equations of hydrostatic equilibrium and the EOS of the star. The modules used in this project will be described in Chap. 5.

## 2.1 Energy transport by convection

When deriving the equations and variables for a star, it is usually assumed that the star can be treated as being spherically symmetric. In reality though, there will be fluctuations on small scales that has to be taken into account. The most considered of these instabilities or fluctuations is *convection.* These can be treated as small perturbations.

Convection can be described as macroscopic mass elements or "bubbles" that transports energy in a star. Elements that are hotter than their surroundings rises upwards carrying excess thermal energy. The displacement of the element grows exponentially and when the velocity becomes too large, nonlinear effects causes the thermal energy to be released into the surroundings. Thus, convection contributes by transporting energy, and mixing the gas elements. This has large consequences for the stellar evolution as we shall see in Sec. 5.

Whether a region in a star is stable against convection depends on whether the perturbation is allowed to grow under certain conditions. Therefore, it is a matter of *convective instability*. Assuming that the mass elements do not exchange energy with the surroundings (during movement), and therefore moves adiabatically, it can be derived that

$$\nabla < \nabla_e + \frac{\phi}{\delta}\nabla_\mu, \tag{2.7}$$

describing the condition for convective stability. Here

$$\nabla \equiv \left(\frac{d\ln T}{d\ln P}\right)_s, \qquad \nabla_e \equiv \left(\frac{\partial \ln T}{\partial \ln P}\right)_e, \qquad \nabla_\mu \equiv \left(\frac{\partial \ln \mu}{\partial \ln P}\right)_s. \tag{2.8}$$

Here, the subscript $e$ means that the derivative is in relation to the element, whereas $s$ is the surrounding material. For the case where energy is transported by radiation or conduction only

$$\nabla_{rad} \equiv \left(\frac{d\ln T}{d\ln P}\right)_{rad}, \tag{2.9}$$

temperature variation is described with depth. In a layer where all energy transport is either radiation or conduction, $\nabla = \nabla_{rad}$. Also, assuming that the element moves adiabatically such that

$$\nabla_e = \nabla_{ad} \equiv \left(\frac{\partial \ln T}{\partial \ln P}\right)_{ad} \tag{2.10}$$

and inserting in Eq. 2.7, one arrives at

$$\nabla_{rad} < \nabla_{ad} + \frac{\phi}{\delta}\nabla_\mu, \tag{2.11}$$

known as the *Ledoux criterion*. Under the assumptions mentioned earlier, this is the criteria for dynamical stability. It can be simplified further by assuming that the chemical composition is homogeneous such that $\mu$ is constant. This yields the *Schwarzschild criterion* on the simple form:

$$\nabla_{rad} < \nabla_{ad}. \tag{2.12}$$

This assumption does not apply well to evolving stars where elements are not necessarily produced in the same layer (as heavier elements are produced below lighter). Instability to convection thus occurs when the left hand side becomes larger than the right hand side. The small perturbations will grow until the layers is filled with convection. This occurs if

- $L(r)/m(r)$, (the energy generation rate per unit mass within radius $r$) is large. In massive stars, this rate is an increasing function of temperature, thus increasing $L/m$ towards the center. Therefore these stars have convective cores.

- $\rho/T$ is large. Since $\rho/T^3$ increases rapidly in the photosphere, this usually occurs in cooler stars.

- The opacity $\kappa$ is large. Stars with low surface temperatures usually have higher $\kappa$ in the outer layers.

- $\nabla_{ad}$ is small. This happens in ionization zones.

To sum up, the first condition consequently allows for convection in the core of massive stars. The remaining conditions for outer layers of cooler stars. The different possibilities for the structures are illustrated on Fig. 2.1.

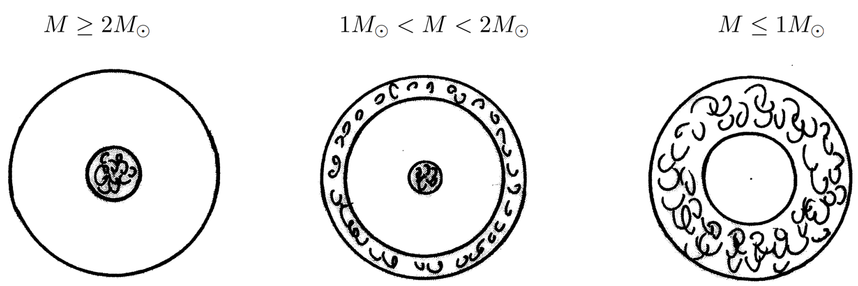


Figure 2.1: Estimated occurrence of convection zones in main-sequence stars with different masses. Stars with masses higher than $2\ M_\odot$ have fully convective cores and only a very thin convective shell. Less massive stars with masses below $1M_\odot$ have deep convective envelopes. The stars in between marks the transition between the two. They have convective cores and a thin convective outer layer.

The stars in this project lies in the *intermediate mass* range which is usually stars of masses between $1.5M_\odot$ and $2.2M_\odot$. They cover the transition from deep convective envelopes and convective cores. The motivation for using such stars will be discussed further in Sec. 4.2.

If Eq. 2.11 leads to stability it follows that $\nabla = \nabla_{rad}$ for the entire layer. The last possibility is that one of Eq. 2.11 and Eq. 2.12 says stability whereas the other says instability. This is called the Twilight zone, see (Kippenhahn et al., 1990) for more details.

This prescription gives a very simplified picture of where convection is expected to occur within a star. However, in reality a local treatment is complicated since convective motion is not only dependent on local forces, but forces between layers as well (such as momentum and inertia). The border of a convective zone is thereby not well-defined and precise as elements accelerated from one layer might flow into another. This will be discussed further in

Sec. 5.1.3. Convection flows in the laboratory is relatively well described by reasonable approximations. However, in stars convection is happening in much more violent conditions where compression of gas and turbulent motion depends on density, pressure and gravity of very high orders. Taking such effects into consideration is not simple by any means, but efforts have been made to implement convection by making full two- and three-dimensional hydro dynamical simulations (e.g. Nordlund & Stein (1990)). Such codes do not treat the convection as separate homogeneous bubbles, but as a fully coupled time-dependent system. Such codes give a much more detailed and realistic picture of convection for single models. However, since the computation time for the full convective solution of a model is much longer than a simplified version, calculating a full track is not yet feasible. Therefore, the most used method is the *standard mixing length theory* (Weiss et al., 2004), which is a time-independent assessment. This is not sufficient to describe full hydrodynamical convection, but allows approximations to give a simplified local treatment, where convection can be described as macroscopic mass elements transferring energy. The mean free path is described with *the mixing length.* There are several ways to implement this in stellar modeling which will be described in Sec. 5.1.3.

## 2.2 Numerical results for stellar evolution through the HR-diagram

This section describes the evolution of a star through numerically calculated stellar evolutionary tracks, mainly focusing on the main sequence (ms)) and immediate post-main sequence (pms) phases of intermediate mass stars

Stars are born from molecular clouds, collapsing under their own gravity. When the cloud reaches a the *Jeans Mass*, the *Jeans Criterion* is fulfilled, meaning that any perturbation will cause a free-fall collapse. This continues while the process happens isothermally until the free-fall time becomes similar to the timescale for thermal adjustment. The process then becomes adiabatic, stopping the rapid dynamical contraction and leaving behind a *protostar* in hydrostatic equilibrium. Due to their low internal temperature and high opacity, these stars are fully convective. Thereby they are born on the *Hayashi Track* where the contraction continues. This track is the beginning of the *pre-main sequence phase.* As the star contracts and descends on the Hayashi track, the surface temperature (or effective temperature) is essentially constant while the luminosity decreases. The star heats up from the inside out since gas escapes the outer layers more easily. As the center becomes hotter, the opacity decreases and the convection zone slowly recedes. The star then leaves the Hayashi track and proceeds a radiative contraction on *the Henyey track.* This causes the decreasing luminosity trend to reverse and the star becomes more luminous. Eventually the core temperatures will be sufficiently high to trigger the proton-proton reaction, converting H into deuterium ($^2$H) and thereafter $^3$He.[1]

[1] The full proton-proton chain is not yet completed since the temperature is still too low to burn hydrogen in full equilibrium.

As a result, a convective core is created. This will however disappear if the mass of the star is below $1.1M_\odot$, whereas stars of higher mass will burn hydrogen in the cores through the *CNO-cycle*. Accretion of mass continues on the PMS phase on a thermal timescale. Stars of masses larger than $9M_\odot$ moves so quickly into the MS phase that they are unobservable on the PMS due to the thick shell of accreting mass, while stars of masses between 1.6-$9M_\odot$ end their accretion of mass on the PMS. When the star begins burning hydrogen in full hydrostatic equilibrium it is born onto the *zero-age main-sequence* (ZAMS). Stars below $0.08M_\odot$ never reaches ZAMS because their internal central temperature never becomes high enough to fuse hydrogen to helium in equilibrium. Instead they become degenerate, and are known as *brown dwarfs*. Although stellar pulsations in brown dwarfs were theoretically predicted by Palla & Baraffe (2005) these pulsations have not yet been detected (Aerts et al., 2010; Cody & Hillenbrand, 2014).

The ZAMS is where the star begins the life on the main-sequence where it spends 90 % of its life burning H to He. The computed solutions from this stage on can be seen on Fig. 2.2. The main sequence corresponding to the hydrogen burning in the core is defined as the phase between point 1 and 2. For all stars, the luminosity increases during this phase. The reason for this is that the hydrogen is converted into helium which causes the mean molecular weight to increase, which can be seen from

$$\mu \simeq \frac{4}{3 + 5\mathrm{X} - \mathrm{Z}}, \tag{2.13}$$

where X, Y and Z is the hydrogen, helium and metal fraction respectively. It follows form the ideal gas law that $\mathrm{P} \propto \rho\mathrm{T}$. The pressure must balance the weight of the overlaying layers, hence it cannot decrease. Instead, $\rho T$ compensates for the increase in $\mu$. The core will start contracting to increase $\rho$ and gravitational potential energy energy is released, which further causes an increase in T (from the Virial theorem[2]. As the opacity follows $\kappa \propto \mathrm{T}^{-3.5}$, an increase in temperature will cause a decrease in opacity. Thus, the photons can escape more easily, and the luminosity increases. This also follows from the equation of radiative transport Eq. 2.5 where $L \propto 1/\kappa$.

It is more complicated to explain the change in global parameters such as the effective temperature and radius. The radius increases in general as the star evolves, but the rate of this expansion is mass dependent. For stars that have low masses (close to $1M_\odot$) expansion is slow and the increase in luminosity will lead to an increase in the effective temperature as well, while it is the opposite for stars with higher masses and higher expansion rates. Since the star heats from the inside, the outer layers will have expanded before the temperature can increase in this region, hence the effective temperature decreases.

When hydrogen abundance get sufficiently low in the core, the star reaches the *terminal-age main-sequence* (TAMS). Here, the core now consists of helium. For intermediate mass stars,a noticeable feature is the "hook" following the ms,

[2]See Chapter 3 in Kippenhahn et al. (1990)

also known as the *Henyey Hook* (not to be confused with the Henyey track). This is clearly depicted on Fig. 2.3 As these type of stars have convective cores, the energy production will decrease uniformly throughout the core. The star will attempt to compensate for this by increasing the central temperature and keep the energy production up, hence causing the core to contract. As a result of the contraction, gravitational potential energy is released, where half is converted to thermal energy, heating up the core and essentially shifting the evolution to higher effective temperatures. This phase is in the order of a few megayears, which is extremely fast evolution compared to the main sequence (in the order of $10^{10}$ yrs. Therefore, studying a star in this exact phase is very difficult since a star can only be verified to be in this phase through modeling, as observations in color-magnitude diagrams cannot resolve it. From now on this will be referred to as the *post main-sequence contraction phase*. At this point most of the energy production still comes from nuclear reactions, and the gravitational contribution is small in comparison. It is surrounded by a region where temperature is still high enough to burn hydrogen, and slowly establishes a *shell source*. This will however not be dominant until all hydrogen is exhausted. When this happens at point 3 on Fig. 2.2, the evolution is accelerated and the star is no longer in thermal equilibrium. The contracting core will thus be accompanied by an expanding envelope, causing the effective temperature to decrease. This phase will be referred to as the *post- main sequence expansion phase*. The outer convection zone deepens until is reaches the layers where nuclear fusion has occurred (the core). This is marked as point 5 and is also called *first dredge up*.

At point 5-6 , the star will then move back up the Hyashi track as a red giant. The further evolution from then is largely depending on the mass. Stars with masses between 0.5<M<2.3$M_\odot$ (relevant for this work) will have a degenerate helium core by the end of the main sequence (the exact cutoff depends on the initial metallicity in the star). The core contraction following the main-sequence continues until it reaches a temperature high enough to ignite helium in the core through the triple $\alpha$ process. A thermal runaway known as *helium-flash* occurs and lifts the degeneracy of the helium core, settling the star down on the *horizontal branch* where it burns helium in the core and hydrogen in a shell (for stars with M<2.0$M_\odot$). Stars with masses below 4-8$M_\odot$ finish nuclear burning at carbon or oxygen. By the end, their envelopes will be ejected into space through stellar winds, forming planetary nebulae. Left behind is the remnant, a white dwarf star.

It has been shown how a star's luminosity changes as a function of effective temperature throughout its evolution. As mentioned in the beginning of the chapter, assumptions on hydrostatic equilibrium and equation of state can provide us with solutions that relates several other properties. The numerical solutions to the radius $R$, surface gravity $g$, core density $\rho$ and convective core mass are shown on Fig. 2.4 as a function of time. The red vertical lines from left to right indicate the beginning of the MS, post-MS contraction and post-MS expansion phases. As for the radius, the star contracts for the entirety of the PMS. As it burns hydrogen on the MS it slowly expands (as the temperature in the core increases slightly with time) until the post-MS where it again contracts.

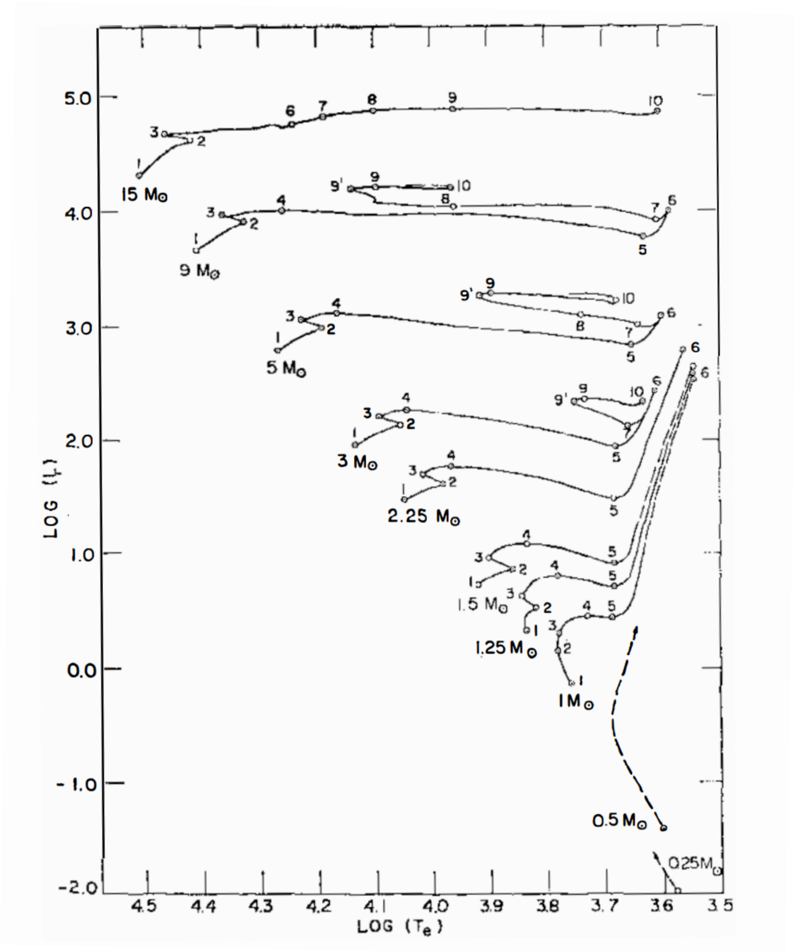

Figure 2.2: (Kippenhahn et al., 1990) Stellar evolution tracks of masses ranging from $0.25M_{\odot}$ to $15M_{\odot}$. The numbers indicate different stages in the evolution. Figure from Iben Jr (1967).

After hydrogen exhaustion the star undergoes fast overall expansion. Another parameter which is highly relevant for the frequencies is the surface gravity, as we shall see in Sec. 3. From theory we know that $g \propto M/R^2$, which is equivalent to the numerical results shown on Fig. 2.4. The density in the center increases rapidly on the Hyashi track when the star contracts, and follows the linear tendency $\rho_c \propto \frac{3M}{\pi R^3}$ on the MS (by assuming $\rho$ is a linear function of the fractional radius $r$. At the immediate post-MS phase it increases again as the core contracts rapidly.

An important parameter to also look at is the mass of the convective core. On the Hyashi track, the star is fully convective as it contracts. As the star burns hydrogen, the convective core mass slowly decreases until the point where hydrogen is exhausted in the core. On Fig. 2.5, numerical results for the convective core mass ratio to the total stellar mass is plotted as a function of stellar age in Gyrs for tracks with different masses. It can here be seen that higher stellar masses leads to higher convective core masses. Since stars with

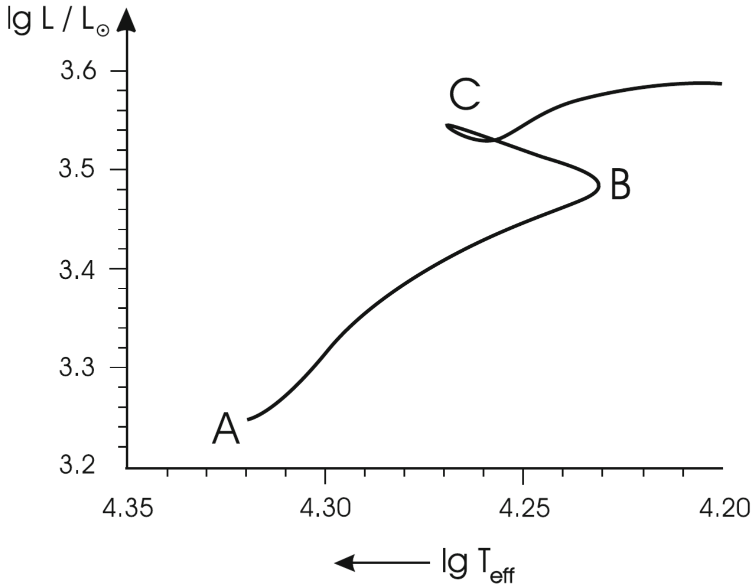


Figure 2.3: (Kippenhahn et al., 1990) Stellar evolution track of a $5M_\odot$ star. The main sequence is marked between A and B, the post-MS contraction from B to C and the post -MS expansion is after C. Figure from (Kippenhahn et al., 1990).

higher mass also have shorter lifetimes on the ms, which is also well-depicted on the figure as the convective core mass drops to zero when nuclear fusion in the core ends, which occurs sooner for higher masses. At this point, the core will not longer have high enough temperature to be convective. The smaller inset window on Fig. 2.5 shows the convective core mass evolution on the PMS to the MS. Higher masses enter the hyashi track at a lower age than stars with smaller masses again indicating a faster evolution in general.

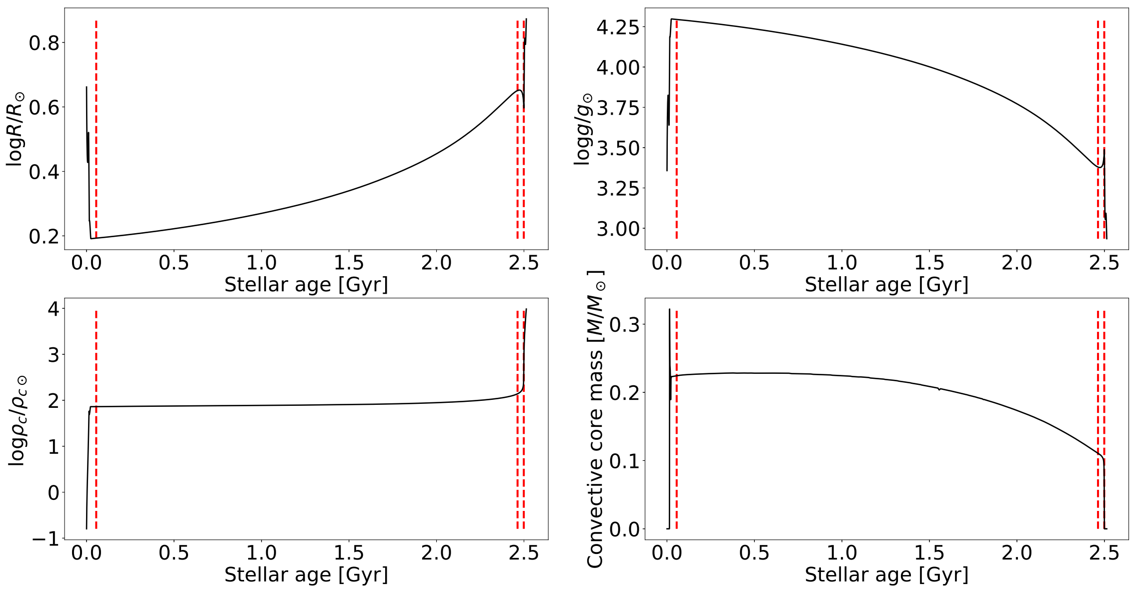


Figure 2.4: Numerically calculated stellar parameters for a track with $1.75M_\odot$, X=0.75, Z=0.02, $\alpha_{mlt}$=0.5, $\alpha_{ov}$=0.3. The dashed lines marks the different stages of the evolution, leftmost being thew beginning of the main-sequence, middle one the post- MS contraction phase and rightmost the post-MS expansion phase.

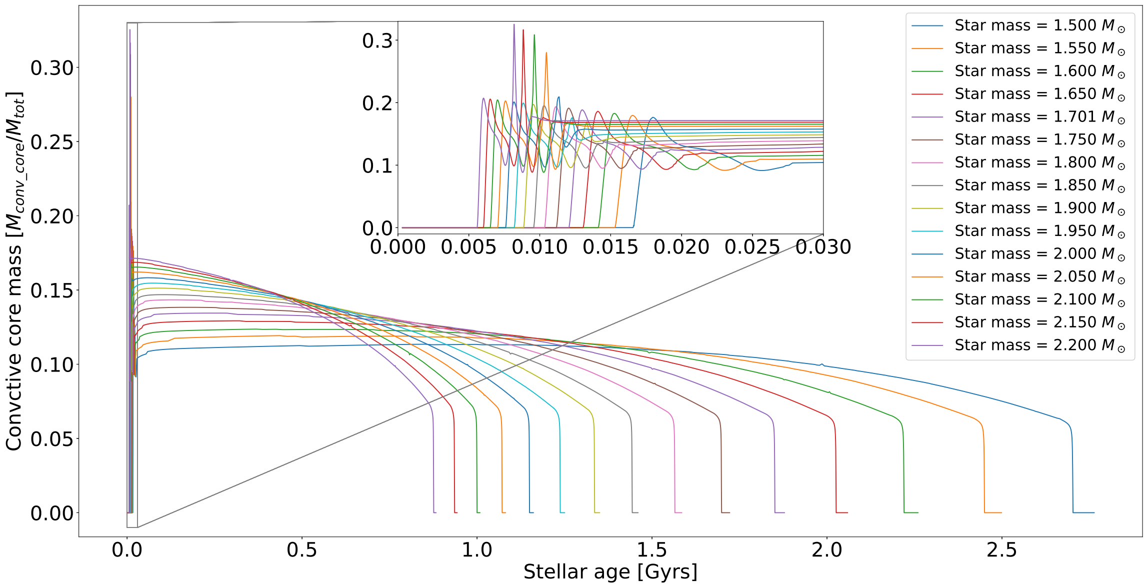


Figure 2.5: Numerical results for stars with masses ranging from $1.5M_\odot$ to $2.2M_\odot$, X = 0.70, Z = 0.02, $\alpha_{mlt} = 0.5$ and $\alpha_{ov} = 0.3$. The convective core mass ratio is plotted as a function of stellar age. The small window shows a zoom in of the plot at the age where the convective core is established (on the ms)

# 3 An introduction to asteroseismology

All stars are different in temperature, radius, luminosity, density and mass. Some stars also have *pulsations*, meaning that their luminosities vary in certain periods. The field of asteroseismology exploits these stellar pulsations in a star to look inside it and determine the inner structure. There are several types of pulsations depending on particularly the mass. In this chapter, a brief introduction to key aspects in the theory of stellar pulsations are given.

Pulsating stars contract and expands periodically, causing brightness changes that can be observed using two methods. Periodic brightness and thereby temperature variations causes variations in luminosity which can be measured with photometry. Changes in the velocity fields due to periodic changes in the luminosity gives rise to an observable Doppler effect which can be measured using spectroscopy. The outcome of the observations are time-series that can be converted to oscillation spectra through a fourier transform. The oscillation spectra can be analyzed to identify the nature of each frequency. Modeling the star can then reproduce the environment in the star, specifically the sound speed which changes according to the temperature and chemical composition. Therefore, comparing these theoretically produced frequencies with observations allows us to estimate the properties of the star.

## 3.1 Stellar pulsations

Pulsations in stars are treated three-dimensionally, and usually assumes a spherical symmetry of the star (which is true when rotation of the star is so small that the distortion of the stellar symmetry is negligible and the spherical harmonics still apply, see Eq. 3.4). The three directions for which the natural oscillation modes have nodes are described by the distance to the center of the star, $r$, co-latitude $\theta$ (measured from pulsation pole) and longitude $\phi$. Nodes are defined as concentric shells of constant r, cones of constant $\theta$ and finally planes of constant $\theta$. We can then describe the displacement in the ($r$,$\theta$,$\phi$) space as the following

$$\xi_r(r,\theta,\phi,t) = a(r)Y_l^m(\theta,\phi)e^{-i2\pi\nu t} \tag{3.1}$$

$$\xi_\Theta(r,\theta,\phi,t) = b(r)\frac{\partial Y_l^m(\theta,\phi)}{\partial\theta}e^{-i2\pi\nu t} \tag{3.2}$$

$$\xi_\Theta(r,\theta,\phi,t) = \frac{b(r)}{\sin(\theta)}\frac{\partial Y_l^m(\theta,\phi)}{\partial\phi}e^{-i2\pi\nu t}, \tag{3.3}$$

where $a(r)$ and $b(r)$ are the amplitudes, $\nu$ is the oscillation frequency (1/Period) and $Y_l^m(\theta,\phi)$ are the spherical harmonics given by

$$Y_l^m(\theta,\phi) = (-1)^m\sqrt{\frac{2l+1}{4\pi}\frac{(l-m)!}{(l+m)!}}P_l^m(\cos(\theta))e^{im\phi}, \tag{3.4}$$

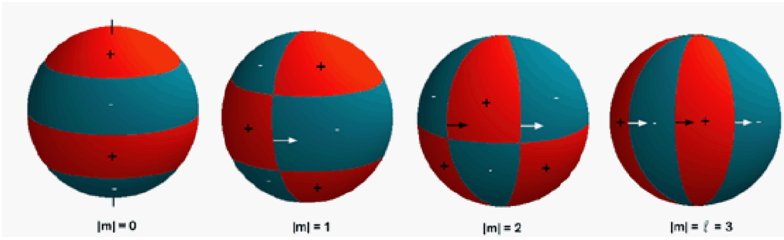


Figure 3.1: Possible geometrical nonradial pulsation patterns with $l$=3 for a spherically symmetric star. The '+' indicates areas that moves towards the observer, and the '-' away from the observer. (Antoci et al., 2011) (adapted from Wolfgang Zima 1999 master thesis.)

where $P_l^m(\cos(\theta))$ are the Legendre polynomials[1], with $l$ being the spherical degree and $m$ the azimuthal order . The normalization constant

$$c_{lm} \equiv \sqrt{\frac{2l+1}{4\pi}\frac{(l-m)!}{(l+m)!}}, \tag{3.5}$$

is defined such that the integral over the unit sphere of $|Y_l^m|^2 = 1$. Three quantum numbers describes the modes for 3-D stars, $n$,$l$ and $m$. $n$ is the *radial order* describing the number of radial nodes in the star. $l$ is the *spherical degree* and represents the total number of surface nodes; finally $m$ is the *azimuthal order* where $|m|$ is the number of longitudinal nodes, crossing the equator. It then follows that $l$-$|m|$ are the co-latitudinal nodes. $m$ can vary from $-l$ to $l$, yielding therefore a number of $2l+1$ different nodes for each spherical degree. An example of all geometrical possibilities of an $l = 3$ mode can be seen on Fig. 3.1.

Generally we can divide stellar pulsations into radial and non-radial pulsations. Radial pulsations is the case for which $l = 0$, with the very simplest geometry being the $n = 1$ or *radial fundamental mode*. In this case there is a node only at the center with the corresponding anti-node at the surface, meaning that the entire star pulsates. $n = 2$ is the first radial overtone with one node, $n = 3$ the second overtone has two radial nodes and so on. If we assume that the star is uniform in temperature and chemical composition we would expect the ratio between the fundamental mode and the first overtone to be similar to that of an organ pipe (Aerts et al., 2010). However, since we know that the temperature and chemical composition in the star changes with radius, we can exploit the fact that the sound speed changes accordingly, hence affecting the ratio. For instance we expect a ratio between the fundamental mode $F$ and first overtone $1H$ to be $F/1H = 0.77$ for $\delta$ Sct stars, but only $F/1H = 0.71$ for Cepheids (as they are slightly more evolved). Hence, we can already say something about the interiors based only on two observed

[1]see Aerts et al. (2010) for more details.

[1]These equations are introduced for the sole purpose of presenting the spherical harmonics. They will not be used for calculations during the project. For more details, see (Aerts et al., 2010).

frequencies. As for the non-radial modes, the *dipole* mode is the simplest with $l = 1$.

As mentioned earlier we have assumed that the star behaves symmetrically, and that for non-radial modes all $|m|$ values have the same frequency as the $|m| = 0$. However, it can cause the star to deviate from the assumption of spherical symmetry and lift this degeneracy such that all frequencies in $m$ for a given $l$ are different. The Coriolis and centrifugal forces will cause the wave to divert to either slightly lower or higher frequencies. Traveling with the rotation yields the *prograde* modes (lower frequencies), whereas traveling against rotation are *retrograde* modes (higher rotation)[2]. Assuming that the rotation still behaves uniformly we can write

$$\nu_{nlm} = \nu_{nl0} + m(1 - C_{nl})\Omega/2\pi, \tag{3.6}$$

where $\nu_{nlm}$ is the frequency, and $\nu_{nl0}$ is the unperturbed central frequency for which $m = 0$. The $m = 0$ mode is the same even with rotation. $\Omega$ is the angular velocity of the star and finally $C_{nl}$ is the Ledoux constant- calculated from models (Aerts et al., 2010), Sec. 2.8. The result from this is that we get a multiplet with $2l + 1$ components that is *rotationally split* by $(1 - C_{nl})\Omega/2\pi$. However, this approximation of a uniform rotation of the star is rather crude. In reality rotation is asymmetric and the rotational splittings depend on several properties of the mode. Also, the components in the multiplet could be excited to different amplitudes or some could not be excited[3]. This complicates the identification of the multiplets severely. However, we are nonetheless able to observe these rotational splittings which is very relevant for fast rotating stars.

### 3.1.1 Pressure and Gravity modes

Pulsations in stars can generally be divided into two groups: pressure modes (p modes) and gravity modes (g modes). The main difference between them is the restoring force in the two cases. For the p modes the pressure is the main restoring force when a star is perturbed from equilibrium, whereas the g modes have gravity as the restoring force. The difference between p modes and g modes is depicted on Fig. 3.2. It is also possible to observe stars that shows both types of modes and these are called *hybrids*. There is also a third option between p modes and g modes, which are the surface modes or f modes. These only exist for $l > 1$. All three types of modes are shown on Fig. 3.2 as a function of spherical degree $l$.

There are two characteristic frequencies that constrains the cavity in which modes can propagate. The first is the *Lamb frequency*, describing the inverse time needed to travel a horizontal wavelength with local adiabatic sound speed:

$$L_l^2 = \frac{l(l+1)c^2}{r^2}, \tag{3.7}$$

[2]The sign of the quantum number $m$ indicates whether the mode is prograde or retrograde, depending on the convention used.

[3]This depends on the driving mechanism. See Sec. 3.3

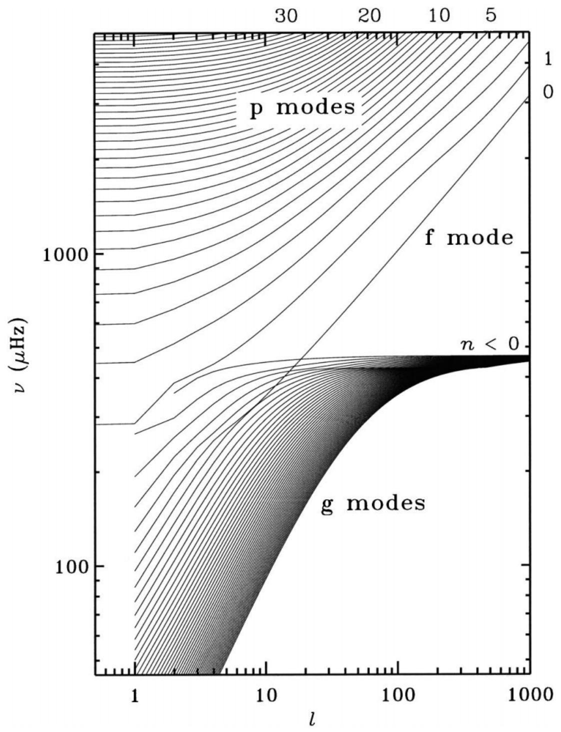


Figure 3.2: Frequencies of p and g modes for a solar model. For p modes, the frequency increases with overtone $n$ and spherical degree $l$. For g modes the it decreases with overtone. Lines are chosen to illustrate the modes for clarity, but is should be noted that individual modes are discrete points. Figure from Aerts et al. (2010).

with $l$ being the spherical degree and $c$ the adiabatic sound speed at radius $r$. The second frequency is the *Brunt-Väisälä frequency.* This is the frequency for which a fluid element oscillates around its equilibrium (vertically):

$$N^2 = g\left(\frac{1}{H} - \frac{g}{c^2}\right), \tag{3.8}$$

where $H$ is the density scale height and $g$ is the local gravity. Together these frequencies define cavities where a mode can oscillate:

- $\omega^2 > L_l^2$ and $\omega^2 > N^2$ where $\omega$ is the angular eigenfrequency of a mode. This region is situated in the outer layers of the star where the restoring force is pressure. Hence, oscillations in this area are the p modes.
- $\omega^2 < L_l^2$ and $\omega^2 < N^2$ is the cavity for which the restoring force is gravity, hence pulsation modes propagate as g modes.

Energy from modes are mainly distributed to layers where a pulsation can propagate, wheres outside the cavities the mode is *evanescent.* The Brunt-Väisälä (black line) and Lamb frequency (red line) region is depicted on Fig. 3.3 for a $1.9M_\odot$ model. Left panels show the propagation diagram for three different stages of the star that are depicted on the evolutionary track depicted on the right panels. In the propagation diagram the dimensionless frequency is plotted as a function of fractional radius. The p modes are located towards the surface of the star.

Mixed modes exists in the overlapping area of the p mode and g mode cavities. They act as g modes in the interior and p modes in the outer layers. As the star evolves, the modes change:

- The spacing between consecutive radial orders decreases as the star becomes more evolved.
- The cavity for g modes grows in frequency and radius space. I.e. more evolved stars have more g modes.
- The g mode cavity will overlap the p mode cavity more in evolved stars resulting in an increasing number of mixed modes.

Since the frequencies in a star depends very strongly on the environment,i.e structure, they can therefore act as a tracer for the evolutionary stage of the star.

We can also exploit that different pulsation modes penetrate to different layers of the stars. The depth to which a mode will penetrate to is determined by the spherical degree $l$. Fig. 3.4 shows that the different *ray paths* for different spherical degrees. Dashed lines indicate the turning point where the wave front will be diverted back to the surface. Here, the Lamb frequency is equal to the mode frequency. The wave is then reflected inwards again due to the drop in density in the outer layers. Besides from p modes being more sensitive to conditions in the outer layers and for g modes in the interior layers, there are two other important properties for p modes and g modes: 1) As the number of radial nodes increase, so will the frequencies of the p modes, whereas the frequencies for g modes will decrease. 2) for $n \gg l$ there is an asymptotic relation for p modes. This states that the modes are equally spaced in frequency. A similar relation exists for g modes, however stating that modes are equally spaced in period.

(Shibahashi, 1979) used asymptotic theory to calculate the frequencies of p modes as the following:

$$\nu_{n,l} = \Delta\nu \left( n + \frac{l}{2} + \widetilde{\alpha} \right) + \epsilon_{n,l}, \tag{3.9}$$

where $n$ and $l$ are the radial order and the spherical degree of the mode, $\widetilde{\alpha}$ is a constant of order unity, $\epsilon_{n,l}$ is a small correction and finally $\Delta\nu$ is the *large frequency separation.* This is the inverse of the sound travel time traveling from the surface to the core and back. It is given by:

$$\Delta\nu = \left( 2 \int_0^R \frac{dr}{c(r)} \right)^{-1} \tag{3.10}$$

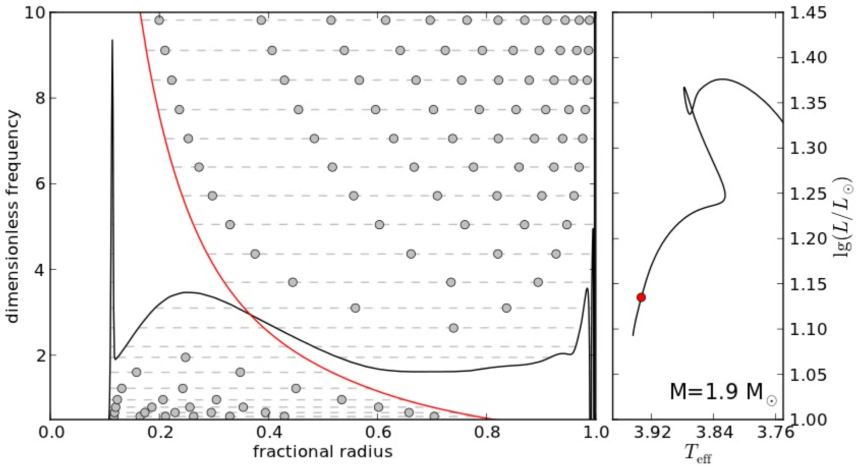


(a) Frequencies of p- and g modes on the MS.

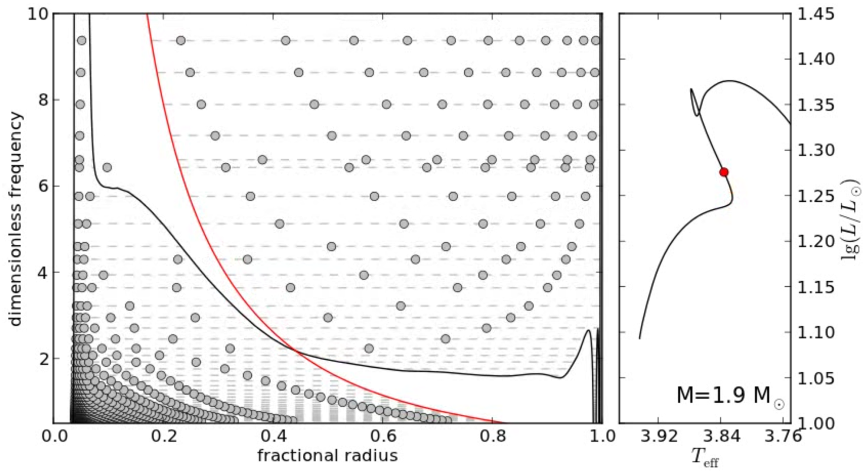


(b) Frequencies of p- and g modes on the post-MS contraction phase.

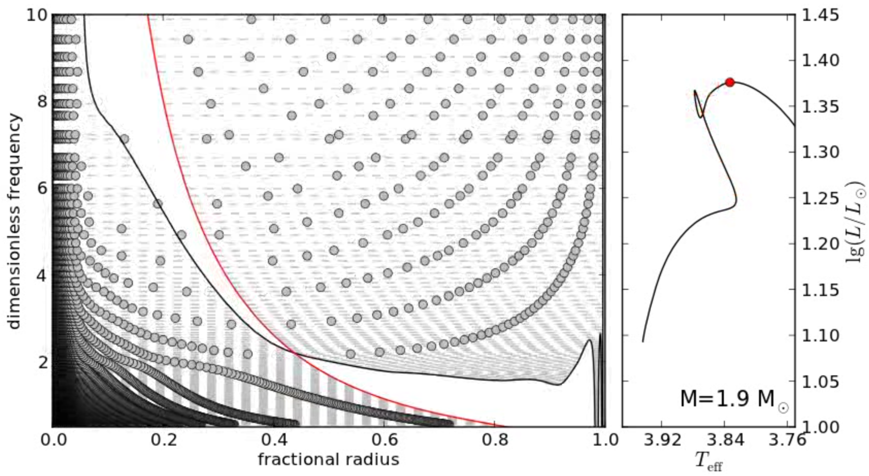


(c) Frequencies of p and g modes on the post-MS expansion phase.

Figure 3.3: Left panels shows the propagation diagrams of p and g modes in a 1.9 $M_\odot$ star as a function fractional radius (0.0 being the center). Right panels shows the evolutionary track for the corresponding propagation diagram, with the current stage marked with a black dot. Credit Patrick Lenz.

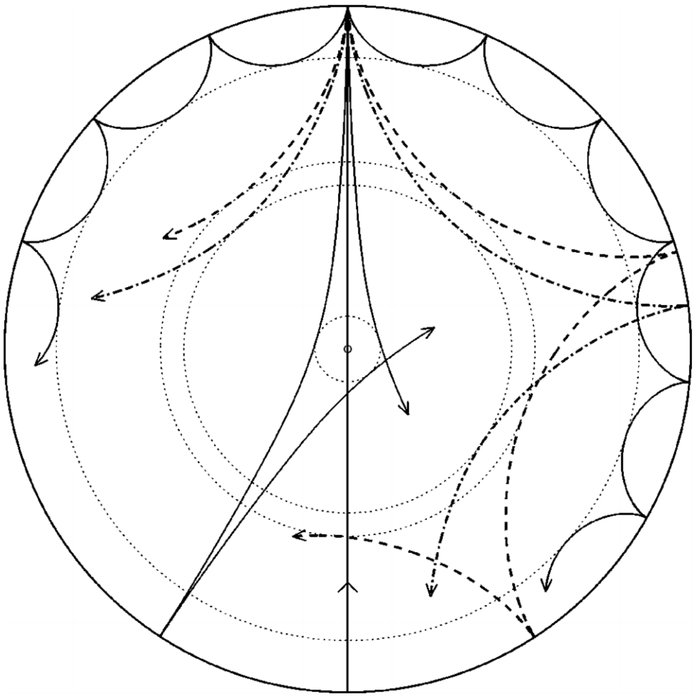

Figure 3.4: Schematic view of the propagating p modes in a star. The rays penetrate the star to a depth depending on the spherical degree, $l$. The ray reaches an point where it will turn around. This is due to the increasing sound speed with depth. After the turnaround, the star will eventually be reflected near the surface, due to a fast decrease in density. The straight line shows the acoustic ray paths of $l$= 0 , 2,20,25 and 7 (Aerts et al., 2010).

where $c(r)$ is the adiabatic sound speed. It can be seen from this that the frequency separation is sensitive to the radius of the star, and is thus a measure of the mean density.

The asymptotic relation for g modes states that the periods of g modes are given by:

$$\Pi_{n,l} = \frac{\Pi_0}{\sqrt{l(l+1)}}(n+\epsilon), \tag{3.11}$$

where $n$ and $l$ are radial order and spherical degree, $\epsilon$ is a small constant and

$$\Pi_0 = 2\pi^2 \left(\int \frac{N}{r} dr\right)^{-1}, \tag{3.12}$$

where $N$ is the Brunt-Väisälä frequency and the integral is over a cavity in which a given g mode propagates.

There are many more aspects pf the theory of stellar oscillations that can be investigated. This chapter provided an overview of the general theory and these can now be applied to the specific cases of $\Delta$ Sct stars.

# 4 The $\delta$ Sct stars

In this chapter we characterize and describe the $\delta$ Sct stars more in detail, including the stars used in this work.

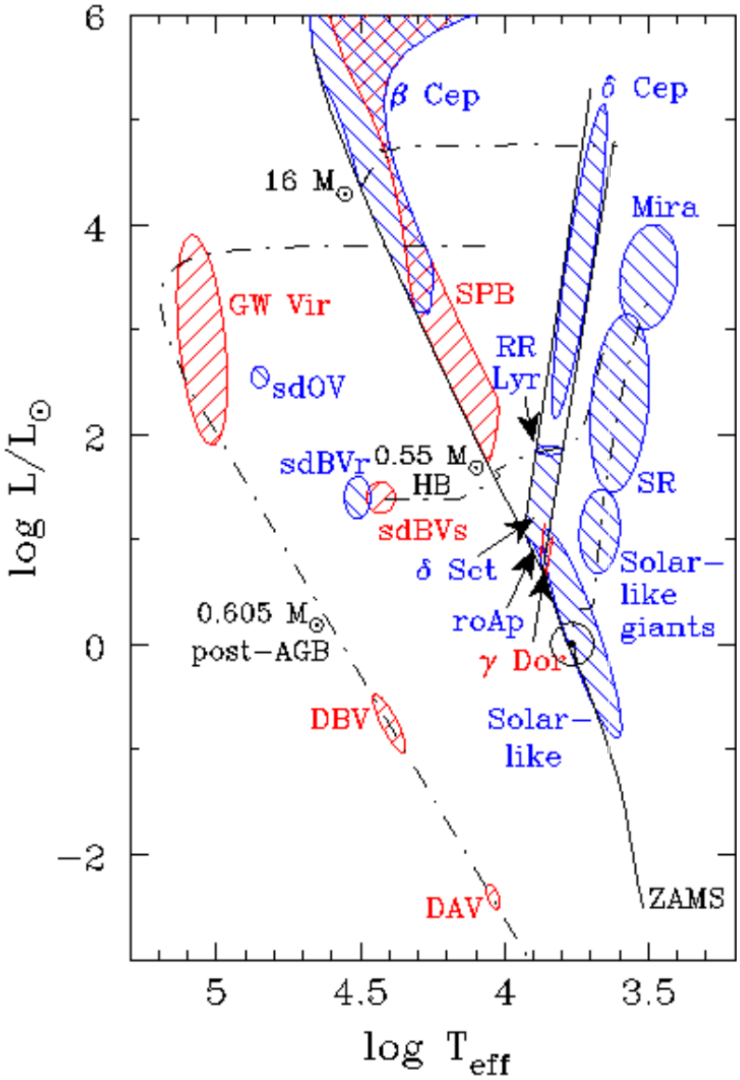


Figure 4.1: Asteroseismic HRD, showing the different classifications of pulsating stars.

## 4.1 The pulsation HR-diagram and the driving mechanisms

As mentioned in Chap. 3, there are many different types of pulsating stars, situated over the entire Hertzsprung-Russel diagram (HR-diagram). Fig. 4.1

illustrates the schematic overview of the various types of stars in the *asteroseismic HR-diagram.* Stars that have p mode pulsations are marked in red, whereas g mode pulsators are blue. The range for which the stars pulsate is marked in the HR-diagram and is called an *instability strip*(different for each type). The hybrids pulsate in both p and g modes simultaneously and can be found where the instability strips overlap.

The type of oscillation in a star depends on the *driving mechanism.* For the Sun and solar like-oscillators the primary driving mechanism is the stochastic driving. Acoustic energy from motion in convective cells in the outer convection zone can sufficiently cause a resonance at the star's natural frequencies, where a part of the energy becomes oscillation modes. A mode will be excited in a convection cell and damped when the cell turn over. But since there is a large number of convective cells it will be re-excited immediately after at a different phase. So the excitation is random or *stochastic.* For $\delta$ Sct stars, the driving mechanism is different. These are driven by a heat engine, which is a mechanism that transforms thermal energy in a star into mechanical energy of oscillations. When a star contracts the pressure and temperature increases, causing the opacity ($\kappa$) to increase in layers of H and He ionization. This is also why it is called the *$\kappa$-mechanism.* The radiative flux from the core is hence blocked and builds up underneath the layers of higher opacity. When the star reaches a thermodynamic equilibrium the additional stored energy is transformed into mechanical energy, causing the layers to move beyond the equilibrium; the star expands. When the star is heated the H and He atoms will ionize. The ionization of the gas causes a reduction in opacity and radiation can flow through. The gas then cools down so much that it can no longer support the weight of the overlying layers, and the star then contracts recombining H and He. The cycle then repeats itself. The zones where the radiative flux becomes trapped are the layers of partial ionization. The first zone is where H and He are ionized around 14.000 K, close to the surface of the star. Second ionization zone is around 40.000 K where He II is partially ionized. Lastly, the innermost zone is where ionization of iron elements occur, at 200.000 K. For $\delta$ Sct stars the driving mechanism excites primarily in the He II ionization layer.

Yet another type of driving mechanism is the *convective blocking* in Gamma Doradus ($\gamma$ Dor), DA and DB dwarfs. This mechanism is similar to the $\kappa$ mechanism, except the energy is stored in the outer convection zones. Such mechanism gives rise to g-modes oscillations rather than the p-modes from the $\kappa$ mechanism.

Contrary to the stochastic excitations in solar-like oscillators, the heat engine mechanism does not excite all modes to an observable amplitude, which makes *pattern recognition* challenging. It is also not well understood why only some modes are excited to an observable amplitude. Dziembowski & Królikowska (1990) suggested trapping in the acoustic cavity as an explanation to why only some modes are excited. They however do not exclude the possibility that the process is random. All of these features makes it difficult to determine the frequency of the mode i.e. *mode identification.* For stochastic oscillations, we are able to derive relations to estimate stellar age (Kjeldsen

& Bedding, 2011), however such relations has not yet been found for $\delta$ Sct stars. Therefore, mode identification is significantly more empirical and must be assessed with a more practical approach rather than theoretical.

## 4.2 Why $\delta$ Sct stars?

The main focus of this thesis is the $\delta$ Sct stars. In the pulsating HR-diagram $\delta$ Sct pulsators are located in the lower part of *the classical instability strip*. As mentioned previously they pulsate due to the $\kappa$ mechanism acting in the He II ionization zone. In the HRD, the region of $\delta$ Sct pulsations is marked is defined by the *rededge* and *blueedge*. The location of these edges is defined by the effective temperature of the $\delta$ Sct star. Higher effective temperature means that the opacity bump will be located deeper in the star where the star is denser. Therefore, the blue edge indicates the maximum effective temperature for which the He II opacity bump is still located at densities where the $\kappa$ mechanism can excite pulsations (Pamyatnykh, 2000). At temperatures lower than the red edge the convective layers go deep enough that oscillations are damped. These boundaries were calculated theoretically by considering the interaction between pulsation and convection (Dupret et al., 2004; Grigahcène et al., 2005).

The $\delta$ Sct stars have spectral types from A0 to F2, with pulsation periods between 18 minutes and 8 hours. They can be found on the PMS, MS and immediate post-MS, and their masses range from around 1.5 to 2.5 solar masses. There are several types of $\delta$ Sct pulsators, but historically they are divided into two main groups: High-amplitude $\delta$ Sct pulsators (HADS) with amplitudes of the dominant modes around 0.3 mag. Radial pulsations are dominant for these types. A vast majority of these types have low projected rotational velocities. The second group is the low-amplitude $\delta$ Sct pulsators (LADS) which pulsate in many non-radial modes and are suggested to have higher projected rotational velocities with an average $v \sin i$ of 96 $kms^{-1}$ (Solano & Fernley, 1997).

There are several reasons why these intermediate mass stars are of particular interest for understanding stellar evolution. They occupy a region in th HRD where many processes occur. They are at the transition where the outer convection layer goes from deep and active to shallow an ineffective. Additionally, stars in the classical instability strip have a convective core, which gives rise to convective processes near the core that cannot be found in the Sun. The reason this transition is so important is not only because it has an impact on the stability of pulsation but also on the mixing processes, evolution and particularly the lifetime. Therefore, understanding these processes in these stars makes it possible to project that knowledge to stellar evolution in general. Star that follow the following criteria are better subjects for studying.

- Every single additional pulsation frequency contain valuable information about the star. Therefore it is desirable to have a wide range of both radial and non-radial modes.

- As discussed in Chap. 3, rotation causes numerous effects that cannot be ignored in mode identification (rotational splitting) and modeling. Therefore, $\delta$ Sct stars with low rotational velocities are favored.

For these reasons 44 tau is a good candidate for studying and modeling. The results and methods can then be applied to stars where mode id has been less successful and modeling is needed. In this study, this will be HD 187547 (Antoci et al., 2014).

## 4.3 The delta Scuti stars 44 Tau and HD 187547

### 4.3.1 44 Tau

44 tau is a class F2 IV $\delta$ Sct star. The observational background and history of 44 Tau will be briefly presented here. For more details on the full observational history, see Antoci et al. (2007). Photometric campaigns were conducted by the *Delta Scuti Network* from 2000-2003. Here, an extensive frequency analysis was performed, and the rotational velocity has been determined to be as low as $2 \pm 1 kms^{-1}$ (Lenz et al., 2008). Since the average projected rotational velocity of early F-type stars is $114 \pm 5 kms^{-1}$ (Royer et al., 2004), this is a very small value, which lead to the discussion if the star is a slow rotator or if it is observed pole-on(Antoci et al., 2007). An additional multisite campaign was initialized in 2004 (Zima et al., 2007) and Breger & Lenz (2008) contributed with frequency analysis from seasons 2004/5 and 2005/6, giving a total of 6 years of photometry data. This yielded a total of 49 frequencies. These frequencies presented in Table 4.1. Zima et al. (2007) confirmed that 44 Tau is an intrinsically slow rotator by constraining the inclination angle to $60 \pm 25°$ with an equatorial rotation rate of $3 \pm 2 kms^{-1}$. Atmospheric parameters were derived from spectroscopy to be $T_{eff} = 7000 \pm 200K$ and $\log g = 3.6 \pm 0.1$ (Zima et al., 2007).

No significant interstellar reddening has been found, and the metallicity was determined to be close to that of the sun by McNamara & Powell (1985). From this metallicity the Vienna NEMO grid (Model Grid of Stellar Atmospheres, Nendwich et al. (2004), Heiter et al. (2002)) can be employed to derive an effective temperature and surface gravity. This was done by Lenz et al. (2008), yielding $\log T_{eff} = 3.839 \pm 0.007$ ($T_{eff} = 6900 \pm 100K$), in agreement with the spectroscopic value. Based on the HIPPARCOS parallax of $16.72 \pm 0.93 mas$ a luminosity of $\log L/Ł_{\odot} = 1.340 \pm 0.065$ was also derived. This was revised with a new bolometric correction to $\log L/L_{\odot} = 1.305 \pm 0.065$ (Lenz et al., 2010).

The recent data release for the GAIA mission has provided new atmospheric parameters for both 44 Tau and HD 187547. GAIA data release 2 was released on 25 April 2018 and is available through the Gaia Archive (Brown et al., 2018). GAIA conducts three-band photometry on bright sources, assuming that they are single stars. From the three-band photometry, measured parallax and training sets, estimates on $\log T_{\text{eff}}$ and $R$ are made. The luminosity can be derived through the G-band magnitude $M_G$ and bolometric correction $BC_G$:

$$-2.5 \log L = M_G + BC_G(Teff) - M_{bol,\odot}, \quad M_{bol,\odot} \tag{4.1}$$

Table 4.1: Observed frequencies of 44 Tau with the corresponding mode identification (Lenz et al., 2010).

| Frequency | Value $d^{-1}$ | $(l, m)$ |
|---|---|---|
| $f_1$ | $6.898 \pm 2.76222 \cdot 10^{-7}$ | (0,0) |
| $f_2$ | $7.006 \pm 1.21273 \cdot 10^{-6}$ | (1,1) |
| $f_3$ | $9.117 \pm 3.31115 \cdot 10^{-6}$ | (1,1) |
| $f_4$ | $11.52 \pm 1.0979 \cdot 10^{-6}$ | (1,0) |
| $f_5$ | $8.960 \pm 8.4549 \cdot 10^{-7}$ | (0,0) |
| $f_6$ | $9.561 \pm 1.9848 \cdot 10^{-6}$ | (1,-) |
| $f_7$ | $7.303 \pm 1.648910 \cdot 10^{-6}$ | (2,0) |
| $f_8$ | $6.795 \pm 2.793810 \cdot 10^{-6}$ | (2,0) |
| $f_9$ | $9.583 \pm 4.3814210 \cdot 10^{-6}$ | (0,0) |
| $f_{10}$ | $6.339 \pm \cdot 4.2260 \cdot 10^{-6}$ | (0,0) |
| $f_{11}$ | $8.639 \pm 5.4421110 \cdot 10^{-6}$ | (0,0) |
| $f_{12}$ | $11.29 \pm 6.20210 \cdot 10^{-6}$ | |
| $f_{13}$ | $12.69 \pm 1.844210 \cdot 10^{-6}$ | |
| $f_{14}$ | $5.305 \pm 7.280110 \cdot 10^{-6}$ | |
| $f_{15}$ | $7.790 \pm 4.50430869010 \cdot 10^{-6}$ | |

Some systematic errors were detected by Andrae et al. (2018). The GAIA atmospheric parameters for 44 Tau is listed along with the HIPPARCOS and spectroscopic values in Table 4.2.

Table 4.2: Observational parameters listed as given by Lenz et al. (2010) and Brown et al. (2018). The "parameter set column" divides the observationaæ parameters into to consecutive runs done for 44 Tau.

| | Value | Reference | Parameter set |
|---|---|---|---|
| $\log g$ | $3.6 \pm 0.01$ | (Zima et al., 2007) | 1 and 2 |
| $\log T_{\text{eff}}$ | $3.839 \pm 0.007$ | (Lenz et al., 2010) | 1 |
| $\log T_{\text{eff, GAIA}}$ | $3.843^{+0.003}_{-0.007}$ | (Brown et al., 2018) | 2 |
| $\log(L/L_\odot)_{HIP}$ | $1.305 \pm 0.065$ | (Lenz et al., 2010) | 1 |
| $\log(L/L_\odot)_{GAIA}$ | $1.383 \pm 0.004$ | (Brown et al., 2018) | 2 |

During this project, two difference runs will be made to implement the values for different parameters sets. Firstly, a run will be made with the Lenz et al. (2010) photometric $\log T_{\text{eff}}$ and $\log L/L_\odot$ with the spectroscopic $\log g$. Second run will be made with the GAIA $\log T_{\text{eff}}$ and $\log L/L_\odot$ ($\log g$ will be the same). In order to verify the GAIA values of $\log L/L_\odot$ a calculation was made based on the GAIA parallax, bolometric correction from Flower (1996) and B and V magnitudes from the Tycho-2 catalogue. This yielded a value of $\log(L/L_\odot)_{gaia} = 1.3572 \pm 0.0082$. This value will not be further investigated in the runs, but is made for making the point that parameters from GAIA (or any other mission) should not be used without considering their reliability and updates.

Mode identification yielded a confident identification of the radial fundamental mode and the first overtone (Lenz et al., 2008). Constraining models with these two frequencies has a major advantage in modeling, and Lenz et al. (2010) successfully reproduced the observed frequency range using stellar evolution models from the Warsaw new Jersey code developed by combined with a stellar pulsation code (Paczynski, 1969). The best model showed that 44 Tau is on the post-MS and more specifically in the contraction phase. Relative to the time spent on the MS for these stars, the lifetime in this phase is extremely short and therefore difficult to resolve in the HRD. Hence, modeling is of great importance when studying the evolutionary stage of a star.

### 4.3.2 HD 187547

Like 44 Tau, HD 187547 is a $\delta$ Sct star. It was observed with the NASA spacecraft *Kepler* (Koch et al., 2010). The first observations were taken over thirty days with one minute cadence. The frequency spectrum on Fig. 4.2 shows a large range of pressure modes for both high and low order radial modes, which could not be explained solely by the $\kappa$ mechanism. The frequency range is from $45 - 80d^{-1}$. Follow up ground-based observations were conducted during 2010 (Antoci et al., 2011), mainly spectroscopy; see Antoci et al. (2011) supplementary material for more information. Initially, Antoci et al. (2011) interpreted the high radial overtones as being stochastically excited, and thereby reported HD 187547 as the first $\delta$ Sct star where solar-like oscillations predicted by Houdek et al. (1999) and Samadi et al. (2002) were detected. However, an analysis carried out on an additional 960 days short cadence observations revealed that the spectrum is not consistent with a coherent signal (Fig. 4.3), but is suggested to be related to turbulent pressure (Antoci et al., 2014).

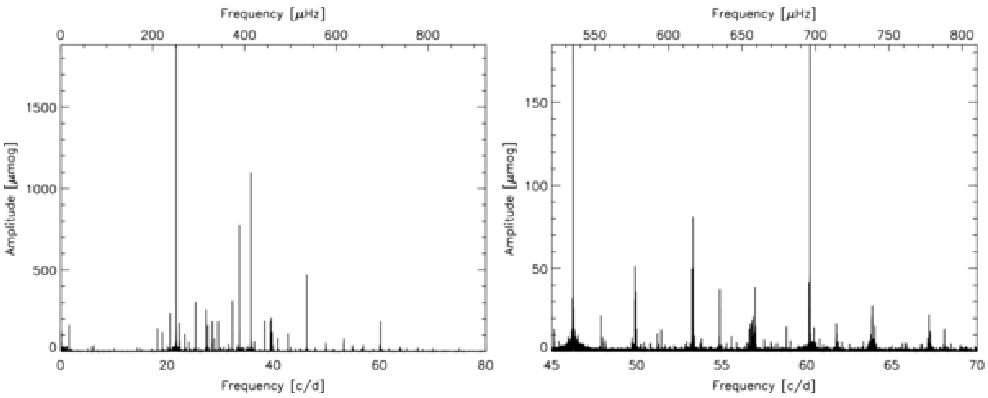


Figure 4.2: Fourier spectra of the Kepler short cadence data. Right panel: close-up in the frequency region interpreted by Antoci (2011) to be stochastically excited. Figure and caption from Antoci et al. (2014)

The spectroscopic observations made by Antoci et al. (2011) led to estimates on the atmospheric parameters $T_{eff} = 7500 \pm 250$, surface gravity of $\log g =$

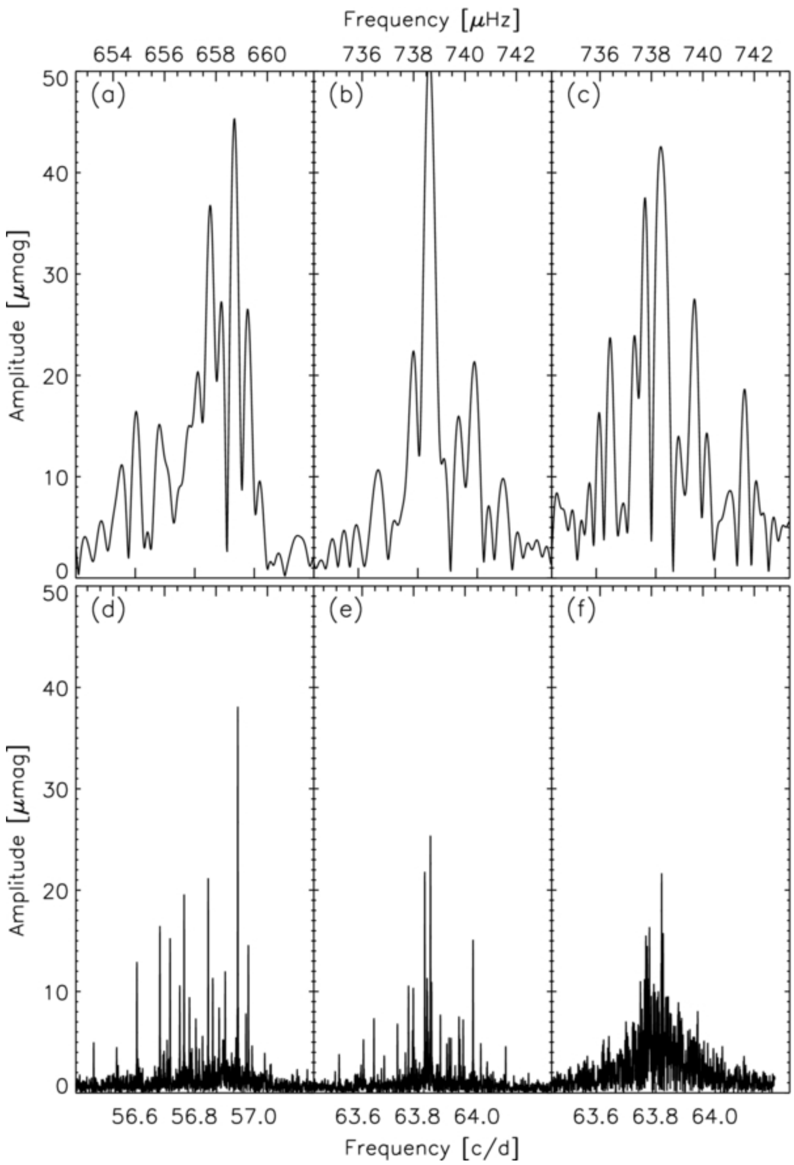


Figure 4.3: In panels (a), (b), (d), and (e), the Fourier spectra of two different oscillation modes observed in HD 187547 is shown. Panels (c) and (f) show simulated stochastic, damped, and re-excited oscillation mode. The Fourier spectra in panels (a), (b), and (c) are based on 30 days of observations (quarter 3.2,(Antoci, 2011)). Panels (d) and (e) illustrate the oscillation spectra of HD 187547 based on 960 days of short-cadence data. It can be seen that for a stochastic signal the amplitude decreases with increasing observing time, which does not occur in coherent modes. Figure and caption from Antoci et al. (2014)

$3.90 \pm 0.25$ and a projected rotational velocity of $v \sin_i = 10.3 \pm 2.3 kms^{-1}$. A photospheric metallicity of Z = 0.017 was also derived by Antoci et al. (2011). The analysis of the high-frequency modes lead to the determination of a large frequency separation of $\Delta\nu = 3.5 \pm 0.05 d^{-1}$. Models with $\log L/L_{\odot} \approx 1.3$ were used for the purpose of modeling the star. However, observations from GAIA has provided new reviewed parameters with a significantly lower $\log L/L_{\odot} = 0.859 \pm 0.003$. The luminosity was also derived by the same method as for 44 Tau in this project, leading to a value of $\log L/L_{\odot} \approx 0.837$. The low value of the luminosity could indicate that the star is not as far in its evolution as Antoci et al. (2011, 2014) anticipated. This would also mean that the $\Delta\nu$ value should be reviewed, even doubled to $\Delta\nu = 7d^{-1}$ (Private communication with Victoria Antoci, Tim Bedding et al. in review). The main focus for HD 187547 will therefore be to determine what $\Delta\nu$ is best reproducing the observed parameters.

| | Value | Reference |
|---|---|---|
| $\log g$ | $3.9 \pm 0.02$ | (Antoci et al., 2011) |
| $\log T_{\text{eff}}$ | $3.875 \pm 0.0011$ | (Antoci et al., 2011) |
| $\log T_{\text{eff, GAIA}}$ | $3.900 \pm 0.002$ | (Brown et al., 2018) |
| $\log(L/L_{\odot})_{GAIA}$ | $0.859 \pm 0.003$[1] | (Brown et al., 2018) |

Besides the peculiar frequency spectrum, an analysis of the abundances of HD 187547 classified it as a chemically peculiar Am star. This means that it shows photospheric overabundances in Ba, Y, and Sr and underabundances in Sc and Ca (Preston, 1974). Particularly of interest are the pulsating AmFM stars, since they do not comply well with predictions from the $\kappa$-mechanism. The theory states that settling of He causes an underabundance in the He II ionization layer, hence the $\kappa$-mechanism cannot drive the pulsation sufficiently. Turcotte et al. (2000) implemented diffusion of heavy elements into the models to account for only a very tightly constrained instability region. However AmFm are not only observed in this region, but over the entire $\delta$ Sct instability strip (Balona et al., 2011; Smalley et al., 2011). In that sense, HD 187547 is interesting not only because of its wide frequency range, but also because those frequencies are even more unusual for a pulsating Am star. Therefore it is of great interest to model this star to gain information on the nature of the pulsations.

[1]The values from GAIA have not considered reddening which is relevant for HD 187547. Therefore they should be used with care.

# 5 Computational tools

In this Chapter an introduction to the tools used to for computations of both stellar evolution models and pulsation frequencies is provided. In Sec. 5.1, the stellar structure and evolution code `MESA` is introduced, and the most relevant aspects for this work is discussed.

## 5.1 MESA

Modules for Experiments in Stellar Astrophysics or MESA is a suite of open source libraries that can be used to compute various applications in stellar astrophysics. Documentation can be found on the webpage `http://mesa.sourceforge.net/index.html` and from papers released with new updates (Paxton et al., 2013, 2015, 2018, 2019, 2010). MESA consists of several modules that works together in order to create computational models of stellar astrophysics. They have both the ability to work independently and each is constructed as a separate Fortran 95 library. All original modules (Paxton et al., 2010) with their purposes are listed in Table 5.1.

Here, the main focus will be on the `MESA star` 1D stellar evolution module.

There are several modules that provides numerical methods used for the computations, the first being the `mtx` module, providing an interface for linear algebra and matrix manipulation. The `num` uses these matrix routines as well as providing a number of solvers for ordinary differential equations from Wanner & Hairer (1996). It also includes a Newton-Raphson solver for multidimensional, nonlinear root finding (derived from Lesaffre's version of the Eggleton stellar evolution code (Eggleton, 1971; Lesaffre et al., 2006; Pols et al., 1995). The modules `interp_1d` and `interp_2d` uses 1-dimensional and 2-dimensional interpolation, respectively. Lastly, the `alert` module reports messages and errors and the `utils` module checks the variables for bad numbers such as NaN and infinity.

### 5.1.1 Stellar structure and evolution

The `MESA star` module that implements several numerics and astrophysics modules to compute stellar evolution tracks using a Henyey-style code (Henyey et al., 1959) with automatic mesh refinement, analytical Jacobians and solutions to coupled stellar structure and composition equations. The `MESA star` implementation is constructed with inspiration from stellar evolution and hydrodynamics codes such as EV (Eggleton, 1971), EVOL (Herwig, 2004), EZ (Paxton, 2004), FLASH-the-tortoise (Lesaffre et al., 2006), GARSTEC (Weiss & Schlattl, 2008), NOVA (Starrfield et al., 2000), TITAN (Gehmeyr & Mihalas, 1994) and TYCHO (Young & Arnett, 2005).

Firstly, `MESA star` reads the input files needed for the run. There are two files that determine the specific controls for `MESA star` to read and implement. The first file specifies the type of evolutionary calculation, EOS and opacity prescriptions, and chemical composition among other properties. Changing

| Name | Type | Purpose |
|---|---|---|
| alert | Utility | Error handling |
| atm | Microphysics | Gray and non-gray atmospheres; tables and integration |
| const | Utility | Numerical and physical constants |
| chem | Microphysics | Properties of elements and isotopes |
| diffusion | Macrophysics | Gravitational settling and chemical and thermal diffusion |
| eos | Microphysics | Equation of state |
| interp_1d | Numerics | One-dimensional interpolation routines |
| interp_2d | Numerics | Two-dimensional interpolation routines |
| ionization | Microphysics | Average ionic charges for diffusion |
| jina | Macrophysics | Large nuclear reaction nets using reaclib |
| kap | Microphysics | Opacities |
| karo | Microphysics | Alternative low-T opacities for C and N enhanced material |
| mlt | Macrophysics | Mixing length theory |
| mtx | Numerics | Linear algebra matrix solvers |
| net | Macrophysics | Small nuclear reaction nets optimized for performance |
| neu | Microphysics | Thermal neutrino rates |
| num | Numerics | Solvers for ordinary differential and differential-algebraic equations |
| package_template | Utility | Template for making a new MESA-module |
| rates | Microphysics | Nuclear reaction rates |
| screen | Microphysics | Nuclear reaction screening |
| star | Evolution | One-dimensional stellar evolution |
| utils | Utility | Miscellaneous utilities |
| weaklib | Microphysics | Rates for weak nuclear reactions |

Table 5.1: MESA module Definitions and Purposes. From (Paxton et al., 2010).

the parameters in this file allows to make a grid as described in Sec. 6.1. The second file specifies the controls to be applied during the run All of the options for the inlist files can be found in the documentation. There are generally two ways to initiate an evolutionary run. One option is to let MESA evolve a PMS model based on an input of an input mass, luminosity and initial abundances. The star then evolves from the PMS and until a certain stop criterion is fulfilled. However, if an entire grid is needed it is a disadvantage to calculate all the PMS models for all individual tracks. The second (and more favorable) option in this work, is to use a pre-calculated PMS model in the inlist and let MESA relax the parameters in the following evolution. In this work a $1.7M_\odot$ PMS model is applied for this purpose [1].

When the input files have been read, the physics modules (EOS, opacities and nuclear network) are initialized. In the first step, the evolutionary run begins. MESA then continues the evolution by continuing to the next time step. As this happens, the model is remeshed if nescessary, mass loss is taken into

[1] However, one needs to be aware that relaxing the parameters can give numerical issues if the PMS sequence model and the initial parameters used for further evolution are too far apart (since it would be numerically feasibly to relax the mass of a $1.7M_\odot$ model to $8M_\odot$).

account (although not used in this work since the mass is assumed constant after being relaxed to the MS), abundances are adjusted by taken diffusion into account, and the solvers are called (Newton-Rapshon) to calculate a new structure and composition solution. Lastly, a new time step is calculated. Within this one time step, `MESA star` builds a one-dimensional spherically symmetric model, where the star is divided into cells reaching from the core to the surface of the star. During one time step, `MESA` does not solve structure equations separately from composition equations. Instead, an entire set of coupled equations are solved for all cells simultaneously. Some of the controls for adjusting structure and time steps relevant for this work are further discussed in Sec. 6.2.

### 5.1.2 Output

There are three different types of output files in `MESA`, which can be used for different purposes. The first is the *history* file, where the history for the entire run is saved. The header contains information on the initial parameters set in the run such as the initial mass and Z abundance. Hereafter, one line corresponds to one *model*. The first two columns contain information on the *model_number*. The rest of the columns show calculated properties such as age, mass and luminosity.

The next output file is the *profile*. On the contrary to the history files, the profiles only contain information of one model. The first line shows the global properties such as the age. The rest of the file shows properties for each point or *zone* in the model. Since it is computationally heavy for `MESA` to write the profiles, it is necessary to evaluate whether all zones are needed in the output files. For this project, it was found sufficient to only use information on the core and surface.

The third output file is *profiles.index*. Since `MESA` does not save profiles for every *step*, the *profile number* and model number are not necessarily the same. Therefore, the profiles.index tells the user how to translate between these.

Additionally, in order to be able to calculate the frequencies in GYRE, an output file for this is needed. This is done by adding the `write_pulse_data_with_profile = .true.` command to the the inlist, producing a *profile.GYRE* file for each corresponding profile. These will be described in more detail in Sec. 5.2.

### 5.1.3 Convection treatment

In Sec. 2.1 the condition for convection has already been discussed briefly. There are several theories that leads to a numerical implementation. Therefore, the main focus here will be the implementation of `MESA mlt` module.

The implementation of convection in both `MESA` and the Warsaw-New Jersey stellar evolution code is based on the standard-mixing length theory of convection as presented by Weiss et al. (2004). This theory provides a very simplified picture of the physical processes of convection, as well as a qualitative and reasonable description of heat transfer by convection. However, the quantitative results should not be expected to have high accuracy or reliability. One parameter that particularly causes discussions due to its high uncertainty, is the parameter describing the mixing length itself. The mixing length, $\Lambda$ is described as the mean-free path that a fluid element travels inside a convectively unstable region in a star. In outer layers of a star, it can be assumed that $\Lambda$ is proportional to the pressure scale height $\lambda_p$. In `MESA mlt`, the mixing-length is therefore implemented as

$$\Lambda \equiv \alpha_{mlt}\lambda_p, \tag{5.1}$$

where $\alpha_{mlt}$ is the parameter input in `MESA`. It is generally assumed to be constant throughout the star. The value of this parameter is only known to be of order one (while the default value in `MESA` is 2), from physical arguments. Having a high mixing length in outer layers essentially means that the bubbles can travel far before dissolving into the environment and the convection is efficient. For $\delta$ Sct stars, the convective outer layer is significantly smaller than that of solar-type stars. Therefore, it is safe to assume smaller efficienty of energy transport by convection. On Fig. 5.1, evolutionary tracks for two models with different mass can be seen in an HR-diagram. The black line shows the track calculated with $\alpha_{mlt} = 0.2$ and the red with $\alpha_{mlt} = 0.8$. From this it is clear that the dependence on the mixing-length parameter is not very significant until just before the red giant branch. Here, the higher $\alpha_{mlt}$ causes a significant drop in luminosity, due to the vast changes in the structure.

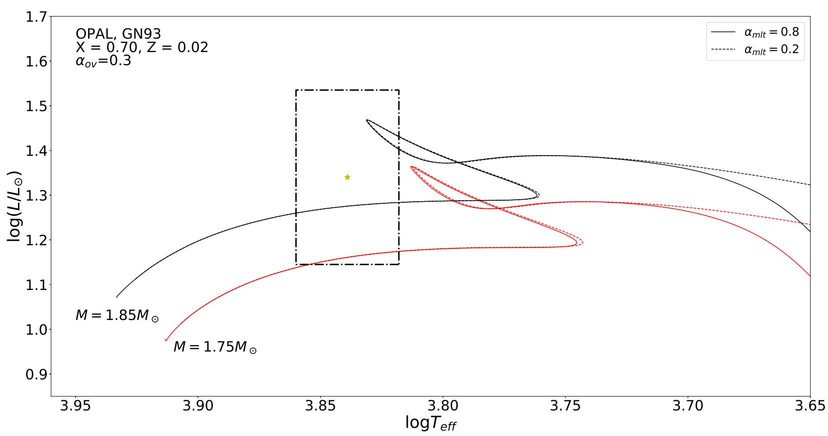


Figure 5.1: Evolutionary tracks with masses of $M = 1.75M_\odot$ and $1.85M_\odot$ and parameter combinations of $X = 0.70$,$Z = 0.02$, $\alpha_{ov} = 0.2$. Each are calculated with two different mixing lengths of $\alpha_{mlt} = 0.5$ (red line) and $\alpha_{mlt} = 0.5$ (black line). The black dashed line indicates errobox for uncertainties for observed parameters from Lenz et al. (2010).

Even though the mixing length paints a nice picture of the convection in the outer layers, there are still issues related to the convection deep in the interior. Specifically to which extend chemical elements are mixed, as it has a big impact on the later evolution of the star. For MS stars with a convective cores the main discussion topic is the convective core overshooting. The convective core overshooting relates to the issue that the boundary between convective core and radiative layers is not sharp; instead, the convection "overshoots" into the layer above (for a quantitative description, see Kippenhahn et al. (1990), Chap. 30). The amount of overshoot depends on the velocity of the convective elements and the breaking force, which are difficult to find as it includes non-local solutions to velocities, gradients and fluxes in the entire core. Therefore, the values for overshooting are, as for the mixing length), arbitrary and can only be evaluated through modeling.

There are two standard methods that are commonly used to calculate the overshoot numerically. The first one is quite similar to that of the mixing length, describing the extension of the convective region defined by the Schwarzschild criterion, in terms of pressure scale height

$$l_{ov} = \alpha_{ov} H_p, \tag{5.2}$$

in which $\alpha_{ov}$ is typically in the order of 0.1 and 0.2. Even though it resembles the description of the mixing length parameter $\alpha_{mlt}$, it has no relation to it and is purely detemined through comparing models to observations. This prescription is applied as "step overshoot" in MESA. The second method considers convective overshoot as a diffusive process with a diffusion constant depending on the radial distance z from the border defined from the Schwarzschild criterion.

$$D(z) = D_0 \exp \frac{-2z}{f_{ov} H_p}, \tag{5.3}$$

where $f_{ov}$ is a free parameter in the order of 0.02, and $D_0$ sets the scale of the diffusive speed. This prescription has a particular advantage as it can be added quite easily to a stellar evolution code where diffusion is already implemented. However, for this work, only the former prescription is implemented.

The reason that convective core overshoot is important to implement is that the overshoot causes additional mixing of elements. Hence, more hydrogen is transported to the core, acting as additional fuel on the main sequence. Therefore, just a small extension to the convective core causes a significant continuastion of the main sequence. An example can be seen on Fig. 5.2, where two stellar evolution tracks of masses $1.95 M_\odot$ and $1.75 M_\odot$ are shown. The black line indicates a track with $\alpha_{ov} = 0.2$ and the red line the corresponding track with $\alpha_{ov} = 0.3$. it can here clearly be seen that the main sequence is significantly longer for models with higher $\alpha_{ov}$, and that it affects the remaining part of the evolution as well.

### 5.1.4 Element abundance mixtures

In order for `MESA` to calculate a stellar model, the element abundances needs to be implemented. The chemical composition of a star is assumed to be a reflection of the distribution of elements in the cloud from which the star was born, assuming that the composition is preserved in the outer layer of the star. Since solar neighbourhood abundances are usually more accurately measured than stars outside, the solar element mixture is commonly used for modeling

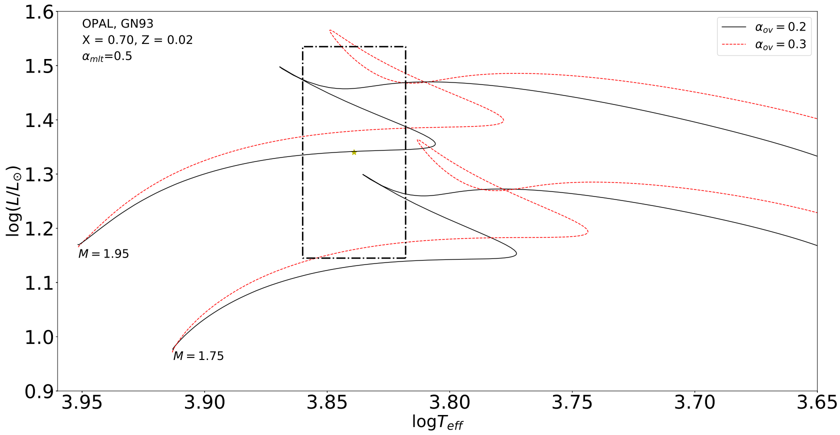


Figure 5.2: Evolutionary tracks with masses of $M = 1.75M_\odot$ and $1.85M_\odot$ and parameter combinations of $X = 0.70, Z = 0.02$, $\alpha_{mlt} = 0.5$. Each are calcululated with two different mixing lengths of $\alpha_{ov} = 0.3$ (red line) and $\alpha_{ov} = 0.2$ (black line). The black dashed line indicates errobox for uncertainties for observed parameters from Lenz et al. (2010)

stars from outside the neighbourhood as well. In MESA, the initial abundances X (hydrogen), Y (helium) and Z (metals, i.e. all elements with atomic numbers higher than helium) is given in terms of mass fractions where $1 = X + Y + Z$ must always be fulfilled.

The solar element abundances depends on the choice of theoretical atmosphere model. Hence, they are updated continuously as atmosphere models are changed and improved. There are several abbreviations of element mixtures that can be appliued in `MESA`, such as GN93 (Grevesse & Noels, 1993), GS98 (Grevesse & Sauval, 1998) and a09 (Asplund et al., 2009). Grevesse & Noels (1993) used a one-dimensional hydrostatic atmosphere model to derive the solar abundances, and compared to the solar system abundances extracted from meteorites, and found good agreement. This is what is used in this project. The main reason for this is that compared to a09, GN93 does not have issues such as *the solar abundance problem*(Asplund et al., 2009). The importance of element mixture choice is further discussed in Sec. 7.

### 5.1.5 Equation of state

The equation of state takes the density and temperature and calculate the corresponding pressure, ionization degrees and thermodynamic quantities necessary to calculate the stellar structure.

The equation of state is implemented through the `EOS` module, where density $\rho$ and temperature $T$ are treated as independent variables in the Helmholtz free energy formulation. However, some calculations are carried out through the Gibbs free energy formulation where the density can be provided through root-finding. This is computationally heavy, so the roots are therefore

Table 5.2: References for the two opacity groups.

| Source | Reference |
|---|---|
| OPAL | Iglesias & Rogers (1996) |
| OP (Opacity Project) | Badnell et al. (2005) |

pre-processed, creating $P_{gas}$ and $T$ tables that allows for a quicker solution when calling the `EOS` module (provided that the input values are within the range of the pre-computed values). The $\rho - T$ tables are based on OPAL EOS tables from Rogers & Nayfonov (2002), and for lower values Saumon et al. (1995), covering an area up to $Z \leqslant 0.04$. If parameters are outside of the region covered by the `MESA` tables, the EOS from HELM (Timmes & Swesty, 2000) and PC (Potekhin & Chabrier, 2010) are used. These use a free energy approach assuming complete ionization, which is applicable to the region outside of the tables (where cooler stars are only partly ionized).

### 5.1.6 Opacity data

From the density, temperature and chemical composition, the EOS yields estimates on the ionization equilibrium concentrations and level populations in a medium. These can be used to evaluate the Rosseland mean opacities. These are implemented though the `kap` module in `MESA`, where pre-processed opacity tables are within the `make_kap` module. The electron conduction opacity tables are based on Cassisi et al. (2007). For the radiative opcaities, low temperature regions ($\log T \leqslant 4$) is covered by Freedman et al. (2008) or Ferguson et al. (2005).

Radiative opacities have been calculated by two teams, OPAL and OP. The references for the groups are listed in Table 5.2

Both groups uses slightly different methods to compute the radiative opacities (Seaton & Badnell, 2004). For this project, only the OPAL opacities are implemented, which will be discussed briefly in Chap. 7.

## 5.2 GYRE

In order to interpret asteroseismic observations from recent mission such as MOST (Matthews, 2007; Walker et al., 2003), CoRot (Michel et al., 2008) and Kepler (Borucki et al., 2009; Gilliland et al., 2010), a stellar oscillation code calculating the eigenfrequency spectrum of an input stellar model is needed. The asteroseismic module included in `MESA` is based on the stellar pulsation code `ADIPLS` (Christensen-Dalsgaard, 2008a), which allows for a calculation of the eigenfrecuencies. However, a demand for more detailed non-adiabatic calculations lead to the development of `GYRE`, which is an open source pulsation code from 2013 described in (Townsend et al., 2017; Townsend & Teitler, 2013) and on the webpage (Townsend, 2013).

`GYRE` is written in `Fortran 2008` and uses a *Magnus Multiple Shooting* (MMS) scheme to solve linearized pulsation equations. The following steps are used to calculate the eigenfrequencies for an arbitrary input model:

1. *Stellar model* As a first step, `GYRE` needs to read an input model. This model can be either read from a pre-built or can be constructed analytically. It supports three different classes of models. The first is the evolutionary models (which is what is used in this work) constructed from a stellar evolution code. The second relies on polytropic models, and the last is purely analytical calculations based on explicit expressions for structure coefficients.

2. *Grid calculation* When the file has been read, a calculation grid is constructed. The grid allows for multiple shooting and eigenfunction reconstruction. The type of grid idepends on the type of input model.

3. *Root-finding* Initial guesses for discriminant roots are found by scanning the frequency space in the grid.

4. *Eigenfunctions* Based on the initial guesses of roots, the corresponding eigenfunctions are then constructed.

These are only the very basic steps used by `GYRE`; a more detailed description of the numerical steps used is beyond the scope of this work, and the reader is instead referred to (Townsend & Teitler, 2013).

It is now also possible for `GYRE` to be implemented directly in the `MESA star` module, which couples calculations of both stellar evolution and frequencies. However, implementing it is a bit more intricate than reading in the files separately; therefore, the first method is used in this project (calculating a grid of models that can then be used as an input for the `GYRE` calculations).

### 5.2.1 Input and output options

`GYRE` reads input parameters given in an input file. The input file is structured in a similar way as the `MESA` inlist files, consisting of several namelist groups:

- *Constants* Defines the physical constants such as the gravitational constant and solar parameters (mass, luminosity etc.)
- *Stellar model* Defines the stellar model that `GYRE` reads and constructs eigenfrequencies for.
- *Mode parameters* Defines mode parameters such as $l, m$ and minimum and maximum radial orders.
- *Oscillation parameters* Defines the parameters relates to the oscillation, such as inner and outer voundary conditions and rotation.
- *Numerical parameters* Specifies numerical methods parameters.
- *Frequency scan* Defines the span of the frequency space scan with a set of points.
- *Calculation grid* Defines the parameters used for the calculation grid.

- *Output files* Specifies the output produced by the end of a run. This includes the file format, frequency units, comma separation etc.

For this project, the input model is constructed as a .GYRE file for every profile constructed in `MESA`, which is then read into the `GYRE` input file. The input files used in this project for 44 Tau and Superstar is constructed from a bash script which can be seen in Sec. 8.1. When the input file has successfully been read and the calculations have finished, `GYRE` constructs one of two different types of ouput files. The first is the Summary files that provides global information on the theoretically produced modes. The second is the mode files, containing information on a single mode including detailed eigenfunction quantities such as rotation kernels. For this project, the first file is used. The contents of the output file is defined in the input file described above with the `summary_item_list` (or, correspondingly `mode_item_list`). The most relevant for this project is the harmonic degree, radial order and frequencies. Options for non-adiabaticity can be included in the `GYRE` calculations and will be discussed in Chap. 7.

# 6 Modeling 44 Tau and HD 187547

In this chapter the process of modeling the stars 44 Tau and Superstar in `MESA` and `GYRE` is described. The methods for comparing the models to observations is introduced and discussed.

## 6.1 Choosing a grid

For this project a grid of models is calculated in order to compare to observations and determine the evolutionary stages of 44 Tau and HD 187547. More than one approach can be taken to reach this goal, each with their own advantages and disadvantages. Lenz et al. (2010) narrows down the grid size by first calculating the best mass for each stage. It is an approach where the star is initially assumed to be in the MS, post-MS contraction or post-MS expansion phase. This results in three different grids where the best model is found for each stage. This method has the advantage that is it forces a result on all three stages. However, it is a process that requires the grid to be narrowed through several steps, including a separate analysis of the mass range.

In this project a slightly different approach is used. Instead of dividing the models into different stages and narrowing the three grids, a wide grid stretching over the entire instability domain is calculated, and of these the best models are found. To find not only the best overall model, but also consider their tracks and initial input parameter combination, the best model for each track is found. This choice is discussed in Sec. 6.3.1.

As discussed in Sec. 5, the input parameters $\alpha_{mlt}$, $\alpha_{ov}$ have a great influence of the further evolution of the star. Other input parameters such as initial abundances and the mass in particular also influence the evolution of the star. Therefore, the input parameters for the initial grid need to be thoughtfully considered. The grid must be wide enough in parameter space to not only cover the observationally determined parameter space, but adequately beyond this in order to include the uncertainties on the observations. The mass has not been observationally determined, but since both stars have been classified $\delta$ Sct stars, the mass can be narrowed by the instability strip. Usually this includes stars between 1.5-2.5 $M_{\odot}$. Therefore this mass range is chosen to be from $1.5M_{\odot}$ to 2.2 $M_{\odot}$[1]. This yields a range of $0.65 < X < 0.75$ and $0.01 < Z < 0.03$[2]. Numerical results for two different masses and $Z$ can be seen on Fig. 6.1. Here, the red color correspond to masses of $M = 1.75M_{\odot}$ and black lines $M = 1.85M_{\odot}$. The different values of $Z$ are represented with

[1]This limit should preferably be $2.5M_{\odot}$, but was here restricted to $2.2M_{\odot}$ due to lack of time.

[2]`MESA` can go much lower, but is chosen to be 0.01 as there is no indication that either of the stars have extreme values for $Z$. The upper limit is $Z = 0.04$, but this caused convergence issues for more tracks. Therefore, it is limited to 0.03 here.

full and dashed lines respectively. There is a clear difference between tracks with different $Z$. Higher values of $Z$ yield a high opacity which blocks the radiation from the inner layers. Hence, stars with higher metallicity will be less luminous. In this case, the luminosity difference is in the order of $\log L/L_\odot = 0.2$ within the three sigma uncertainties on the luminosity. It can also be seen from eq. (7.3) in Christensen-Dalsgaard (2008b) that $L$ $propt\frac{1}{\kappa}$ ($\kappa$ being the opacity.)

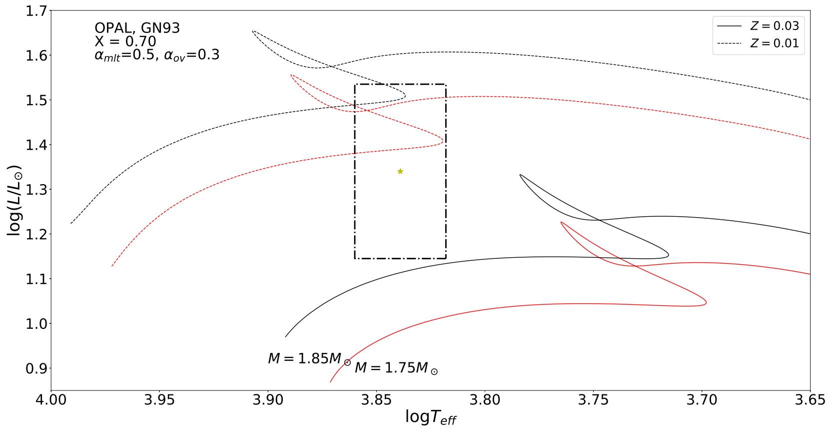


Figure 6.1: Stellar evolution tracks for two different masses with two different metal abundances. Each track has $X = 0.70$, $\alpha_{mlt} = 0.5$ and $\alpha_{ov} = 0.3$. The red lines indicates tracks with masses of $M = 1.75M_\odot$, and black lines indicate $M = 1.85M_\odot$. The full lines have $Z = 0.03$ and dashed lines $Z = 0.01$. The black dashed box shows the three sigma uncertainties on $\log L/L_\odot$ and $\log T_{\rm eff}$ (from Lenz et al. (2010)).

Numerical results for increasing initial abundances at fixed metallicity can be seen in Fig. 6.2. The line and color convention corresponds to that of Fig. 6.1, with the difference being the line type indicating the values of $X$ instead. Here it is also clear that the initial hydrogen abundance affects the luminosity. Higher hydrogen abundances causes $\kappa$ to increase, hence decreasing $\log L/L_\odot$.

Parameters $\alpha_{mlt}$ and $\alpha_{ov}$ difficult to establish, since they are purely empirical and depend strongly on the prescription used in the modeling (see Sec. 5.1.3. For the $\alpha_{mlt}$ the standard value in `MESA` is around 1.8. The Warsaw-New Jersey stellar evolution code used to calculate models for 44 Tau by Lenz et al. (2010) has a mixing length prescription bases on the standard mixing length theory like `MESA`. Their results showed that models with mixing length of $\alpha_{mlt} > 0.2$ gave the best fits, confirming the assumption that smaller mixing lengths than the sun is needed in order to model these stars. However, `MESA` is not computationally capable of handling a mixing length below 0.2 which is not surprising as it would mean that energy transport by convection in the outer layers is almost non existing in the `MESA` implementation. This also underlines the fact that convection is treated differently in each stellar evolution code

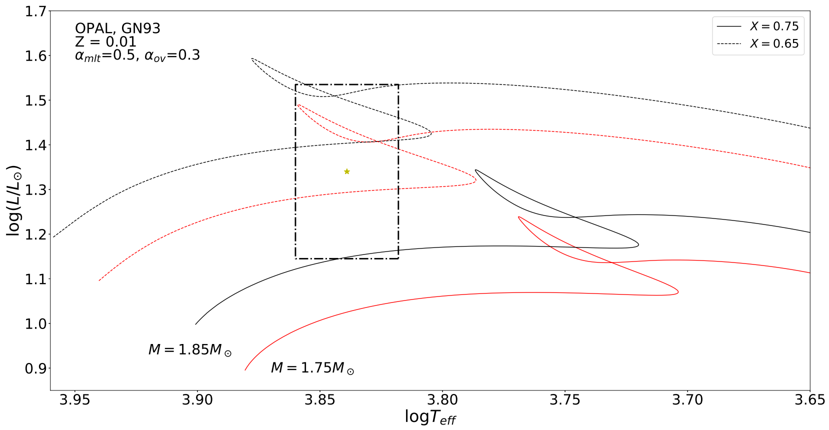


Figure 6.2: Stellar evolution tracks for two different masses with two different metal abundances. Each track has $Z = 0.01$, $\alpha_{mlt} = 0.5$ and $\alpha_{ov} = 0.3$. The red lines indicates tracks with masses of $M = 1.75M_\odot$, and black lines indicate $M = 1.85M_\odot$. The full lines have $X = 0.75$ and dashed lines $X = 0.65$. The black dashed box indicates the three sigma uncertainties on $\log L/L_\odot$ and $\log T_{\rm eff}$ (from Lenz et al. (2010)).

through the implementation of $\alpha_{mlt}$(as discussed in Chap. 5), which therefore needs to be carefully evaluated in the grid. It can also be argued that since $\delta$ Sct stars have a significantly smaller convection layer than that of the Sun, the convection will not be as efficient. Trampedach & Stein (2011) calculated a range of mixing lengths through a grid simulation of solar type structures. One of the results can be seen on Fig. 6.3.

The mixing length is predicted to be smaller for higher values of $\log T_{\rm eff}$, as expected. Both 44 Tau and HD 187547 are out of range in $\log T_{\rm eff}$ space, since the mixing length range here is calculated based on solar-like structures. However, the trend in mixing length is still applicable to the stars in this work. As an initial grid, values of $\alpha_{mlt}$ between 0.2 and 0.8 are chosen. Analogous to the mixing length, the convective overshoot near the core is described with the convective core overshoot parameter $\alpha_{ov}$. As it is typically in the order of 0.1-0.2 (Kippenhahn et al., 1990), values between 0.1-0.3 are chosen. The initial grid used here can be seen in Table 6.1.

Some of these combinations did however not converge properly, and could therefore not be included in the grid. These models are:

- $M = 1.50M_\odot$: combinations with $X = 0.75$ and $Z = 0.02$ or $Z = 0.03$
- $M = 1.55M_\odot$: combinations with $X = 0.75$ and $Z = 0.03$
- $M = 1.95M_\odot$: combinations with $X = 0.75$ and $Z = 0.03$
- $M = 1.80M_\odot$: combinations with $X = 0.75$ and $Z = 0.02$ and $\alpha_{mlt} = 0.2$
- $M = 1.90M_\odot$: combinations with $X = 0.75$ and $Z = 0.02$ and $\alpha_{mlt} = 0.8$

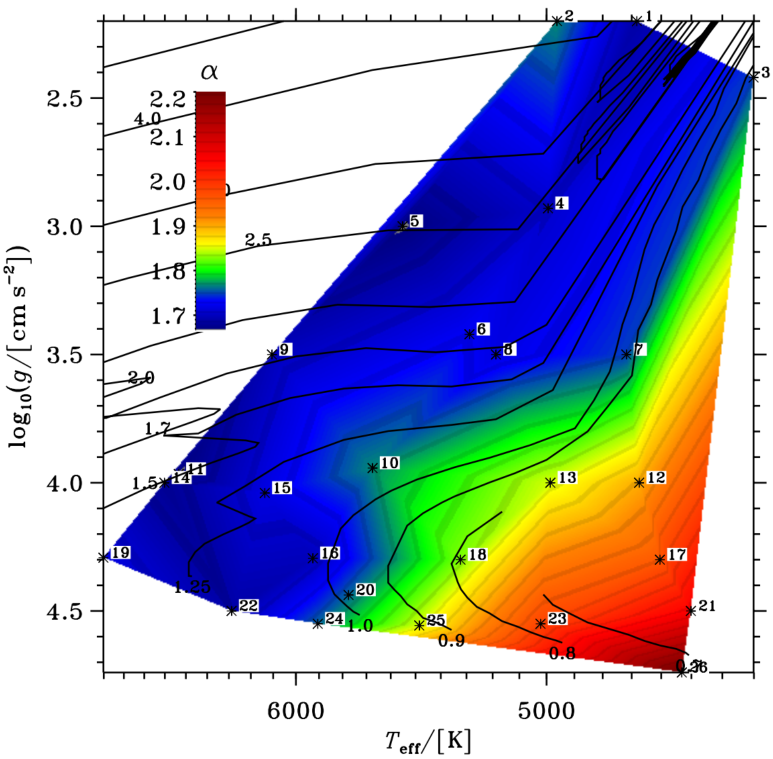


Figure 6.3: Mass mixing lengths in units of pressure scale height $H_p$ in the $\log T_{\text{eff}}$- $\log g$ plane. From (Trampedach & Stein, 2011).

Table 6.1: Values and step sizes for all parameters in the grid calculated in this work.

| | values | step size |
|---|---|---|
| X | 0.65-0.75 | 0.05 |
| Z | 0.01-0.03 | 0.01 |
| Mass/$M_\odot$ | 1.5-2.2 | 0.05 |
| $\alpha_{mlt}$ | 0.2-0.8 | 0.3 |
| $\alpha_{ov}$ | 0.1-0.3 | 0.1 |

It is unclear why these exact combinations have numerical issues, and further investigation needs to be done. Some of these combinations lead to extreme helium abundances , particularly the case where $X = 0.75$ and $Z = 0.03$ yielding $Y = 0.22$. This might explain most of the issues since this value is lower than the primordial helium abundance. Likewise, the combination of $X = 0.65$, $Z = 0.0.1$ yields $Y = 0.31$ which might only be observed in strange cases. The reason for still including these extreme values is that models might still be able to reproduce these numbers in the calculation. So if a model has this value it can be interpreted as an example of the imperfect theory behind the stellar structure an evolution codes.

## 6.2 Resolution and varcontrol

As mentioned previously in Sec. 5.1, they way `MESA` works is to fulfill calculations in time steps that are non-equidistant. As a result of this, models on a track can be far apart, particularly if the evolution is fast. This means that models on the MS are well resolved, while the models on fast stages (particularly post-MS contraction phase) are far apart in terms of structure. This also results in the frequencies being very different from one model to another, which should be considered when calculating the $\chi^2$ (see Sec. 6.3). An example can be seen on Fig. 6.4 where, the radial fundamental mode is plotted as a function of timestep. The upper panel shows an HRD with the evolution divided into three stages MS (1), post-MS contraction (2), and post-MS expansion (3). The lower panel of Fig. 6.4 is the same models corresponding to middle panel but where the radial fundamental mode frequency difference between models, $f_1(i+1) - f_1(i)$, is plotted as a function of time. This shows that the resolution in the frequency space is as high as $0.18\ d^{-1}$ for this track[3]. The highest point is on the MS which should be taken into account for HD 187547. For 44 Tau, the focus for the resolution control should be much later on the post-MS.

Since 44 Tau has earlier been identified to be in the post-MS phase and the low value of $\log L/L_\odot$ for HD 187547 indicates an earlier stage on MS, the resolution of the models in `MESA` needs to be adjusted to allow for a higher chance of finding a good fit, particularly within these stages. It is possible to simply force smaller time steps, but this is not ideal since it would not only increase the computation time on the fast evolutionary stages, but the entire track. It is therefore favorable to consider an alternative parameter that does not spend computation in areas where it is not needed.

There are more than one way of achieving this. It is possible to set a limit for magnitude of maximum change in temperature and photosphere with the `delta_lgTeff_limit`, or alter the minimum and maximum number of grid points in a model with `mesh_delta_coeff` (a higher value decreases the number). The parameter found to be most efficient in this project is the `varcontrol_target` parameter. This parameter is assigned a value describing the relative variation in the structure from one model to the next. The timestep then adjusts accordingly, depending on whether the variation is smaller or

[3] Some tracks have poorer resolution of $0.2d^{-1}$

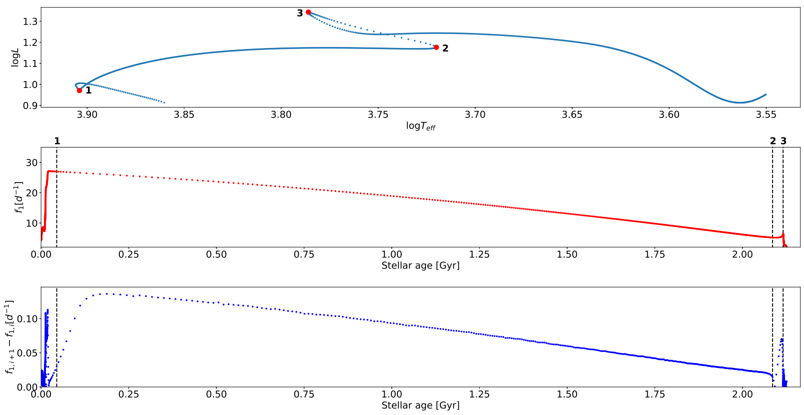

Figure 6.4: Resolution at different stages of an evolution of a track with M=1.85$M_{\odot}$, X=0.75, Z=0.02, $\alpha_{mlt} = 0.5$, $\alpha_{ov} = 0.3$. The beginning of the MS is marked with a bold "1", continuing until "2" where the post-MS contraction phase starts. At "3" all hydrogen has been exhausted in the core, and the star is in the post-MS expansion phase. Middle panel: Here the fundamental frequency is plotted as a function of time. The dashed lines indicate the stages corresponding to those in the middle panel. Lower panel: Shows the absolute difference in fundamental frequency between two subsequent models.

larger than the value. Increasing the resolution through this value does also increase the computation time. An example of this can be seen on Fig. 6.5 where the same track is plotted with different values of `varcontrol_target`. It is here found that a value of $5 \cdot 10^{-5}$ is sufficient in making the resolution satisfactory for this work.

Some tracks are still better resolved than others. A general tendency from the computed tracks are that models with overshoot below 0.2 are not resolved nearly as well as models with high overshoot of 0.3, which can also be seen on Fig. 6.6. Particularly the Henyey hook cannot be reproduced very well for overshoot of 0.1. The details as to why this occurs is beyond the scope of this work, however it is very important to take into consideration when evaluating results as tracks with low overshoot will automatically have fewer models and therefore limited chances of fitting well to observations.

## 6.3 $\chi^2$ testing

### 6.3.1 Finding the best model

In order to find out how well a model fits the data, a comparison with stellar parameters is needed. By just comparing models to $\log L/L_{\odot}$, $\log T_{\rm eff}$, and $\log g$, it is difficult to find an estimate on the evolutionary stage as the best model on one track might be on the main sequence, whereas the best model on a different track is on the post-main sequence. Therefore, frequencies are need

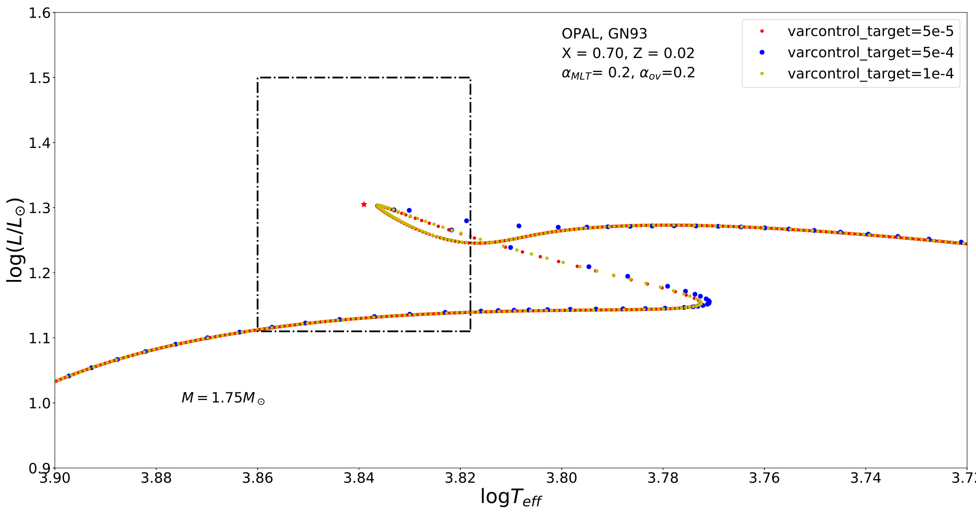


Figure 6.5: Evolution of three tracks with same initial parameters ($M = 1.75M_\odot$,$X = 0.70, Z = 0.02, \alpha_{mlt} = 0.2, \alpha_{ov} = 0.2$ ), but different values of `varcontrol_target` where $1 \cdot 10^{-4}$ is default in `MESA`. It can be seen that the resolution drops significantly for the value $5 \cdot 10^{-4}$. Therefore, a slightly smaller value of $5 \cdot 10^{-5}$ is chosen for this work. Observational uncertainties from parameters from Lenz et al. (2010) are marked as a black dashed errorbox.

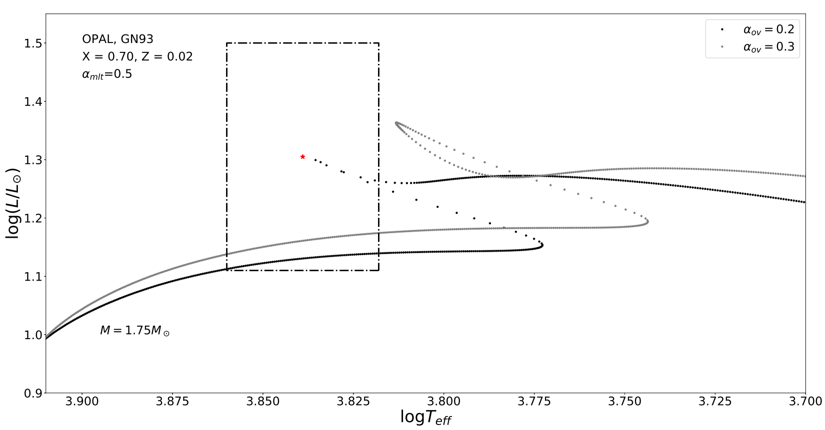


Figure 6.6: Evolution of a track with two different overshoot parameters. $M = 1.75M_\odot$,$X = 0.70, Z = 0.02, \alpha_{mlt} = 0.5$. Observational uncertainties from parameters from Lenz et al. (2010) are marked as a black dashed errorbox.

as additional observational parameters for comparison (as they, as discussed in Sec. 3, change with evolution). There is more than one way of doing the comparisons, but in this work a $\chi^2$ test is used. The $\chi^2$ test yields a value for each model, allowing to find models with lowest $\chi^2$ values. The Pearson's goodness of fit test is commonly written as

$$\chi_j^2 = \sum_{i=1}^{I} \left( \frac{x_{i,j}^{\mathrm{theo}} - x_i^{\mathrm{obs}}}{\sigma_i} \right)^2 , \tag{6.1}$$

where $x_i^{obs}$ is the observed parameter for the $i$'th fitting parameter (and $j$'th model), $x_i^{theo}$ is the corresponding theoretical parameter and $\sigma^i$ is the uncertainty of the $i$'th parameter. It provides a number that describes how close the fitting parameters are to the corresponding observed parameters. There are a few assumption that needs to be taken into consideration before implementing a $\chi^2$ test. Most importantly, statistically speaking, a $\chi^2$ test does not provide any information on how well individual parameters fit, or how likely a model is to be the best representative of the star. As the goal of this project is to estimate the evolutionary stage of the stars, the $\chi^2$ values can simply be used as a way of *comparing* between the different models. So models with the lowest $\chi^2$ are the models with parameters closest to the observed parameters. If the $\chi^2$ values are to be compared between the different models, then they need to be calculated under the same conditions. This means that calculations should be done with the same number of fitting parameters for all models (since they otherwise are not comparable). For instance, if one model have more fitted frequencies than another, the $\chi^2$ of that model will have more fitting parameters, causing it to naturally be larger than the $\chi^2$ for the model with fewer fitted frequencies, making their $\chi^2$ incomparable. This will be taken into consideration in the routine described in Sec. 6.3.2.2.

### 6.3.2 44 Tau

#### 6.3.2.1 Radial modes

For 44 Tau, the frequencies of the fundamental mode and first overtone are well-determined. These frequencies act as a constraint for the l=0 mode models. Initially the l=0 modes are computed using `GYRE` for the entire grid described in Sec. 6.1. Here, we have an initial constraint from only the frequencies corresponding to the radial fundamental mode, first overtone and the global parameters. The $\chi^2$ for this initial run then becomes

$$\begin{aligned} \chi_j^2 = & \left( \frac{\nu^{\mathrm{fund,obs}} - \nu_j^{\mathrm{fund,theo}}}{\sigma_{\mathrm{fund},j}} \right)^2 + \left( \frac{\nu^{\mathrm{first,obs}} - \nu_j^{\mathrm{first,theo}}}{\sigma_{\mathrm{first},j}} \right)^2 + \left( \frac{\mathrm{T}_{\mathrm{eff}}^{obs} - \mathrm{T}_{\mathrm{eff},j}^{\mathrm{theo}}}{\sigma_{\mathrm{T_{eff}},j}} \right)^2 \\ & + \left( \frac{\log \mathrm{g}^{\mathrm{obs}} - \log \mathrm{g}_j^{\mathrm{theo}}}{\sigma_{\log \mathrm{g},j}} \right)^2 + \left( \frac{\log \mathrm{L}^{\mathrm{obs}} - \log \mathrm{L}_j^{\mathrm{theo}}}{\sigma_{\log \mathrm{L},j}} \right)^2 , \end{aligned} \tag{6.2}$$

where $\chi_j^2$ is the $\chi^2$ for the $j$'th model. For $\log T_{\text{eff}}$, $\log g$ and $\log L/L_\odot$, the $\sigma$ used are the uncertainties from observations.

For the frequencies the $\sigma$ is naturally very small (in the order of $10^{-6}$), since the uncertainty on observations depend inversely on the observation time. Long observation times of 44 Tau therefore results in very narrow peaks. It is very nice to know a parameter to this precision, but as shown in Eq. 6.2 a small uncertainty will results in high values of $\chi^2$. High values of $\chi^2$ are not an issue in itself, as they are simply numbers for comparison. It does however mean that the frequencies will naturally be weighted higher. The model precision is simply not comparable to frequency precision. In other words, no model will ever get close to fitting well. Also, by only dividing by the uncertainties the resolution of the track is not taken into consideration. As shown in Sec. 6.2 the resolution of the track is important as fewer models in the same range decreases the possibility of having a good fit within that space. This also means that a model frequency can change a lot between two time steps if the resolution is low, and this should be taken into account. In this work the following prescription is therefore applied to the frequencies:

$$\chi^2 = \sum_{i=1}^{I} \frac{\left(v_i^{\text{obs}} - v_{i,j}^{\text{theo}}\right)^2}{(\sigma_i^{\text{obs}})^2 f_i(\Delta\nu_{i,j})} \tag{6.3}$$

where $i$ in this case is the different frequencies (i.e I=2 for $l = 0$ calculations where we only compare to fundamental frequency and first overtone) and $j$ is the $j$'th model. Lastly, $f_i(\Delta\nu_{i,j})$ is a function that artificially enhances the sigmas on the frequencies

$$f_i(\Delta\nu_{i,j}) = \frac{\nu_j - \nu_{j-1}}{\sigma_{\text{obs},i}}, \tag{6.4}$$

where the distance in frequency space is taken into consideration for the j'th model. Smaller distances in the frequency space between model means a higher $f_i(\Delta\nu_{i,j})$, hence, as smaller $\chi^2$. Runs both with and without the uncertainty pump will be made to test the difference in the main result.

As of yet only l=0 modes have been fitted. Calculating corresponding l=1 and l=2 modes for all models is time consuming, and therefore a selection criteria is needed. This is done by first finding the model with the lowest $\chi^2$ is for each track. From all of these the best 5% are found for both observational parameter sets as listed in Table 4.2. These models and their input parameters are shown in Table 6.2. The difference between the different runts can be seen in the last column.

Table 6.2: List of models that are within the 5% lowest $\chi^2$ values for 44 Tau.

| Model | $M[M_\odot]$ | X | Z | $\alpha_{mlt}$ | $\alpha_{ov}$ | Parameter set |
|---|---|---|---|---|---|---|
| 1238 | 1.50 | 0.65 | 0.01 | 0.2 | 0.3 | 1,2 |
| 1201 | 1.50 | 0.65 | 0.01 | 0.5 | 0.1 | 1,2 |
| 1211 | 1.50 | 0.65 | 0.01 | 0.5 | 0.3 | 1,2 |
| 1214 | 1.50 | 0.65 | 0.01 | 0.8 | 0.2 | 1,2 |

| | | | | | | |
|---|---|---|---|---|---|---|
| 1168 | 1.50 | 0.65 | 0.01 | 0.8 | 0.3 | 1,2 |
| 1190 | 1.55 | 0.65 | 0.01 | 0.2 | 0.2 | 1,2 |
| 1411 | 1.60 | 0.70 | 0.01 | 0.2 | 0.3 | 1,2 |
| 1434 | 1.60 | 0.70 | 0.01 | 0.5 | 0.3 | 1,2 |
| 1244 | 1.60 | 0.70 | 0.01 | 0.8 | 0.3 | 1,2 |
| 1353 | 1.60 | 0.70 | 0.01 | 0.8 | 0.3 | 1,2 |
| 1204 | 1.60 | 0.70 | 0.01 | 0.5 | 0.1 | 1,2 |
| 1264 | 1.60 | 0.70 | 0.01 | 0.8 | 0.1 | 1,2 |
| 1384 | 1.65 | 0.70 | 0.01 | 0.2 | 0.2 | 1,2 |
| 1428 | 1.65 | 0.70 | 0.01 | 0.5 | 0.2 | 1,2 |
| 1328 | 1.65 | 0.70 | 0.01 | 0.2 | 0.2 | 1,2 |
| 1289 | 1.65 | 0.70 | 0.01 | 0.2 | 0.3 | 1,2 |
| 1353 | 1.701 | 0.65 | 0.02 | 0.2 | 0.1 | 2 |
| 1144 | 1.701 | 0.65 | 0.02 | 0.5 | 0.2 | 1,2 |
| 1121 | 1.701 | 0.65 | 0.02 | 0.8 | 0.1 | 2 |
| 1131 | 1.701 | 0.65 | 0.02 | 0.8 | 0.2 | 2 |
| 1140 | 1.701 | 0.75 | 0.01 | 0.8 | 0.3 | 1 |
| 1290 | 1.701 | 0.75 | 0.01 | 0.5 | 0.3 | 2 |
| 1148 | 1.701 | 0.75 | 0.01 | 0.8 | 0.2 | 2 |
| 1126 | 1.701 | 0.65 | 0.02 | 0.8 | 0.1 | 1 |
| 1273 | 1.75 | 0.75 | 0.01 | 0.2 | 0.2 | 1,2 |
| 1187 | 1.75 | 0.75 | 0.01 | 0.5 | 0.2 | 1,2 |
| 1216 | 1.75 | 0.65 | 0.02 | 0.2 | 0.2 | 1 |
| 1231 | 1.75 | 0.65 | 0.02 | 0.2 | 0.3 | 1,2 |
| 1158 | 1.75 | 0.65 | 0.02 | 0.5 | 0.3 | 1,2 |
| 1177 | 1.80 | 0.70 | 0.02 | 0.2 | 0.2 | 1,2 |
| 1165 | 1.80 | 0.70 | 0.02 | 0.5 | 0.3 | 1,2 |
| 1271 | 1.85 | 0.70 | 0.02 | 0.2 | 0.2 | 1,2 |
| 1089 | 1.85 | 0.70 | 0.02 | 0.5 | 0.2 | 1,2 |
| 1065 | 1.85 | 0.70 | 0.02 | 0.8 | 0.2 | 1,2 |
| 1137 | 1.85 | 0.65 | 0.03 | 0.2 | 0.1 | 1,2 |
| 1230 | 1.85 | 0.65 | 0.03 | 0.2 | 0.3 | 1 |
| 1025 | 1.85 | 0.65 | 0.03 | 0.8 | 0.2 | 1,2 |
| 1219 | 1.90 | 0.70 | 0.02 | 0.2 | 0.3 | 1,2 |
| 1074 | 1.90 | 0.70 | 0.02 | 0.5 | 0.2 | 1,2 |
| 1071 | 1.90 | 0.70 | 0.02 | 0.8 | 0.2 | 1,2 |
| 1086 | 1.95 | 0.75 | 0.02 | 0.5 | 0.1 | 1 |
| 1072 | 1.95 | 0.75 | 0.02 | 0.8 | 0.1 | 1,2 |
| 1023 | 1.95 | 0.70 | 0.03 | 0.8 | 0.2 | 1,2 |
| 1088 | 2.0 | 0.75 | 0.02 | 0.5 | 0.1 | 1,2 |
| 1069 | 2.0 | 0.75 | 0.02 | 0.5 | 0.2 | 1,2 |
| 1050 | 2.0 | 0.75 | 0.02 | 0.8 | 0.1 | 1,2 |
| 1046 | 2.0 | 0.75 | 0.02 | 0.8 | 0.2 | 1,2 |
| 1123 | 2.0 | 0.70 | 0.03 | 0.2 | 0.2 | 1,2 |
| 1030 | 2.0 | 0.70 | 0.03 | 0.5 | 0.1 | 1,2 |
| 1010 | 2.0 | 0.70 | 0.03 | 0.8 | 0.1 | 1,2 |
| 1151 | 2.05 | 0.75 | 0.02 | 0.2 | 0.1 | 1,2 |

| | | | | | | |
|---|---|---|---|---|---|---|
| 1129 | 2.05 | 0.70 | 0.03 | 0.2 | 0.1 | 1,2 |
| 994 | 2.05 | 0.70 | 0.03 | 0.8 | 0.2 | 1,2 |
| 1156 | 2.10 | 0.75 | 0.02 | 0.2 | 0.2 | 1,2 |
| 1073 | 2.10 | 0.75 | 0.02 | 0.8 | 0. 3 | 1,2 |
| 1090 | 2.10 | 0.70 | 0.03 | 0.5 | 0.3 | 1,2 |
| 1010 | 2.15 | 0.75 | 0.03 | 0.5 | 0.2 | 1,2 |
| 1219 | 2.20 | 0.75 | 0.03 | 0.2 | 0.3 | 1,2 |
| 1055 | 2.20 | 0.75 | 0.03 | 0.5 | 0.1 | 1,2 |
| 1087 | 2.20 | 0.75 | 0.03 | 0.5 | 0.3 | 1,2 |
| 1034 | 2.20 | 0.75 | 0.03 | 0.8 | 0. | 1,2 |
| 979 | 2.20 | 0.75 | 0.03 | 0.8 | 0.2 | 1,2 |
| 1068 | 2.20 | 0.75 | 0.03 | 0.8 | 0.3 | 1,2 |

By first selecting the model with the lowest $\chi^2$ value for each track, a wide range of parameter combinations is ensured. It forces an estimate on the evolutionary stage at all areas of the grid, including the very outskirts. The disadvantage of this is that it makes it more difficult to identify the most likely parameter combination, since there cannot be more than one model in the 5% range on a track. However, as the end goal is to find an estimated evolutionary stage and a single best model, the method is adequate.

Since $\chi^2$ only provide a value to compare to other models, it does not give an indication of how likely a parameter space is. This also means that the $\chi^2$ for the frequency space can deviate a lot from the $\chi^2$ from the other observable parameters. To ensure that the 5% models are also within the observable parameter space of $\log g$ and $\log T_{\text{eff}}$, a scatter plot is made which can be seen on Fig. 6.7.

Here, $\log g$ is plotted as a function of $\log T_{\text{eff}}$ and color coded with the corresponding $\chi^2$. The $1\sigma$ uncertainty on $\log g$ and $\log T_{\text{eff}}$ is marked with a black stippled line. Some of the scatter plots shows expected tendencies such as $\log L/L_{\odot}$, $\log g$, $\log T_{\text{eff}}$ and profile numbers. Since higher profile number is at a later stage[4], the effective temperature is much lower for lower profile numbers.

The lowest $\chi^2$ seems to linearly decrease with $\log T_{\text{eff}}$. This is because $\log g$ is strongly related to $\rho$ (hence, $\Delta\nu$ and $\log T_{\text{eff}}$). For the element abundances, there is a trend a that lower values of $\log g$ yield lower values of Z and X, in particular. This falls out of Eq. 2.13 as high abundances of hydrogen and/or metallicity causes a lower mean molecular weight $\mu$. Since $\mu \propto \rho \propto g$, a smaller value of X or Z yields a smaller value for g as well. Since $g$ is also directly proportional to the mass, the mass decreases with $\log g$ in the plot as well.

There seems to be no recognizable trend in the $\alpha_{mlt}$ and $\alpha_{ov}$ color coding. Since there is a definite correlation between the convection and structure of the star, it would be expected to see a trend between the mixing length or overshoot parameter and $\log g$ and $\log T_{\text{eff}}$. Since this sample is small, it cannot be excluded that there is a trend that can be found if more data points are included.

[4]Note that the profile number does only indicate the stage of that individual track i.e profile number 900 on one tracks is not necessarily at the same stage for the same profile number on a different track.

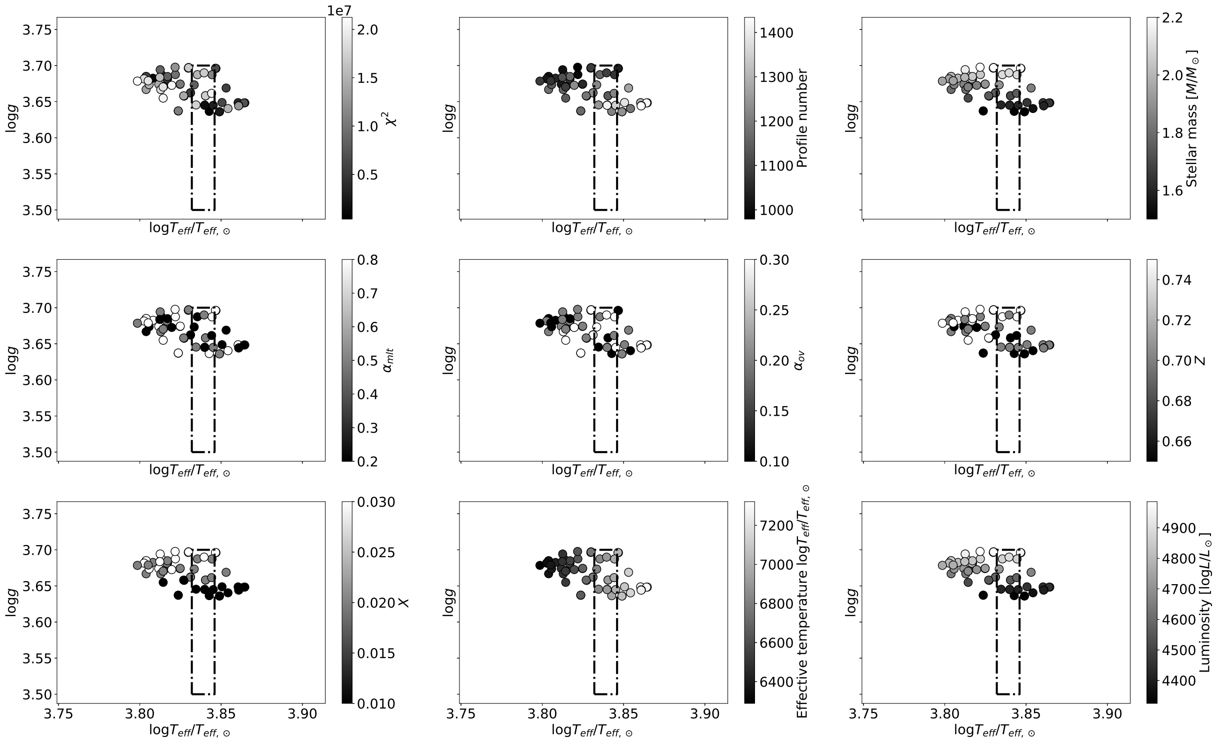


Figure 6.7: Scatter plots showing $\log T_{\rm eff}$, $\log g$ color coded with nine different parameters for the 5% best models (without resolution control). The plots color coded with $\log T_{\rm eff}$ and $\log g$ are plotted to show that the plotting method works correctly. The run was made with the Lenz obsevational parameters set.

#### 6.3.2.2 Nonradial modes

A new calculation is conducted in `GYRE` for $l = 0, 1, 2$ modes for all of the 5% models. The frequencies produced gives a further constrain of the best models as all frequencies can now be compared with observations.

Calculations of $\chi^2$ are conducted based on the fact that $n$ and $l$ is known for the models, but does not include a comparison to $l$ of the observed models. To ensure that the $\chi^2$ are comparable between each model, as mentioned earlier, the models all need to have the same amount of fitting parameters. This is not an issue in the initial $\chi^2$ calculations with $l$=0, since this $\chi^2$ is only based on the same two frequencies for all models. But including $l = 1$ in the calculations require that all observed frequencies are fitted to a corresponding theoretical match (so if the number of theoretically produced frequencies is lower than the observed, the model will be excluded).

It is carried out in the following way: for each model, each individual model-frequency is compared to all observed frequencies and the best match (i.e. the smallest difference) is thereby assumed to be the closest frequency.

This is repeated from the lowest to highest frequency until all model-frequencies have been given a best match observation frequency. This means that the observed frequency will be given the $n$ and $l$ of the best matching model frequency. Each model then has an estimated set of frequencies where $\chi^2$ can be computed. It does not take into consideration that the radial fundamental mode and first overtone are already determined (and might match it to n that are higher, however these models should be excluded as their match will not be good if the two first frequencies do not match expectations). This yields

$$\chi^2 = \left(\frac{\nu^i_{\text{all,obs}} - \nu^i_{\text{all,theo}}}{\sigma^i_{\text{first}}}\right)^2 + \left(\frac{\mathrm{T}^i_{\text{eff,obs}} - \mathrm{T}^i_{\text{eff,theo}}}{\sigma^i_{\mathrm{T_{eff}}}}\right)^2 + \left(\frac{\log \mathrm{g}^i_{\text{obs}} - \log \mathrm{g}^i_{\text{theo}}}{\sigma^i_{\log \mathrm{g}}}\right)^2 + \left(\frac{\log \mathrm{L}^i_{\text{obs}} - \log \mathrm{L}^i_{\text{theo}}}{\sigma^i_{\log \mathrm{L}}}\right)^2. \tag{6.5}$$

From these, the models with the lowest $\chi^2$ is found for the two different luminosities respectively.

As mentioned, this routine does not take the identified $l$ into account. The first way to do so is to weight each frequency individually by including a comparison between theoretically produced $l$ and the one from mode identification. Though this method probably provides a more detailed and statistically stringent result, it is does require a thorough estimate and evaluation of the single frequencies, which is beyond the scope of this work.

### 6.3.3 Results

The best models found for the two different runs of 44 Tau are shown in Table 6.3 and Table 6.4. The variation from parameter set 1 and parameter set 2 does not affect the total result, as the $\chi_{tot}$ does not differ down until a factor $10^{-13}$. It does however shift the best found model if only including the observational parameters. The reason for this is that the frequencies weigh more in the $\chi^2$ than the observational parameters. Artificially enhancing the frequencies does shift the model to a higher mass (closer to the mass estimated by Lenz et al. (2010)), but the $\chi^2_{tot}$ is higher for this model. Enhancing the uncertainties corresponds to adding a weight to the frequencies. However, the difference between the weighted and unweighted results is of order 1, not changing overall result that frequencies still dominates the final outcome.

The green points tend to overlap the red points, which again indicates that the frequencies are highly more weighted than the observational parameters. The frequencies thereby controls the final outcome, explaining why there is no difference in the main result by changing between the two runs for different observational parameter sets. The best model places 44 Tau on the post-MS, evolved further than result from Lenz et al. (2010) whereas the best model with artificially pumped frequencies is earlier in its evolution. Both of these are within the three-sigma uncertainty of the observations (inside the errorbox). The frequency fit for the best model and best pumped model can be seen on Fig. 6.9, Fig. 6.10, respectively.

Table 6.3: Best models for the two different observed parameter sets for 44 Tau. The two different parameter sets yielded the same overall result for best model. The difference in the $\chi^2$ between the two parameter sets is0 insignificant (in the order of $10 \cdot^{-13}$ except for the best $\chi^2_{obs}$: The best frequency model is therefore the same as the total best model, since the $\chi^2_{freqs}$ completely dominates the $\chi^2_{tot}$, and there therefore is no significant difference between best $\chi^2_{tot}$ and $\chi^2_{freqs}$.

| Profile | $M[M_\odot]$ | X | Z | $\alpha_{mlt}$ | $\alpha_{ov}$ | $\chi^2_{tot}$ | $\chi^2_{freqs}$ | $\chi^2_{obs}$ | $\chi^2_p$ | Parameter set reference |
|---|---|---|---|---|---|---|---|---|---|---|
| 1190 | 1.55 | 0.65 | 0.01 | 0.8 | 0.1 | $6.2814 \cdot 10^8$ | $6.2814 \cdot 10^8$ | 5.5763 | $6.1377 \cdot 10^8$ | Lenz et al. (2010)/Brown et al. (2018) |
| 1411 | 1.60 | 0.70 | 0.01 | 0.2 | 0.2 | $9.0844 \cdot 10^9$ | $9.0844 \cdot 10^9$ | 0.2238 | $1.6366 \cdot 10^9$ | Lenz et al. (2010) |
| 1384 | 1.65 | 0.70 | 0.01 | 0.2 | 0.2 | $1.6275 \cdot 10^9$ | $1.6275 \cdot 10^9$ | 3.7506 | $3.1659 \cdot 10^9$ | Lenz et al. (2010)/Brown et al. (2018) |
| 1090 | 2.10 | 0.70 | 0.03 | 0.5 | 0.3 | $1.6487 \cdot 10^{10}$ | $1.6487 \cdot 10^{10}$ | 1.3523 | $1.2282 \cdot 10^{10}$ | Brown et al. (2018) |

Table 6.4: Continued table from Table 6.3, containing the theoretically produced parameters for the best models.

| Profile | $\log T_{\text{eff}}$ | $\log g$ | $\log L/L_{\odot}$ | age [Gyr] |
|---|---|---|---|---|
| 1190 | 3.8542 | 3.6405 | 1.3582 | 1.1966 |
| 1411 | 3.8399 | 3.6450 | 1.3100 | 1.6019 |
| 1384 | 3.8506 | 3.6488 | 1.3624 | 1.4652 |
| 1090 | 3.8400 | 3.6900 | 1.3819 | 1.1188 |

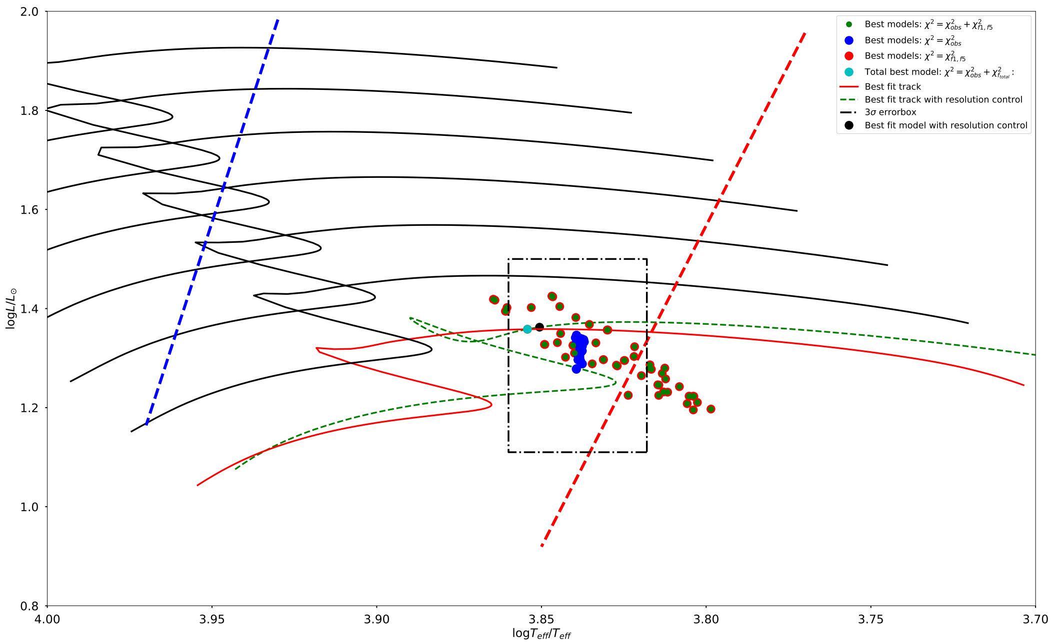


Figure 6.8: HRD where the best model is estimated to be $M = 1.55M_{\odot}$, $X = 0.65$, $Z = 0.01$, $\alpha_{mlt} = 0.5$, $\alpha_{ov} = 0.1$. The best total model is marked with a cyan blue dot, on the track marked with red. The green points shows the best 5% models if the criteria is the total $\chi^2$. Blue dots are the 5% best models if only observational parameters is included in the $\chi^2$, whereas the red dots is the 5% if the $\chi^2$ is only calculated from the frequency fits. The green tracks shows the best track with the black dot marking the best model if the frequency uncertainties have been artificially enhanced as in Eq. 6.3. This track has the parameter combination of $M = 2.05$ ,$X = 0.70$, $Z = 0.03$, $\alpha_{mlt} = 0.5$ and $\alpha_{ov} = 0.3$.

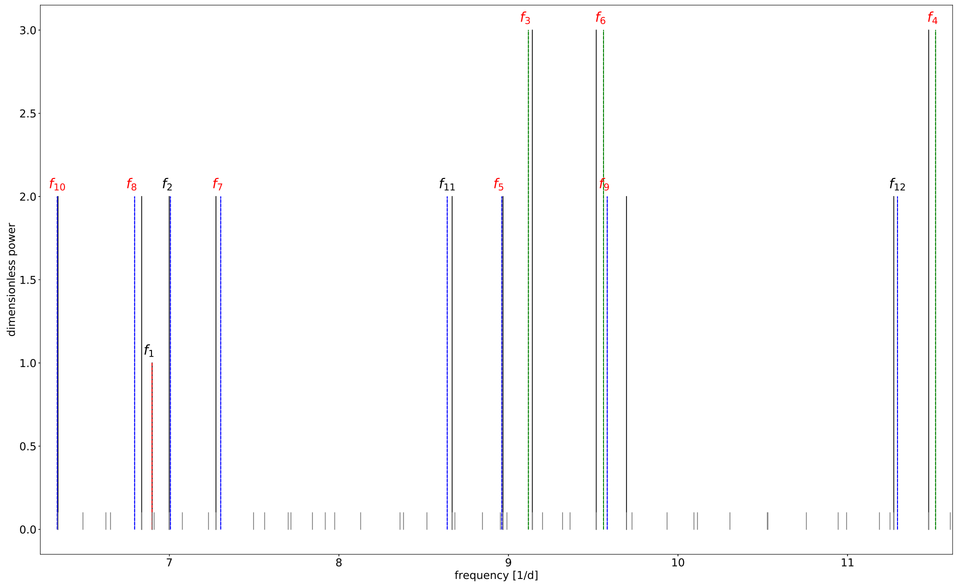


Figure 6.9: Color-coded frequency plot of the best total model. These are color-coded by the spherical degree as follows: $l = 0$ are red, $l = 1$ are blue and $l = 2$ are green, with dimensionless powers of 1,2 and 3. The black lines indicate the matched theoretical frequency, and the gray lines at the bottom represents all theoretically produced frequencies. The naming convention of the modes correspond to that of Lenz et al. (2010). Stippled lines are lines of uncertainty on the frequencies, although these are so small that they are not visible.

The naming convention of the frequencies are defined as in Table 4.1. Stippled lines are lines of uncertainty on the frequencies, although these are so small that they are not visible. Since the uncertainty is so small, technically none of the theoretical frequencies are matched within the uncertainties. However, they are all matched within a range of $0.2d^{-1}$. The text marked with red are indicates where the estimated modes from mode identification is different from the theoretically calculated spherical degrees. To indicate that some models might be better estimates for the star, a frequency fit of the track $M = 1.65$, $X = 0.70$, $Z = 0.01$, $\alpha_{mlt} = 0.5$, $\alpha_{ov} = 0.3$ is shown of Fig. 6.12[5]. Here, only two modes could differ in spherical degree from the mode identification. The corresponding HRD is shown on Fig. 6.13. Here, the evolutionary stage is pushed back to the Henyey hook, closer to the results of Lenz et al. (2010)[6]. Therefore, for future work it is necessary to implement a routine weighing the different frequencies depending on the mode identification as well.

[5]This run includes pre-MS models as well. These do not influence the minimum $\chi^2$ of this run

[6]This run was made without the cutoff at profile $> 900$, meaning that pre-MS models are included. They are located at the bottom right corner

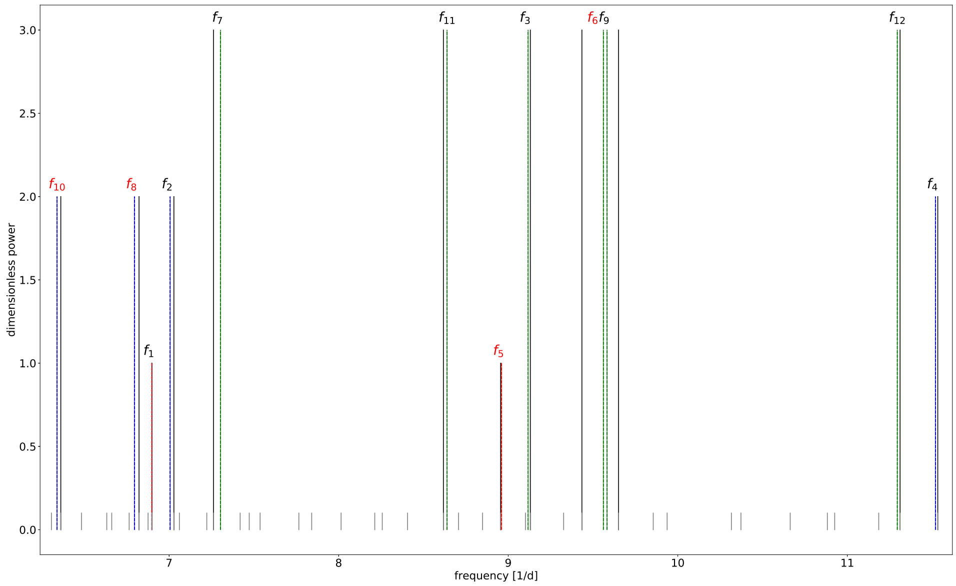


Figure 6.10: Frequency fit for best model with artificially enhanced uncertainties on the frequencies. Same color coding as Fig. 6.9.

There can be other reasons for the contradictions in spherical degree : 1) The pulsation code does not calculate the theoretically produced frequencies correctly. At this point it is already a well-known issue that the theory behind these type of oscillations does not comply well with observations. Lenz et al. (2010) was indeed successful with modeling 44 Tau, but this example is the first one of its kind where all identified modes where reproduced theoretically. More often, pulsation codes does not match observations. 2) Due to the high uncertainty in mode identification, some of the modes have been misidentified. This is the more likely scenario since 1) would probably cause issues for more than two modes, and would not have been able to fit the rest either. There is also strong evidence that some modes could be identified wrongly due to the model dependency of the mode identification. It can be seen on Fig. 6.11 that the choice of mixing length affects the mode identification significantly. The theoretically predicted regions for $l = 0, 1, 2$ are marked with red, green and blue respectively. Observations are plotted with black boxes. For small values of $\alpha_{mlt}$ the regions tend to move closer, making it difficult to distinguish between spherical degree. These models are based on frozen convection where the mixing length describes the local convection. However, time-dependent convection is needed in order to describe the full picture of convection, and the difference in mode identification is significant (Dupret et al., 2005),(Victoria Antoci 2019, private communication).

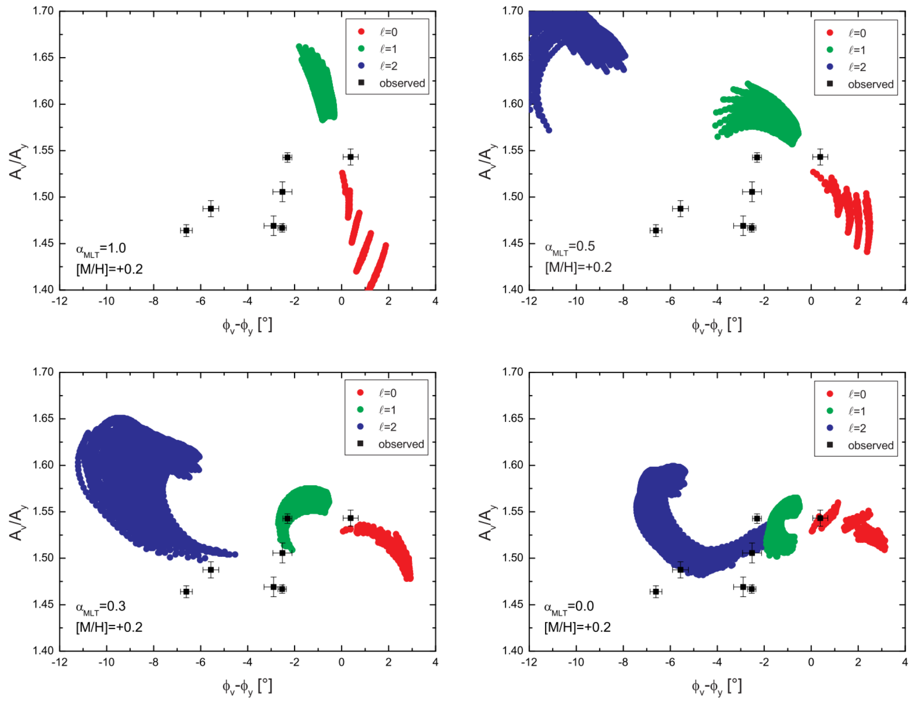


Figure 6.11: Predicted theoretical model position for four different values of the mixing length parameter $\alpha_{mlt}$. Figure from Lenz (2009)

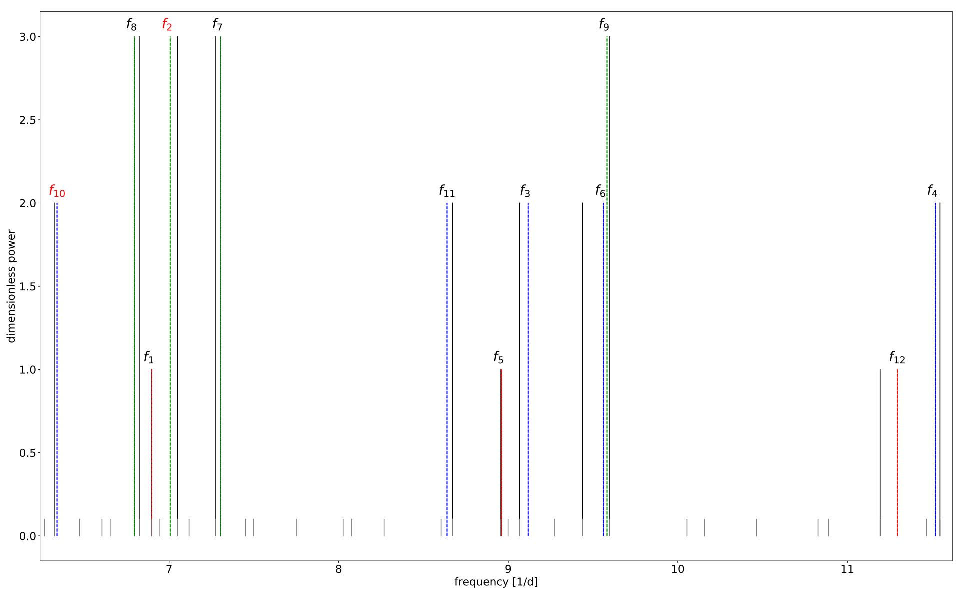


Figure 6.12: Frequency fit for $M = 1.65 M_\odot$, $X = 0.70$, $Y = 0.01$, $\alpha_{mlt} = 0.5$, $\alpha_{ov} = 0.3$. Color coding as Fig. 6.9.

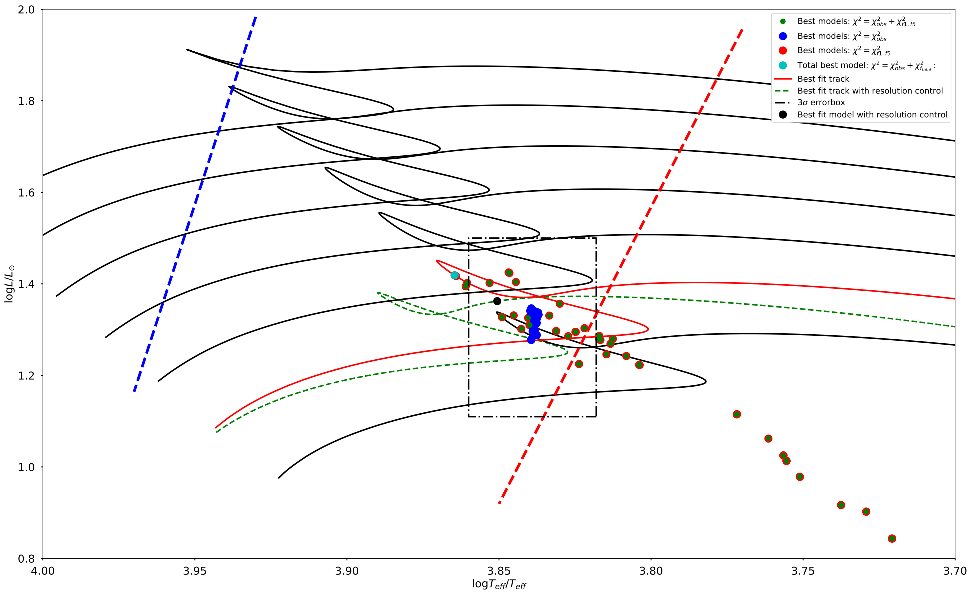


Figure 6.13: HRD where the best model is estimated to be $M = 1.65 M_\odot$, $X = 0.70$, $Y = 0.01$, $\alpha_{mlt} = 0.5$, $alpha_{ov} = 0.3$.

## 6.4 HD 187547

On the contrary to 44 Tau, no modes are well enough determined to use an initial constraint for the models of this star. Instead of fitting the frequencies it is therefore more favourable to fit the large frequency separation, now defined as

$$\Delta\nu = \nu_{n+1} - \nu_n, \tag{6.6}$$

the frequency difference between two ($l$=0) consecutive frequencies with same $l$[7]. The $\chi^2$ can now be calculated using the observed large frequency separation of $3.5d^{-1}$ AND $7d^{-1}$ (Antoci et al., 2014). Results are shown shown in Table **??**.

For modes higher than $l$=0, calculating the $\chi^2$ for HD 187547 is more elaborate than for 44 Tau, since it is based on the large frequency separation. When $l > 0$ , the frequency separation depends significantly on the mixed modes and radial order. Therefore, this part is beyond the scope of this work.

[7]This is not the same frequency separation as in Eq. 3.10. Thjs does not require $n \ll l$ and is not necessarily asymptotic. Therefore, the values calculated for $\Delta f$ are not to be compared with $\Delta\nu$. For Antoci et al. (2011) these were assumed to be the same as the HD 187547 was assumed to have solar-like oscillations in this region where the asymptotic relation applies.

### 6.4.1 Results

The best models for the two different HD 1987547 runs can be seen in Table 6.5. The best model of the respective $\chi^2$ is marked with red. For $\Delta\nu = 3.5d^{-1}$ the best model based on $\chi^2_{tot}$ with a theoretical $\Delta f = 3.5672$. Only looking at the $\chi^2_{sep}$, the best model will be slightly shifted, and obtain a significantly higher $\chi^2_{tot} = 1254$. This is indicates that if the large frequency separation fits well, the observable parameters will not fit nearly as well. The model with the best $\chi^2_{obs}$ does indeed have a $\Delta f \approx 6d^{-1}$, significantly higher than $3.5d^{-1}$. This strengthens the suspicion that $3.5d^{-1}$ is too low to match the observed parameters. This can also be seen on Fig. 6.14, as the best total track is forced outside the bounds of the instability strip. From the placement of the 5% best models it can be seen that the separation is closely related to the evolutionary stage (as they tend to line up along the same stage of the tracks. ) There is not overlap between the models for $\chi^2_{sep}$ and $\chi^2_{obs}$. The best combined modes therefore match the luminosity relatively, but is not within the errrorbox of the $\log T_{\rm eff}$, or $\log L/L_\odot$. The best model (marked in black) does place HD 187547 on the main-sequence, however to the right of the red edge, pushing it outside of the instability strip.

Increasing the large frequency separation to $\Delta\nu = 7d^{-1}$ yields the result shown in Fig. 6.15.

The best track in this case is still on a low mass of $M = 1.55M_\odot$, but is now inside the red edge of the instability strip. This also puts HD 187547 at a stage very early on the MS. There is now an overlap between the best models from separation and the best models for parameters. The $\chi^2_{tot}$ is lower than for the run with $\Delta\nu = 3.5d^{-1}$, suggesting a better fit. What is to be noted is that the best model for the separation only ($\chi_{sep}$) is smallest on a track with a significantly higher mass $M = 2.05M_\odot$. The $\chi^2_{tot}$ however, is much larger.

If HD 187547 is on the PMS we would expect features from different metallic lines and dust to appear in the spectrum, however no so observations indicate that this should be the case. As mentioned, the PMS tracks in `MESA` made in this work should not be trusted for the purpose of asteroseismic modeling, since the are all products of the same relaxed pre-calculated PMS model. Therefore, the results are forced on to the MS by making a cutoff at profile 900. This is a rough cutoff since profile 900 on one tracks is not necessarily an indication of the same stage for the same profile on another track. This cutoff is marked with a black vertical dashed line on Fig. 6.16. The frequency separation $\Delta f$ is shown on Fig. 6.16. It can be seen that the large frequency separation decreases somewhat linearly on the MS, until reaching the post-MS phases. The model cutoff in this case (best model for HD 187547) excludes only models on the PMS, yet also includes some models that should not be included. Therefore, this cutoff method should be reconsidered.

A more secure way do it would be to evaluate the helium content in the core and set a limit for the gradient (i.e., defining the ms at a certain limit for an increase in helium in the core). This would however require an individual assessment of each track and is therefore beyond the scope of this work.

Table 6.5: Best models for superstar with the two different $\Delta\nu$ . The $\chi^2$ are calculated by comparing theoretical parameters with the observational parameters are $\log T_{eff} = 3.875 \pm 0.011$, $\log g = 3.9 \pm 0.2$ and $\log L/L_{\odot} = 0.859 \pm 0.003$. The best $\chi^2$ value for the different parts of the $\chi^2$ is marked in red.

| profile | M[$M_{\odot}$] | X | Z | $\alpha_{mlt}$ | $\alpha_{ov}$ | $\log T_{\text{eff}}$ | $\log g$ | $\log L/L_{\odot}$ | Age [Gyr] | $\chi^2_{tot}$ | $\chi^2_{obs}$ | $\chi^2_{sep}$ | $\Delta f_{theo}$ | $\Delta\nu_{obs}[d^{-1}]$ |
|---|---|---|---|---|---|---|---|---|---|---|---|---|---|---|
| 1144 | 1.50 | 0.65 | 0.03 | 0.2 | 0.3 | 3.727 | 3.604 | 0.873 | 2.540 | 70.399 | 68.595 | 1.8049 | 3.5672 | 3.5 |
| 964 | 1.50 | 0.75 | 0.01 | 0.8 | 0.2 | 3.873 | 4.201 | 0.859 | 1.254 | 2728.3 | 2.3180 | 2726.0 | 6.1105 | 3.5 |
| 1128 | 1.75 | 0.75 | 0.02 | 0.2 | 0.2 | 3.808 | 3.840 | 1.025 | 1.802 | 2605.9 | 2605.9 | $1.2759 \cdot 10^{-9}$ | 3.5000 | 3.5 |
| 991 | 1.55 | 0.75 | 0.01 | 0.5 | 0.1 | 3.8933 | 4.2949 | 0.8601 | 0.6093 | 6.5110 | 6.4926 | 0.0166 | 6.9932 | 7.0 |
| 964 | 1.50 | 0.75 | 0.01 | 0.8 | 0.2 | 3.873 | 4.201 | 0.859 | 1.254 | 318.77 | 2.318 | 316.46 | 6.1105 | 7.0 |
| 966 | 2.05 | 0.70 | 0.01 | 0.2 | 0.1 | 4.0244 | 4.3283 | 1.4721 | 0.0061 | 35171 | 35171 | $9.5566 \cdot 10^{-9}$ | 7.0000 | 7.0 |

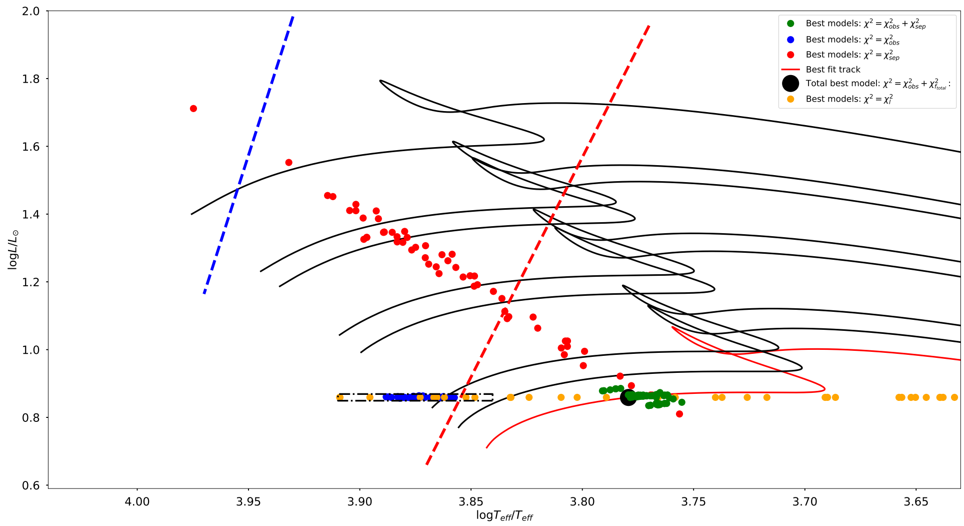


Figure 6.14: HRD for HD 187537. The tracks for which $\chi^2_{tot}$ icds lowest is marked with red. The black tracks have the same parameter combinations as the best track but with masses varying from $M = 1.55$ to $M = 2.2\ M_\odot$. The red dots are the plotted 5% best models based on the $\chi^2$ from the separation only ($\chi^2_{sep}$). Here, $\Delta\nu = 7^d{-}1$ The blue points are the best 5% for observed parameters $\chi_{obs}$, and the green dots for the combined $\chi^2_{tot}$. The orange dots indicates best models for $\chi^2$ calculated based on $\log L/L_\odot$. Three sigma observed uncertainties are marked with a black dashed line as an errorbox. The instability strip is marked with the blue and red edges from Murphy et al. (2019).

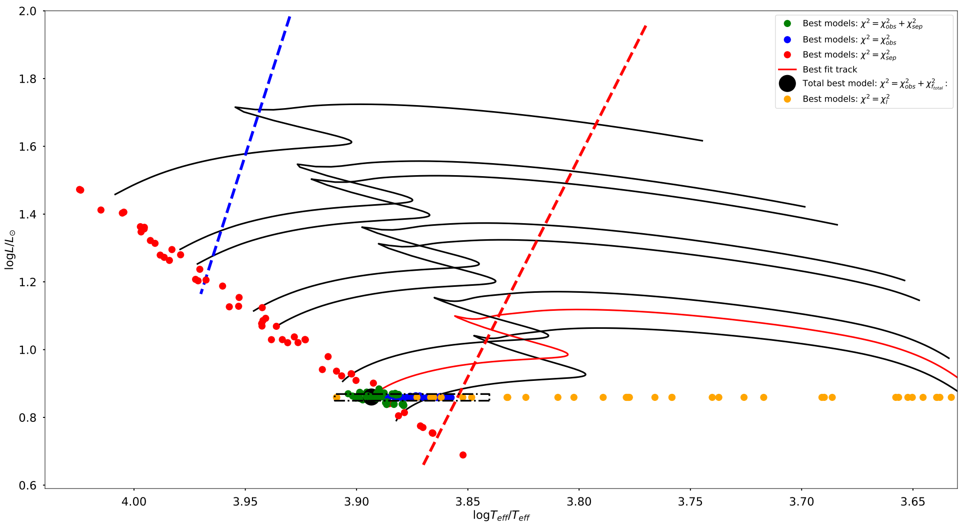


Figure 6.15: HR diagram for HD 187537, corresponding to Fig. 6.14 but with $\Delta\nu = 3.5^{-1}$ . The tracks for which the total $\chi^2$ is lowest is marked with red. The black tracks have the same parameter combinations as the best track but with masses varying from $M = 1.55$ to $M = 2.2\ M_{\odot}$. The red dots are the plotted 5% best models based on the $\chi^2$ from the separation only ($\chi^2_{sep}$). The blue points are the best 5% for observed parameters $\chi_{obs}$, and the green dots for the combined $\chi^2_{tot}$. The orange dots indicates best models for $\chi^2$ calculated based on $\log L/L_{\odot}$. Three sigma observed uncertainties are marked with a black dashed line as an errorbox. The instability strip is marked with the blue and red edges from Murphy et al. (2019).

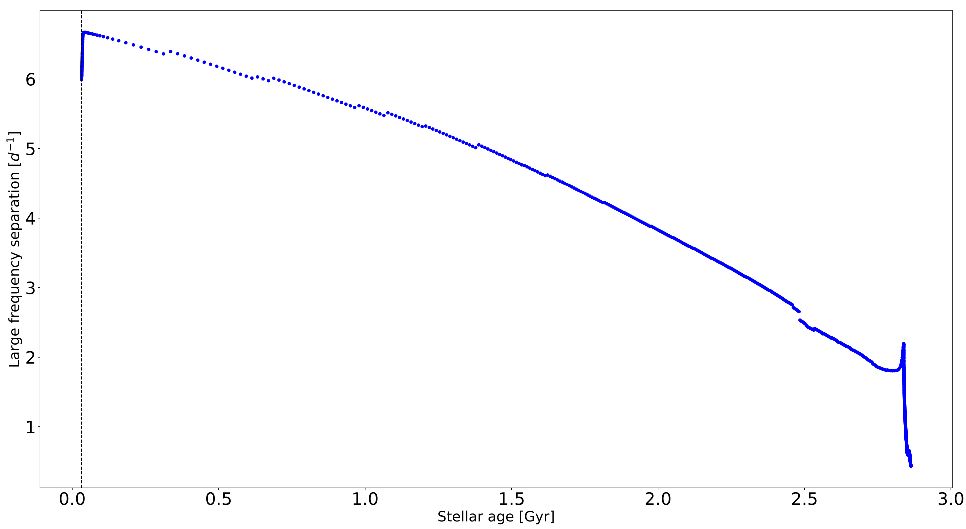


Figure 6.16: Large frequency separation as a function of evolution for a track wit h$M = 1.5M_{\odot}$, $X = 0.65$, $Z = 0.03$, $\alpha_{mlt} = 0.2$ and $\alpha_{ov} = 0.3$.

# 7 Discussion and future work

In this chapter the results will be discussed in more detail for the purpose of proposing any issues and aspects that needs to be addressed in future work for obtaining further knowledge and improvement of the field.

## 7.1 Grid considerations

The grid of tracks constructed for this project proves sufficient for providing an estimate on the range in the evolutionary stage for 44 Tau and HD 187547. It stretches from a mass of 1.5 to 2.2 $M_{\odot}$ to cover up most of the instability strip in the parameters space. However, as $\delta$ Sct stars have been observed even outside of the instability strip, it is important to include that possibility of more extreme parameter space possibilities. Therefore, further analysis in the future should include a more detailed evaluation of the outer grid bounds to analyze the probability of the best fit models in those ranges. As the exact position of the instability strip is still a big discussion topic in the field of asteroseismology of $\Delta$ Sct stars (Murphy et al., 2019), a larger grid including masses up to 2.5 $M_{\odot}$ should be included in the grid to ensure full coverage.

Since $\alpha_{mlt}$ is a purely empirical parameter and therefore not directly applicable in analytical solutions, there are not many guidelines as how to the range in the grid should be chosen. Here, smaller values were initially chosen due to two reasons: Firstly, the values for the mixing length parameter used in Lenz et al. (2010) is as low as $\alpha_{mlt} = 0$. Hence, the values in this project must be correspondingly small in order to compare results more easily. However, this argument becomes faulty as soon as the implementations of $\alpha_{mlt}$ is not the same in both stellar structure and evolution codes, meaning that the same number has different interpretations. Although, secondly, one might still argue that such small values still is a good estimate for stars with very small convective envelopes, since the convection is not efficient. This is very much still up for discussion, since convective efficiency and how it affects the excited frequencies, despite efforts (references), still lacks understanding. For this project, the effects of different mixing length throughout the HRD is shown on Fig. 5.1, and as earlier discussed in Sec. 5 it primarily has affects the star in the late stage of the subgiant phase.

The choice of a consistently small $\alpha_{mlt}$ could potentially cause a bias in the best 5% as $\alpha_{mlt}$ correlates with the structure of the star (and thereby the frequencies). For future work, it would therefore be necessary to extend the $\alpha_{mlt}$ to values as high as the standard solar value of 1.8 in `MESA`. This ensures the exclusion of unconscious bias from the grid choice.

As mentioned in Sec. 6.3.2, the uncertainties of the frequencies are very small, causing the values of the total $\chi^2$ is completely controlled by the frequencies. A method taking the resolution into consideration was implemented for the purpose of weighing the frequencies with the resolution through Eq. 6.4. This did yield lower values of $\chi^2$, but not nearly enough to make the uncertainties of the frequencies the same order as the rest of the fitting parameter uncertainties. It can also be argued that frequencies should naturally be weighed higher as the observations have smaller uncertainties, and that the $\log g$, $\log T_{\text{eff}}$, and $\log L/L_{\odot}$ should be given correspondingly smaller weights due to higher uncertainties (and disagreements between spectroscopic and photometric values). However, this does cause the frequencies to weigh much more than the remaining parameters, and it would therefore be relevant to conduct an implementation of more thoroughly selected weights for all the fitting parameters.

Even though the frequency resolution was implemented into the $\chi^2$, it is still favorable to have as many points on a track as computationally realistic. As discussed, this is time consuming computationally, but ensures more input parameter combinations and thereby a higher possibility for including a model with a good fit. The `varcontrol_target` command in `MESA` allowed for a somewhat better resolution (particularly for tracks with high $\alpha_{ov}$), but more options to increase the resolution even further should be considered in future work. This analysis was primarily focused on the evolutionary stage of the stars, but also depends strongly on the input parameters for the tracks. In this work, the step size of the tracks is bigger than that of Lenz et al. (2010), resulting in a larger difference in parameter space. Thus, models in between these tracks are not considered. Since creating an entire grid is time consuming, doubling it up would take very long, and could prove excessive particularly in those areas of the HRD where it would be less likely to find $\delta$ Sct pulsations. Instead, grid with smaller step sizes could be constructed around the tracks of either the best 5% models, or those with higher likelihood. The latter is, however, a different statistical approach where each model input parameter gives a likelihood. Both ways would also allow for a more detailed evaluation of the individual model parameters, particularly the $\alpha_{mlt}$ and $\alpha_o v$. By further constructing a narrow but dense grid around the best model, it can be tested if the minimal $\chi^2$ is still on the original track, or if $\chi^2$ can be optimized even further.

Throughout this project, the grid constructed was only calculated using GN93 element abundances and OPAL opacities. However, as Lenz et al. (2010) showed in asteroseismic modeling of 44 Tau, the tracks and thereby the evolutionary stage are affected by this choice. Therefore, a further analysis of the choice is needed in order to evaluate how it affects the $\chi^2$.

## 7.2 Stringent statistics

From a statistical point of view, the $\chi^2$ test carried out in this work is crudely simplified for the purpose of answering the question of which evolutionary stages the stars are in. The $\chi^2$ is merely a number that gives the sum of differences for the parameters, but a small $\chi^2$ does not necessarily mean that that model has the highest **likelihood**. In order to compare $\chi^2$ between all models in the grid, strictly speaking, the conditions should not change between the models as the individual parameters are then weighted differently. Therefore, since Eq. 6.4 adds a weight to the frequencies but not to the rest of the fitting parameters, the $\chi^2$ sum depends on two different weighting methods. This is not a problem in itself, but it is more statistically correct to ensure consistency. This means that comparing the same tracks for a different observed luminosity needs to be done very carefully since the uncertainties of the luminosities are different, and the $\chi^2$ are thereby automatically weighted differently. Strictly speaking, the two runs for 44 Tau (with different observation parameter sets) can not be compared since they do not have the same underlying conditions. But since the frequencies dominate the run, this is not an issue (as the frequency fit is the exact same in both cases).

In order to use the $\chi^2$ as a way of determining how well a **fit** the parameters provide, the reduced $\chi^2$ should be used instead. This is defined as

$$\chi^2_{red} = \frac{\chi^2}{K}, \tag{7.1}$$

where $K$ is the number of degrees of freedom. If the $\chi^2$ is larger than 1, the fit is considered "bad" in the sense that the value is high compared to degrees of freedom. However, if $\chi^2$ is smaller than one, it is considered an overfit. The reduced $\chi^2$ is commonly used in astronomy. However, determining the number of degrees is trivial at all. For linear models it is simply given by $N - P$, where $N$ is the number of datapoints and $P$ is the number of fit parameters. For the most this is works in practice. But it is strictly speaking not true since K can only be defined so if the basis functions are linearly independent in the sampled regime. Even though this is not the case for the modeling in this work, a reduced $\chi^2$ should be considered to make a more complete evaluation of the $\chi^2$ fits.

## 7.3 Non-adiabatic calculations

Implementing non-adiabatic calculations of the most relevant models should be considered for future work in order to get a full discription of the frequencies. This includes information of whether modes are excited or not, and a fuller picture of the excited frequency range. This is very useful for modeling since the range can be compared to the observed frequency range. Adiabatic calculations assume adiabadicity and solves purely linear equations. However, the non-adiabatic case is non-linear and therefore more complicated and time consuming. Making non-adiabatic solutions for every model in a grid would be excessive. Therefore, as mentioned earlier in this chapter, models should be initially evaluated to choose a set of models the calculations should be conducted on. First and foremost the pre-MS models should not be considered as there is no evidence to support that this is the evolutionary stage of 44 Tau and HD 187547. If the possibility is to be considered, the `MESA` tracks should be recalculated with the main purpose of optimizing them for stellar pulsations. Secondly, models outside the instability strip should not be included unless there is evidence that they are within reasonable fitting area. A way of doing so could be to calculate the adiabatic tracks and evaluate those (like here), and then additionally calculating the non-adiabatic values for the 5% or 10% best models.

# 8 Conclusion

The goal of this project was to use asteroseismic modeling on the two stars 44 Tau and HD 187547 respectively, in order to extract information on their frequencies, stellar parameters and evolutionary stages. For this purpose, a grid of models was calculated with `MESA` stellar structure and evolution code to simulate their evolutionary tracks. The `GYRE` pulsation code calculated theoretical frequencies for the entire grid to simulate the pulsations within the star. The resolution of the tracks were tested and improven to ensure that all stages of the evolution were properly resolved.

A $\chi^2$ method was implemented for both stars, in order to fit observed parameters to modeled parameters. The $\chi^2$ was implemented as defined by Eq. 6.1. The uncertainties of the frequencies were artificially enhanced through the resolution in a second $\chi^2$ implementation for 44 Tau. The purpose of this was to test if the frequencies needed to be weighed less to compensate for the small uncertainties. In both bases, 44 Tau was successfully modeled to be on the post-MS. For the classical $\chi^2$ approach, the best fitted model was on the tracks with mass $M = 1.55M_{\odot}$, $X = 0.65$, $Z = 0.01$, $\alpha_{mlt}$, $\alpha_{ov}$ and the minimum $\chi^2$ model was shown to be on the post-MS, well into the post-MS expansion phase. For the artificially enhanced case, the resulting best model was better fitted to the observational parameters $\log T_{\text{eff}}$,$\log L/L_{\odot}$ and $\log g$ with the evolutionary stage being slightly later. The results of the evolutionary stage agrees somewhat with the work from Lenz et al. (2010)(post-MS), although with a lower mass and at an even later stage. The fitted frequencies for the best models showed a discrepancy between $l$ from model and $l$ from mode identification, which is due to the fitting routine used to calculate the $\chi^2$ not taking $l$ into consideration. An additional result showed that the track with $M = 1.65M_{\odot}$, $X = 0.70$, $Z = 0.01$, $\alpha_{mlt} = 0.5$, $\alpha_{ov} = 0.3$ has a much better frequency fit (looking at the mode identification also) and an evolutionary stage on the Henyey hook, closer to the results from Lenz et al. (2010). However, the mass is underestimated compared to Lenz et al. (2010) and it is not clear whether this is due to inadequacy of the models (lack of time-dependent convection treatment and non-adiabatic calculations of the frequencies.), or a bias in the grid stemming from the low $\alpha_{mlt}$ values. Even though the frequency fit is significantly better, there is still two modes which differs from observations. This can possibly be explained with uncertainties in the model dependent mode identification. Further investigation is needed in order to address the difference between model parameters of this work and Lenz et al. (2010). The grid needs to be narrowed down in parameter space and have more grid points. This should be done around the best model, in order to test if the $\chi^2$ can be optimized more options for parameter combinations. The low values of $\alpha_{mlt}$ causes a bias in the models as the frequencies are strongly related to the models. Therefore, the grid needs to be tested with standard values around $\alpha_{mlt} = 1.8$ also.

For HD 187547 the modeling was conducted through fitting the theoretically calculated large frequency separation to two different observed estimates of $\Delta\nu$ (Antoci et al., 2011), (private communication,Victoria Antoci, Bedding et al. in review). The modeling was limited to $l = 0$ modes with a frequency range of $45 - 80d^{-1}$ since modeling the larger frequency separations for higher $l$ requires a more advanced routine than implemented here. This was done for $\Delta\nu = 3.5d^{-1}$ and $\Delta\nu = 7d^{-1}$ respectively. Results showed that for both $\Delta\nu$, the star is on the MS (although at a younger stage for the highest $\Delta\nu$). The $\Delta\nu = 3.5d^{-1}$ best track was outside the borders of the instability strip, and the best models $\chi^2$ for observed parameters and large frequency separation did not overlap. This strongly indicates that $\Delta\nu = 3.5d^{-1}$ is too low to account for the low value of $\log L/L_{\odot}$, and that the star is indeed at the earlier stages of the MS. A cutoff was made in the grid to exclude models on the pre-MS. Since it is an exact cutoff, the removal of MS models on some track was unavoidable. It is therefore a possibility that the star is even younger than modeled here. For future work, a cutoff should be made based on the helium content in the core, to find the MS on each individual track. Resolution is also poorest at the very early stages of the MS, and more tracks and models are needed to minimize the $\chi^2$ further. Additionally, the high order $l$ should be considered in the calculation of the separation. This could be done by cross-correlation between frequencies for selected model, as this would work for all values of $l$, and add more constraints to the modeling.

# Appendix

## 8.1 Inlist files from MESA and GYRE

### 8.1.1 MESA inlist

The standard inlist file used ofr `MESA` grid construction is shown here. The `initial_h1`,`initial_he3`,`initial_he4`, `mixing_length_alpha`, `new_mass` and the different `step_overshoot_f` commands changes the values of $X, Z, M, \alpha_{mlt}, \alpha_{ov}$ respectively. This is done through a bash script searching and replacing the correct values.

```
! For the sake of future readers of this file (yourself included),
! ONLY include the controls you are actually using.  DO NOT include
! all of the other controls that simply have their default values.

&star_job

  ! begin with a pre-main sequence model
  !  create_pre_main_sequence_model = .true.
    load_saved_model = .true.
    saved_model_name = 'pre_ms17.mod'

    set_uniform_initial_composition = .true.
    initial_zfracs = 2
    initial_h1 = 0.7
    initial_h2 = 0
    initial_he3 = 0.000028
    initial_he4 = 0.279972

    relax_initial_mass = .true.
    new_mass = 2.0
    lg_max_abs_mdot = -100

    kappa_file_prefix = 'gn93'
    kappa_lowT_prefix = 'lowT_fa05_gn93'

  ! save a model at the end of the run
  !  save_model_when_terminate = .true.
  !  save_model_filename = 'premain.mod'

  ! display on-screen plots
    pgstar_flag = .true.

/ !end of star_job namelist


&controls

  ! starting specifications
  !  initial_mass = 2.1
```

```

  ! stop when the star nears ZAMS (Lnuc/L > 0.99)
  !  Lnuc_div_L_zams_limit = 0.99d0
  !  stop_near_zams = .false.

  ! Stop when logg = 3.6848
  ! log_g_upper_limit = 3.6848

  ! stop when the center mass fraction of h1 drops below this limit
  !  xa_central_lower_limit_species(1) = 'h1'
  !  xa_central_lower_limit(1) = 1d-3

  ! Stop when Teff is smaller than this limit
  ! Teff_lower_limit = 7668
  ! log_L_upper_limit = 1.4
  ! My own initial parameters:

  !  initial_z = 0.027
  !  initial_y = 0.29

    mixing_length_alpha = 0.4
    step_overshoot_f_above_burn_h_core = 0.25
    overshoot_f0_above_burn_h_core = 0.01
    step_overshoot_f_above_burn_h_shell = 0.25
    overshoot_f0_above_burn_h_shell = 0.01
    step_overshoot_f_below_burn_h_shell = 0.25
    overshoot_f0_below_burn_h_shell = 0.01
    which_atm_option = 'Eddington_grey'

  ! Create model for GYRE to load

    write_pulse_data_with_profile = .true.
    pulse_data_format = 'GYRE'
    add_atmosphere_to_pulse_data = .true.

  !  write_gyre_for_best_model = .true.
  !  best_model_gyre_filenam = '44tau.mesa'
    log_directory = 'LOGS'
    history_interval = 1
    profile_interval = 1
    max_num_profile_models = 100000
    power_he_burn_upper_limit = 1d-20
    max_num_profile_zones = 2

  !  delta_lgTeff_limit = 0.0003
    varcontrol_target = 5d-5

/ ! end of controls namelist
```

### 8.1.2 GYRE input file to output

```
#!/bin/bash
```

```
#### converter for .GYRE file to oscillation mode frequencies with GYRE
#### Author: Earl Bellinger ( bellinger@phys.au.dk )
#### Stellar Astrophysics Centre, Aarhus
#### Updated: November 2018

### Parse command line tokens

HELP=0
EIGENF=0
SAVE=0
RADIAL=0
FGONG=0
OMP_NUM_THREADS=1
LOWER=0.01
UPPER=8496 # Kepler Nyquist frequency in microHertz
SCALE=0

### $# meaning the number of parameters passed to the script. So if you pass an argument you can choose between f
while [ "$#" -gt 0 ]; do
  case "$1" in
    -h) HELP=1; break;;
    -i) INPUT="$2"; shift 2;;
    -o) OUTPUT="$2"; shift 2;;
    -t) OMP_NUM_THREADS="$2"; shift 2;;
    -l) LOWER="$2"; shift 2;;
        -u) UPPER="$2"; shift 2;;
    -r) RADIAL=1; shift 1;;
    -e) EIGENF=1;SAVE=1; shift 1;;
    -f) FGONG=1; shift 1;;
    -s) SAVE=1; shift 1;;
    -S) SCALE=1; shift 1;;

    *) if [ -z "$INPUT" ]; then
           INPUT="$1"
           shift 1
         else
           echo "unknown option: $1" >&2
           exit 1
       fi;
  esac
done

if [ $HELP -gt 0 ] || [ -z "$INPUT" ]; then
    echo "Converter for .GYRE files to oscillation mode frequencies."
    echo "Usage: ./gyre2freqs.sh -i input -o output -t threads -e -r -l 1000"
    echo "Flags: -s : save calculations directory"
    echo "       -e : calculate eigenfunctions (automatically turns on -s)"
    echo "       -r : only calculate radial modes"
    echo "       -f : FGONG file format"
    echo "       -l : lower bound on frequency search"
    echo "       -S : use scaling relations to find lower bound"
```

```
    exit
fi

## Check that the first input (GYRE file) exists
if [ ! -e "$INPUT" ]; then
    echo "Error: Cannot locate GYRE file $INPUT"
    exit 1
fi

full_input_path="$(realpath $INPUT)"
## Pull out the name of the GYRE file
bname="$(basename $INPUT)"
fname="${bname%%.*}-freqs"
pname="${bname::-5}"

## If the OUTPUT argument doesn't exist, create a path from the filename
if [ -z ${OUTPUT+x} ]; then
    path=$(dirname "$INPUT")/"$fname"
  else
    path="$OUTPUT"
fi

MODES="
&mode
    l=0
/
&mode
    l=1
/
&mode
    l=2
/
"
if [ $RADIAL -gt 0 ]; then
    MODES="
&mode
    l=0
/
"
fi

if [ $FGONG -gt 0 ]; then
    FORMAT="'FGONG'
    data_format = '(1P5E16.9,x)'"
else
    FORMAT="'MESA'"
fi

MODE_ITEM_LIST=''
if [ $EIGENF -gt 0 ]; then
    MODE_ITEM_LIST="mode_file_format = 'TXT'
    mode_template = '%J-%L_%N'
    mode_item_list = 'M_star,R_star,l,n_pg,n_p,n_g,freq,E,E_p,E_g,E_norm,M_r,x,xi_r,xi_h'"
```

```
fi

# use the scaling relations to calculate lower frequency bound
if [ $SCALE -gt 0 ]; then
    #pnum=$(echo "$pname" | sed 's/profile//g')
    #profs<-read.table('../profiles.index', skip=1)
    #which[profs$V1==$pnum]

    # get the first line of the GYRE file
    read -r FIRSTLINE < "$INPUT"
    #LASTLINE=$(awk '/./{line=$0} END{print line}' "$INPUT")

    # pull out M, R, Teff from the GYRE file of the stellar model
    # https://bitbucket.org/rhdtownsend/gyre/src/tip/doc/mesa-format.pdf
    M=$(echo $FIRSTLINE | awk '{print $2}')
    R=$(echo $FIRSTLINE | awk '{print $3}')
    #T=$(echo $LASTLINE  | awk '{print $6}')

    # assumes that Teff is in the 7th column of the profile file header
    T=$(sed '3q;d' "${INPUT::-5}" | awk '{print $7}')

    # divide by the solar values
    Mscal=$(awk '{ print $1 / 1.988475E+33 }' <<< "$M")
    Rscal=$(awk '{ print $1 / 6.957E+10 }' <<< "$R")
    Tscal=$(awk '{ print $1 / 5772 }' <<< "$T")

    # calculate scaling relations
    # numax = M/R**2/sqrt(Teff/5777)
    # Dnu   = sqrt(M/R**3)
    numax=$(awk -v M="$Mscal" -v R="$Rscal" -v T="$Tscal" \
        'BEGIN { print M / R^2 * T^(-1/2) * 3090 }')
    Dnu=$(awk -v M="$Mscal" -v R="$Rscal" \
        'BEGIN { print (M / R^3)^(1/2) * 135 }')

    # find lower limit
    LOWER=$(awk -v numax="$numax" -v Dnu="$Dnu" \
        'BEGIN { print numax - 7.5*Dnu }')

        UPPER=$(awk -v numax="$numax" \
            'BEGIN { print numax * 5/3 }')

    # check that it's greater than 0.01 i
    if [ $(echo "$LOWER < 0.01" | bc -l) -gt 0 ]; then
        LOWER=0.01
    fi
fi

## Create a directory for the results and go there
mkdir -p "$path"
#cp "$INPUT" "$path"
cd "$path"

logfile="gyre-l0.log"
```

```
#exec > $logfile 2>&1

## Create a gyre.in file to find the large frequency separation
echo "&model
    model_type = 'EVOL'
    file = '$full_input_path'
    file_format = $FORMAT
/
&constants
!    G_GRAVITY = 6.67408d-8
!    M_SUN = 1.988475d33
!    R_SUN = 6.957d10
!    L_SUN = 3.828d33
/
$MODES
&osc
    outer_bound = 'JCD'
    variables_set = 'JCD'
    inertia_norm = 'BOTH'
    rotation_method = 'DOPPLER'
/
&num
    diff_scheme = 'MAGNUS_GL4'
/
&scan
    grid_type = 'LINEAR'
    freq_min_units = 'CYC_PER_DAY'
    freq_max_units = 'CYC_PER_DAY'
    freq_min = 0.1
    freq_max = 30
    n_freq = 200
/
&grid
    n_inner = 5
    alpha_osc = 10
    alpha_exp = 2
/
&ad_output
    summary_file = '$fname.dat'
    summary_file_format = 'TXT'
    summary_item_list = 'l,n_pg,n_p,n_g,freq,E_norm'
    freq_units = 'CYC_PER_DAY'
    $MODE_ITEM_LIST
/
&nad_output
/
" >| "gyre.in"

## Run GYRE
$GYRE_DIR/bin/gyre gyre.in &>gyre.out

### Hooray!
cp "$fname.dat" .. || exit 1
```

```
echo "Conversion complete. Results can be found in $fname.dat"
if [ $SAVE -gt 0 ]; then exit 0; fi
rm -rf *
currdir=$(pwd)
cd ..
rm -rf "$currdir"
exit 0
```

## 8.2 $\chi^2$ routine

For the purpose of calculating the $\chi^2$, multiple codes are used. Here, only some of them are presented. All files used in this project can be seen on the webpage `github`.

First, all profiles for all tracks located in the grid directory (`output_smallgrid`) are read into *call_chi.py* which is the main file. This calls several files (not listed here) to extract input parameters, observational properties and pulsations. A file with all the information is created for each track and put into a separate directory `Results_l0`[1].

```
#!/usr/bin/env python3
# -*- coding: utf-8 -*-
"""
Created on Mon Apr  8 14:30:32 2019

@author: janne

Call for all results
"""
import os
import matplotlib.pyplot as plt
import make_table_initparams as init
import make_table_fundfirst as fund
import calculate_chis_ff1 as chi
import numpy as np
plt.close('all')


allinfo = []
list_of_masses = []
list_of_zs = []
list_of_ys = []
list_of_mlts = []

def firstpart(dirname, mtracks):
    list_of_names = []
    list_of_minimums = []
    runonce = 0
    for root, dirs, files in sorted(os.walk(dirname)):
        dirs.sort(key=lambda x: '{0:0>20}'.format(x))
        for dire in dirs:
#            if runonce > 0:
```

[1]The "l0" indicates that the luminosity comes from the first dataset

```
#                   break

                #plt.figure(dire)
            directories = os.path.join(root,dire)
            allf = fund.getfundfreqs(directories)
            init.getinitparams(directories)
            print(directories)
            name = directories.lstrip(root)
            names = '/usr/users/jhm1496/stars/44_tau/44_tau/output_smallgrid/Results_l0/final_'+ name + '.t
            print(names)
            total_chi, minimum = chi.getchis(names)
            list_of_names += [names]
            list_of_minimums += [minimum]
            runonce +=1
            print(runonce)
            #print(list_of_names)
            fullnamelist = "namelist_" + mtracks + ".txt"
    np.savetxt(fullnamelist, list_of_names, delimiter=",", newline = "\n", fmt="%s")
    return  list_of_minimums, list_of_names

list_of_minimums, list_of_names = firstpart('/usr/users/jhm1496/stars/44_tau/44_tau/output_smallgrid/m215


"""

liste = []
for j in list_of_names:
    allinfo = []
    with open(j) as f:
        for line in f:
            inner = [elt.strip() for elt in line.split(',')]
            allinfo.append(inner)
            every = np.asarray(allinfo)
        liste.append(every)
        f.close()

        mass = allinfo[0][2]
        z    = allinfo[0][3]
        y    = allinfo[0][4]
        mlt  = allinfo[0][5]

        list_of_masses += [mass]
        list_of_zs     += [z]
        list_of_ys     += [y]
        list_of_mlts   += [mlt]

minima = np.asarray(list_of_minimums)
chi2 = minima[:,0]
redchi = minima[:,1]

plt.xlabel(r'Mass $[M_{\odot}]$')
plt.ylabel(r'$\chi^{2}$')
plt.rcParams.update({'font.size': 20})
```

```
plt.plot(list_of_masses, chi2,'.', MarkerSize = 15)
#plt.plot(list_of_zs, chi2,'.', MarkerSize = 15)

#def plotmass(input_name):
"""
```

This also does call an initially used $\chi^2$ code `calculate_chis_ff1.py` which was implemented wrong and resulted in $\chi_{freqs} = 1$. Therefore, the correct $\chi^2$ test used in this project is conducted in a separate file `call_chi_actually` that takes the output files in the `Results_l0` directory, calculates the $\chi^2$ based on the observational and pulsational values in the file and creates a new results file in `new_Results_l0`.

```
#!/usr/bin/env python3
# -*- coding: utf-8 -*-
"""
Created on Fri Apr  5 17:29:08 2019

@author: janne

#calculate chi2 for one directory
"""

import numpy as np
import os

radial_funda = 6.8980210
radial_first = 8.9606205

#The following uncertainties are incorrect! - Discuss with Vichi what to do
radial_funda_unc = 7.432077540*10**(-7) #3.682937895*10**(-5) #2.762223525*10**(-7)  # Where does the first
radial_first_unc = 2.243216851*10**(-6) #1.172368430*10**(-5) #8.454940424*10**(-7)  # same

Log_L_obs = 1.305
Log_Teff_obs = 3.839
Log_g_obs = 3.6
Log_Teff_obs_unc = 0.007
Log_L_obs_unc = 0.065
Log_g_obs_unc = 0.1


def getchis(filename, result_name):
    #filename = '/home/janne/Gunter_project/gunther_project/Results_l0/results.txt'

    final_list = []

    with open(filename) as f:
        for line in f:
            inner_list = [elt.strip() for elt in line.split(',')]
            pnum = float(inner_list[7])
            if pnum <= 900:
                continue
            final_list.append(inner_list)
```

```
    #print(len(final_list[0]))
    freqs_info = []

    for i in range(0,len(final_list)):
        #print(i)
        fund     = float(final_list[i][0])
        first    = float(final_list[i][1])
   #     mass     = float(final_list[i][2])
    #    z        = float(final_list[i][3])
    #    x        = float(final_list[i][4])
    #    mlt      = float(final_list[i][5])
   #     ov       = float(final_list[i][6])
        pnum     = float(final_list[i][7])
        teff     = float(final_list[i][8])
        g        = float(final_list[i][9])
        l        = float(final_list[i][10])
        age      = float(final_list[i][11])
   #    chi       = float(final_list[i][12])
   #    red_chi   = float(final_list[i][13])
   #    loglikely = float(final_list[i][14])

        assert pnum > 900
        ##### FIRST METHOD! ####################################
        if i > 0:
            delta_funda_j = np.abs(float(final_list[i][0])-float(final_list[i-1][0]))
            delta_first_j = np.abs(float(final_list[i][1])-float(final_list[i-1][1]))
        elif i == 0:
            delta_funda_j = np.abs(float(final_list[i][0])-float(final_list[i+1][0]))
            delta_first_j = np.abs(float(final_list[i][1])-float(final_list[i+1][1]))

        f_funda       = delta_funda_j/radial_funda_unc
        f_first       = delta_first_j/radial_first_unc

        alpha                  = 1#4.6
        chi_funda_pump         = (fund - radial_funda)**2/(radial_funda_unc**2*f_funda)
        chi_first_pump         = (first - radial_first)**2/(radial_first_unc**2*f_first)
        chi_allfreqs_pump      = 1/alpha*(chi_funda_pump + chi_first_pump)
        chi_funda              = ((fund-radial_funda)/radial_funda_unc)**2
        chi_first              = ((first-radial_first)/radial_first_unc)**2
        chi_allfreqs           = 1/alpha* (chi_funda + chi_first)
        chi_teff               = ((teff-Log_Teff_obs)/Log_Teff_obs_unc)**2
        chi_g                  = ((g-Log_g_obs)/Log_g_obs_unc)**2
        chi_l                  = ((l-Log_L_obs)/Log_L_obs_unc)**2


        chi_rest    = (chi_teff + chi_g + chi_l)
        restfreqs   = chi_rest/chi_allfreqs


        ##### SECOND METHOD! ###################################

#       # l = total number of different frequencies (=2 for l=0)
```

```
#           l = 2
#           sigma_j     = 1/l*np.sqrt((radial_funda-radial_funda_unc)**2+(radial_first-radial_first_unc)**2)
#           chi_allfreqs_m2 = (radial_funda-radial_funda_unc/sigma_j)**2+(radial_first-radial_first_unc/sigma_j)**2

        freqs_info += [[restfreqs, chi_rest, chi_allfreqs, chi_allfreqs_pump, f_funda, f_first]]


#           #chi         = (chi_rest + chi_allfreqs)

#           #diff        = np.abs(chi_rest-chi_allfreqs)


#           likelihood = math.exp(0.5*(-chi**2)) #* age1  #if problems, consider log(weights) NOT Log10
#           loglikely = np.log(age1) - 0.5*chi**2

 #          N = 5#len(final_list)
 #          P = 0#5
 #          K = N-P
 #          red_chi    = chi/K
 #          total_chi += [[chi, red_chi, loglikely]]
 #          minimum = min(total_chi)

    freqs_forchi  = np.asarray(freqs_info)

    add_list = np.asarray(freqs_forchi[:,0])
    rest_list = np.asarray(freqs_forchi[:,1])
    allfreqs_list = np.asarray(freqs_forchi[:,2])
    allfreqs_pumped_list = np.asarray(freqs_forchi[:,3])
    funct_fundas  = np.asarray(freqs_forchi[:,4])
    funct_firsts  = np.asarray(freqs_forchi[:,5])
#    freqs_m2       = np.asarray(freqs_forchi[:,6])

    add_factor = np.sum(add_list)/len(add_list)
    print(add_factor)
    #new_chi_freqs = allfreqs_list       #*add_factor. This add factor is in case we wish to weigh the frequencies by the ra

    chi_final_pumped = allfreqs_pumped_list + rest_list
    chi_final        = allfreqs_list + rest_list

    #print(ages.index(maxagestep))
    output_chi = np.column_stack((funct_fundas, funct_firsts, allfreqs_list, allfreqs_pumped_list, chi_final, chi_final_pumped
    output_final = np.column_stack((final_list, output_chi))
    np.savetxt(result_name, output_final, delimiter=",", newline = "\n", fmt="%s")

    return output_final

for root, dirs, files in sorted(os.walk('/usr/users/jhm1496/stars/44_tau/44_tau/output_smallgrid/Results_l0')):

    for file in files:
        if file.startswith('final_'):
            dirs = os.path.join(root,file)
            print(dirs)
            maindir = '/usr/users/jhm1496/stars/44_tau/44_tau/output_smallgrid/new_Results_l0/'
```

```
            output_filename = maindir + '/' + os.path.join(file)
            output_final = getchis(dirs,output_filename)
```

The output files created contains all $\chi^2$ information $\chi^2_{tot}$,$\chi^2_{freqs}$, $\chi^2_{obs}$ and the artificially pumped total $\chi^2$ and frequencies$\chi^2_{tot,enhanced}$,$\chi^2_{freqs,enhanced}$. For each file (containing information for an entire track) the lowest $\chi^2_{tot}$ is found. Among these, the best 5% models are found. These selections happens in `plot_chis_actually.py`:

```
#/usr/bin/env python3
# -*- coding: utf-8 -*-
"""
Created on Thu May  9 12:00:20 2019

@author: janne
"""
import numpy as np
import os
import matplotlib.pyplot as plt

plt.close("all")
Log_L_obs = 1.305
Log_Teff_obs = 3.839
Log_g_obs = 3.6
Log_Teff_obs_unc = 0.007
Log_L_obs_unc = 0.065
Log_g_obs_unc = 0.1
#final_list = []
minimums      = []

list_of_files  = []
list_of_masses = []
list_of_zs     = []
list_of_ys     = []
list_of_mlts   = []
list_of_ovs    = []
list_of_pnums  = []
#filename = '/home/janne/Gunter_project/gunther_project/Results_l0/final_LOGS-1.75-0.03-0.75-0.2-0.
def getminimum(filename):
    final_list = []
    inner_list = []
    with open(filename) as f:
        for line in f:
            inner_list = [elt.strip() for elt in line.split(',')]
            final_list.append(inner_list)
    #print(filename)
    chis      = []
    best_pnums = []
    teffs     = []
    ls        = []
    gs        = []

    for i in range(0,len(final_list)):
```

```
            #fund      = float(final_list[i][0])
            #first     = float(final_list[i][1])
            pnum       = float(final_list[i][7])
            #print(pnum)
            teff       = float(final_list[i][8])
            g          = float(final_list[i][9])
            l          = float(final_list[i][10])
            #age       = float(final_list[i][11])
            mass       = float(final_list[0][2])
            z          = float(final_list[0][3])
            y          = float(final_list[0][4])
            mlt        = float(final_list[0][5])
            ov         = float(final_list[0][6])
            chi        = float(final_list[i][19])

            chis           += [chi]
            best_pnums     += [pnum]
            teffs          += [teff]
            ls             += [l]
            gs             += [g]

        a = np.asarray(chis)
        b = np.asarray(best_pnums)

        minimum = min(a)

        #print(a,minimum)
        pnum_index = np.where(a==minimum)
        #print(pnum_index)
        #print(best_pnums)
        #print(best_pnums)
        pnum_best = b[pnum_index]

        return minimum, mass, z, y, mlt, ov, pnum_best
profile_structure = []
list_of_minimums = []
for root, dirs, files in sorted(os.walk('/usr/users/jhm1496/stars/44_tau/44_tau/output_smallgrid/new_Results_l0')):
        dirs.sort(key=lambda x: '{0:0>20}'.format(x))
        for file in files:
            if file.startswith("final_"):
                filedir = os.path.join(root,file)
                #print(filedir)
                minimum, mass, z, y, mlt, ov, pnum = getminimum(filedir)
                list_of_files     += [filedir]


                list_of_pnums     += [pnum]
                list_of_minimums += [minimum]
                list_of_masses    += [mass]
                list_of_zs        += [z]
                list_of_ys        += [y]
                list_of_mlts      += [mlt]
                list_of_ovs       += [ov]
```

```
                profile_structure += ['LOGS-'+ str(format(mass, '.2f')) + '-'+ str(z) + '-' + str(y) + '-'
                                      + str(mlt) +'-'+ str(ov) + '-'+ 'profile' +str(int(pnum)) +'.data']

                decent = np.asarray([list_of_minimums, list_of_files, list_of_pnums, list_of_masses,
                                     list_of_zs, list_of_ys, list_of_mlts, profile_structure])
                #print(decent)
#print(list_of_pnums)
fivep_index = np.argsort(decent[0,:].astype('float'))
sorted_min  = np.asarray(decent[:,[fivep_index]])
#print(sorted_min)
percentage = 0.05

fivep = sorted_min[:,:,0:int(percentage*len(list_of_minimums))]
final = np.concatenate(fivep)

fig = plt.figure()
ax = plt.gca()

plt.plot(list_of_masses, list_of_minimums,'k.', MarkerSize = 15)
plt.plot(final[3,:].astype('float'), final[0,:].astype('float'), 'r.',fillstyle='none', MarkerSize = 15,markeredgewidth
plt.xticks(np.arange(min(list_of_masses)-0.05, max(list_of_masses)+0.05, step=0.02))
ax.tick_params(labelsize = 20)
#print(min(list_of_masses), max(list_of_masses))
Mlabel = r'$M/M_{\odot}$'
Mltlabel = r'$\alpha_{mlt}$'
Zlabel = r'$Z$'
Ylabel = r'$Y$'
OVlabel = r'$\alpha_{ov}$'
plt.xlabel(Mlabel,fontsize=20)
plt.ylabel(r'$\chi^{2}$', fontsize=20)
limit = (5/100)*max(list_of_minimums) + min(list_of_minimums)
plt.xticks(np.arange(1.45, 2.25, step=0.05))
#print(final)
firstpoint = np.float(final[0,-1])
secondpoint = np.float(sorted_min[0][0][len(final[0])])
mean = np.mean([firstpoint, secondpoint])

plt.plot([1.49,max(list_of_masses)+0.01],[mean,mean],'r--', linewidth = 3.50)
final_needed = []
files3 = []
for k in range(0,len(final[1])):
    y = 0
    directories = final[1][k]
    files  = directories.lstrip('/usr/users/jhm1496/stars/44_tau/44_tau/output_smallgrid/new_Results_l0/')
    pnumber = str(int(float(final[2][k])))
    pnums = 'profile' + pnumber + '.data'
    files2 = files.rstrip('.txt')
    files3 += [files2 + '-profile' + str(final[2,y])]
    y += 1
    final_needed += [[files, pnums ]]

np.savetxt('/usr/users/jhm1496/stars/44_tau/44_tau/output_smallgrid/new_Results_l0/bestfivep.txt', final_ne
```

```
    #best_files = [files2]
#allinfonames = files2
#plt.plot(list_of_masses[indx], list_of_minimums[indx], 'r.', MarkerSize = 25 )

## find top 5% models based on Teff, L, and Logg.

plt.show()
```

This will create an ouput file with the names of the 5% best models, as listed in Table 6.2. It also produces a plot with the best $\chi^2$ model for each track plotted as a function of mass. An example plot can be seen on Fig. 8.1.

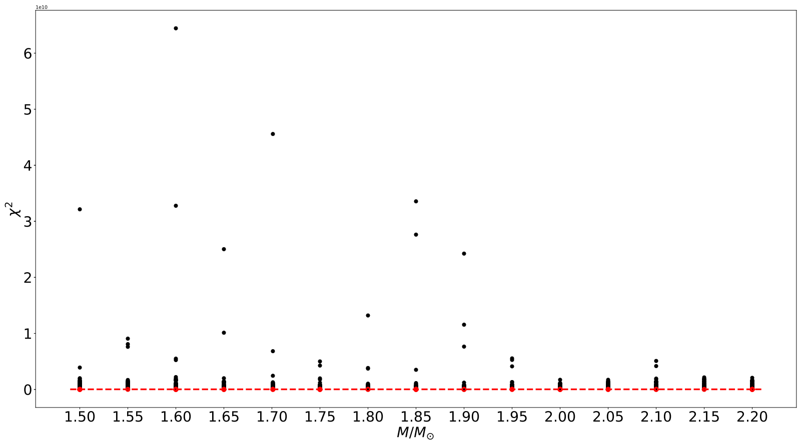


Figure 8.1: Lowest $\chi^2$ models for each track plotted as a function of mass. The red lines indicates the 5% lower $\chi^2$ limit for models to be included into the best 5%.

The non-radial pulsations are then calculated in `GYRE` for the 5% best models. From these, the $\chi^2$ routine for $l = 0, 1, 2$ is run to obtain new $\chi^2$. This is done in `getl1l2_results_actually_version2.py`

```

"""
Created on Wed Apr 10 11:25:35 2019

@author: janne
"""
import gyre_output_read as gar
import numpy as np
import mesa_reader as mr
import os

Log_L_obs = 1.305
Log_Teff_obs = 3.839
Log_g_obs = 3.6
```

```
Log_Teff_obs_unc = 0.007
Log_L_obs_unc = 0.065
Log_g_obs_unc = 0.1

final_list = []
#files_tofindchi = []
mean_functs = []
kolonner_m1 = []
kolonner_m2 = []
alphas = []
chis_final_pumped = []
chis_final = []
chis_rests = []
chis_freqs_pumped = []
chis_freqs = []
#final_list2 = []

filename = '/usr/users/jhm1496/stars/44_tau/44_tau/output_smallgrid/new_Results_l0/bestfivep.txt' #lum1
with open(filename) as f:
    for line in f:
        inner_list = [elt.strip() for elt in line.split(',')]
        final_list.append(inner_list)
#print(final_list)
array = np.asarray(final_list)
logfiles = array[:,0]
profile = array[:,1]
print(logfiles, profile)
for k in range(0,len(logfiles)):
    final_list2 = []
    logdir = logfiles[k].lstrip('final_')
    logdir2 = logdir.rstrip('.txt')
    pnum1 = profile[k].lstrip('profile')
    pnum2 = pnum1.rstrip('.data')
    logs_profiledir = logdir2 + '/' + profile[k]
    maindir = '/usr/users/jhm1496/stars/python_scripts/bestfive_dirs'
    direc = maindir + '/' + logdir2 + '/profile' + pnum2 + '-freqs.dat' # Directory with l=1 and l=2 mode
    print(direc)

#    final_list2 = []
    finalarray = []
    bm_array2 = []
    #dires = os.path.join(root,file)
    data = gar.readmesa(direc)
    harm_degree = data['l']
    radial_order= data['n_pg']

    re_freq_theo = data['Refreq'] # these are the frequencies that will be compared to Lenz and observations.
    #im_freq = data['Imfreq'] #imaginary part of frequencies are not observable.
    #print(re_freq_theo)

    re_freq_obs = [ 6.8980209, 7.00599425, 9.11743254, 11.5196319, 8.96062045, 8.96062045, 7.30312483, 6.
   # re_freq_obs_unc      = listofzeros = [10**(-7)] * len(re_freq_obs)#np.ones(len(re_freq_obs))*10**(-7)
    re_freq_obs_unc = [7.432077540*10**(-7), 2.010925863*10**(-6), 2.363621297*10**(-6), 1.999560327
```

```
    #print(len(np.atleast_1d(re_freq_theo)))
    #re_freq_obs_unc = np.ones(len(re_freq_obs)) * 0.1
    remaining_obs = re_freq_obs
    remaining_obs_unc = re_freq_obs_unc
    remaining_theo = np.atleast_1d(re_freq_theo)
    remaining_ells = np.atleast_1d(harm_degree)
    remaining_radial = np.atleast_1d(radial_order)

    best_matching = []
    #names = []

    for ii in range(min(len(np.atleast_1d(re_freq_theo)), len(re_freq_obs))): #default: freq_obs, but depends if freq_obs is l
        best = np.inf
        bestjj = -1
        bestkk = -1

        #print(len(remaining_obs))

        for jj in range(len(np.atleast_1d(remaining_theo))):
            for kk in range(len(remaining_obs)):
                val = (remaining_theo[jj] - remaining_obs[kk])**2 / 4 #put uncertainty here
                if (val < best):
                    best = val
                    bestjj = jj
                    bestkk = kk

                    # print(best, bestjj, bestkk)
        best_matching += [[remaining_ells[bestjj], remaining_radial[bestjj], remaining_theo[bestjj], remaining_obs[bestkk], r

        remaining_theo = np.delete(remaining_theo, bestjj)
        remaining_ells = np.delete(remaining_ells, bestjj)
        remaining_obs = np.delete(remaining_obs, bestkk)
        remaining_obs_unc = np.delete(remaining_obs_unc, bestkk)
        remaining_radial = np.delete(remaining_radial,bestjj)

        #diff = np.asarray(diff)
        #final = np.append(bm_array,diff)

    bm_array = np.asarray(best_matching)
    bm_array2 += [bm_array]
    finalarray += [[bm_array, pnum2]]
    print(finalarray)

    #### FIRST METHOD ###############################################
#     final_list2 = []
    filename2 = '/usr/users/jhm1496/stars/44_tau/44_tau/output_smallgrid/new_Results_l0/final_' + logdir2 + '.txt'
    with open(filename2) as f2:
        for line2 in f2:
            inner_list2 = [elt.strip() for elt in line2.split(',')]
            final_list2.append(inner_list2)

    for i in range(0,len(final_list2)):
        profilenumber = float(final_list2[i][7])
```

```
        #print(profilenumber, pnum2)
        if int(profilenumber) == int(float(pnum2)):
            teff        = float(final_list2[i][8])
            logg        = float(final_list2[i][9])
            logl        = float(final_list2[i][10])
            funct_funda = float(final_list2[i][15])
            funct_first = float(final_list2[i][16])
            mean = (funct_funda + funct_first)/2

            chi_teff  = ((teff-Log_Teff_obs)/Log_Teff_obs_unc)**2
            chi_g     = ((logg-Log_g_obs)/Log_g_obs_unc)**2
            chi_l     = ((logl-Log_L_obs)/Log_L_obs_unc)**2
            chi_rest  = chi_teff + chi_g + chi_l
            #chis_rests += [chi_rest]
            mean_functs += [mean]

            chi2sum_pump = {}
            chi2sum = {}
            chi2sigma = {}
            chi2m2 = {}
            chiforalpha = {}
            chi2m1 = {}
            #print(finalarray)

            for ii in range(len(finalarray)):
                for kk in range(len(finalarray[ii][0])):
                    pname = finalarray[ii][1]
                    if pname not in chi2sum.keys():
                        chi2sum_pump[pname] = 0
                        chi2sum[pname] = 0
                        chi2sigma[pname] = 0
                        chi2m2[pname] = 0

                    chi2sum_pump[pname] = (chi2sum[pname] + (finalarray[ii][0][kk][2] - finalarray[ii][0][kk][3])*
                    chi2sum[pname] = (chi2sum[pname] + (finalarray[ii][0][kk][2] - finalarray[ii][0][kk][3])**2/(fin
                    chi2sigma[pname] = chi2sigma[pname] + (finalarray[ii][0][kk][2] - finalarray[ii][0][kk][3])**2

            # for ii in range(len(finalarray)):
            #     pname = finalarray[ii][1]
            #     sigma_value = 1/len(finalarray[ii][0])*np.sqrt(chi2sigma[pname])

            #     for kk in range(len(finalarray[ii][0])):
            #         chi2m2[pname] = chi2m2[pname] + ((finalarray[ii][0][kk][2] - finalarray[ii][0][kk][3])/sigma_
            #         print(chi2m2,kk)

            m1 = chi2sum_pump.values()
            m2 = chi2sum.values()

            #for g in m1:
            #    alpha_m1 = chi_rest/g
            #    alphas += [alpha_m1]

            #    alphas_to = np.asarray(alphas)
```

```
            #    final_alpha = 1#np.sum(alphas_to)/len(alphas_to)

            final_alpha = 1

            for n in m1:
                allfreqs_pumped = final_alpha * n
                chi_m1 = allfreqs_pumped + chi_rest
                chis_freqs_pumped += [allfreqs_pumped]
                chis_final_pumped += [chi_m1]
            for m in m2:
                allfreqs = m
                chi_m2 = m + chi_rest
                chis_freqs += [allfreqs]
                chis_final += [chi_m2]
                chis_rests += [chi_rest]
            #chis_freqs += [allfreqs]
            #chis_freqs_pumped += [allfreqs_pumped]
            #chis_final_pumped += [chi_m1]
            #chis_final+= [chi_m2]
            #chis_rests += [chi_rest]
            #kolonner_m1 += [list(m1)]
            #kolonner_m2 += [list(m2)]

#print(len(final_list))
#print(len(chis_rests))
#print(len(chis_final))
#print(len(chis_final_pumped))
print(chis_final[0], chis_freqs[0], chis_rests[0])

output = np.column_stack((final_list, chis_rests, chis_freqs, chis_freqs_pumped, chis_final, chis_final_pumped))
savedir = '/usr/users/jhm1496/stars/44_tau/44_tau/output_smallgrid/Results_l012/' + 'final_fivep.txt'
np.savetxt(savedir, output, delimiter=",", newline = "\n", fmt="%s")


#finalarray, kolonne = to_get_chi2('/home/janne/Gunter_project/44_tau/new_chi_method/Results/')
```

,
which produces the final output file. This file is then opened in `test_l012_results_actually_version2.py`.

```
import os
import numpy as np

dire = '/usr/users/jhm1496/stars/44_tau/44_tau/output_smallgrid/Results_l012'

for root, dirs, files in sorted(os.walk(dire)):
    files.sort(key=lambda x: '{0:0>20}'.format(x))
    for file in files:
        if file.startswith('final_fivep.txt'):
            finals = []
            directory = os.path.join(root,file)
            filename = directory
            final_list = []
            with open(filename) as f:
                for line in f:
```

```
            inner_list = [elt.strip() for elt in line.split(',')]
            final_list.append(inner_list)
        #print(final_list)
        finals += [final_list]
        #for i in range(0,len(finals)):
        #   chi2_freqs = final_list[i][9]

        final = np.concatenate(finals)
        #print(np.shape(final))
        chi2_params = final[:,2].astype('float')
        chi2_freqs = final[:,3].astype('float')
        chi2_freqs_pumped = final[:,4].astype('float')
        chi2_tot = final[:,5]
        chi2_tot_pumped = final[:,6]

#           print(chi2_tot[0], chi2_tot_pumped[0])
        #print(chi2_param)
        minimum_freqs = min(chi2_freqs.astype('float'))
        minimum_freqs_pumped = min(chi2_freqs_pumped.astype('float'))
        minimum_chi_tot = min(chi2_tot.astype('float'))
        minimum_chi_tot_pumped = min(chi2_tot_pumped.astype('float'))
        minimum_param = min(chi2_params.astype('float'))
        print(minimum_chi_tot_pumped)

        index_minfreqs = np.where(chi2_freqs.astype('float') == minimum_freqs)
        index_minfreqs_pumped = np.where(chi2_freqs_pumped.astype('float') == minimum_freqs_pumped)
        index_minchi = np.where(chi2_tot.astype('float') == minimum_chi_tot)
        index_minchi_pumped = np.where(chi2_tot_pumped.astype('float') == minimum_chi_tot_pumped)
        index_minparam = np.where(chi2_params.astype('float') == minimum_param)

#print(chi2_tot, minimum_chi_tot)
print(final[index_minchi,:], minimum_chi_tot)
print(final[index_minfreqs,:], minimum_freqs)
print(final[index_minparam,:], minimum_param)
print(final[index_minchi_pumped,:], minimum_chi_tot_pumped)
```

,

The output prints the minimum $\chi^2_{tot}$, $\chi^2_{obs}$, $\chi^2_{freqs}$ and $\chi^2_p$ (enhanced total $\chi^2$). All of these routines are for 44 Tau calculations. The routines for HD 187547 are similar, but with different directories. The $\chi^2$ code also implements a routine for calculating the separation. This is done in `calculate_chis_ff1_superstar_withcorrectsep.py` called in the main file which is similar to the main file for 44 Tau, and is therefore not listed here).

```
#!/usr/bin/env python3
# -*- coding: utf-8 -*-
"""
Created on Tue Jun 25 21:45:41 2019

@author: janne
"""


#!/usr/bin/env python3
```

```
# -*- coding: utf-8 -*-
"""
Created on Fri Apr  5 17:29:08 2019

@author: janne

#calculate chi2 for one directory
"""

import numpy as np
import os
import re
import gyre_output_read as gar
radial_funda = 6.8980
radial_first = 8.9606

#The following uncertainties are incorrect! - Discuss with Vichi what to do
#radial_funda_unc = 3.682937895*10**(-5) #2.762223525*10**(-7)
#radial_first_unc = 1.172368430*10**(-5) #8.454940424*10**(-7)

Log_L_obs = 0.859073 # GAIA 0.8372440 self-calculated
Log_Teff_obs = 3.87506
Log_g_obs = 3.9
Log_Teff_obs_unc = 0.01158
Log_L_obs_unc = 0.00328 # GAIA
Log_g_obs_unc = 0.2
sepa_obs = 3.5 #cyc/day
sepa_obs_unc = 0.05
#seps = []

def getmeansep(fname):
    fnumbers = []
    alle = []
    finalone = []
    for root, dirs, files in sorted(os.walk(fname)):
            #files.sort(key=lambda x: int(os.path.splitext(x)[0]))
            for file in files:

                if not file.endswith('freqs.dat'):
                    continue
#                print(file)

                fdires = os.path.join(root,file)
                fdata = gar.readmesa(fdires)
#                 #print(fdires)

                if np.size(fdata) == 1:
                    continue

                fnum = re.search('profile(.+?)-freqs.dat', fdires)

                if fnum:
                    fnums = fnum.group(1)
```

```
                    fnum2 = int(fnums)
                    #print(fnum2)
#                  if not fnum2 > 900:
#                      continue
                allf = []
                for i in range(0,len(fdata)):
                    if i < len(fdata) -1:
                        separation = np.abs(fdata[i+1][4]-fdata[i][4])

                    else:
                        separation = np.abs(fdata[i-1][4]-fdata[i][4])


                    allf += [separation]
                #rint(separation)
                #The following way of determining mean applies only well to l=0 modes!

                meansep = np.mean(allf)
                finalone += [[meansep, fnum2]]
                finalonearray = np.asarray(finalone)
                finalonearray = finalonearray[finalonearray[:,1].argsort()]
    #print(finalonearray)
    return finalonearray



def getchis(filename,result_name):
#    filename = '/usr/users/jhm1496/stars/44_tau/44_tau/output_smallgrid_superstar/Results_l0/results.txt'

    final_list = []
    total_chi = []
    red_chi = []
    with open(filename) as f:
        for line in f:
            inner_list = [elt.strip() for elt in line.split(',')]
            final_list.append(inner_list)

    sepa_info = []
    f_sepas = []
    seps = []
    pnums = []
    print(filename)
    hoveddir = '/usr/users/jhm1496/stars/44_tau/44_tau/output_smallgrid_superstar/'
    logdir = hoveddir + filename.strip('/usr/users/jhm1496/stars/44_tau/44_tau/output_smallgrid_superstar/F
    #print(logdir)
    finalforsep = getmeansep(logdir)
    print(np.shape(finalforsep), len(finalforsep))
    #print(finalforsep[0][0])
    sepaarray = np.asarray(finalforsep)
    for i in range(0,len(final_list)):

        pnum     = float(final_list[i][6])
        print(pnum, finalforsep[i][1])
```

```
        sepa      = float(finalforsep[i][0])
        teff      = float(final_list[i][7])
        g         = float(final_list[i][8])
        l         = float(final_list[i][9])
        age       = float(final_list[i][10])
        seps     += [sepa]
        pnums    += [pnum]
        ########## METHOD 1 ########################################

        if not int(pnum) > 900:
            continue

        if i>0:
            delta_sep = np.abs(float(final_list[i][0])-float(final_list[i-1][0]))
        elif i==0:
            delta_sep = np.abs(float(final_list[i][0])-float(final_list[i+1][0]))

        f_sep = delta_sep/sepa_obs_unc

        alpha = 1
        chi_sep            = (np.abs(sepa - sepa_obs)/sepa_obs_unc)**2   #*f_sep)
        chi_sep_pumped     = (sepa - sepa_obs)**2/(sepa_obs_unc**2*f_sep)
        chi_allsep         = 1/alpha*chi_sep
        chi_teff           = ((teff-Log_Teff_obs)/Log_Teff_obs_unc)**2
        chi_g              = ((g-Log_g_obs)/Log_g_obs_unc)**2
        chi_l              = ((l-Log_L_obs)/Log_L_obs_unc)**2

        chi_rest   = (chi_teff + chi_g + chi_l) # + chi_sep)
        ratio      = chi_rest/chi_allsep
        #print(chi_allsep, chi_rest)
#          chi_final          = chi_sep + chi_rest

        sepa_info += [[ratio, f_sep, chi_rest, chi_sep, chi_sep_pumped, chi_l, sepa]]
    index_forfinal = np.where(np.asarray(pnums) > 900)
    index_forfinal2 = np.asarray(index_forfinal)
    finallist_array = np.asarray(final_list)
    sepa_info_array = np.asarray(sepa_info)

    ratios         = np.asarray(sepa_info_array[:,0])
    functs         = np.asarray(sepa_info_array[:,1])
    rests          = np.asarray(sepa_info_array[:,2])
    allseps        = np.asarray(sepa_info_array[:,3])
    allseps_pumped = np.asarray(sepa_info_array[:,4])
    ls             = np.asarray(sepa_info_array[:,5])
    just_seps      = np.asarray(sepa_info_array[:,6])

    add_factor = np.sum(ratios)/len(ratios)
    #print(add_factor)
    new_chi_sepa = allseps #*(add_factor)
    final_chi     = new_chi_sepa + rests
    final_chi_pumped = allseps_pumped + rests
#   print(type(final_list),np.shape(final_list), type(index_forfinal2), np.shape(index_forfinal2))
    output_chi = np.column_stack((ratios, functs, rests, allseps, allseps_pumped, ls,  final_chi, final_chi_pumped, just_seps
```

```
    #print(len(finallist_array[index_forfinal[0],:]), len(output_chi), len(index_forfinal[0]))
    output_final = np.column_stack((finallist_array[index_forfinal2[0],:], output_chi))
    #print(rests[0], allseps[0], final_chi[0], just_seps[0])
    np.savetxt(result_name, output_final, delimiter=",", newline = "\n", fmt="%s")

    return output_final

for root, dirs, files in sorted(os.walk('/usr/users/jhm1496/stars/44_tau/44_tau/output_smallgrid_superstar/Res
    for file in files:
        if file.startswith('final'):
            dirs = os.path.join(root,file)
            maindir = '/usr/users/jhm1496/stars/44_tau/44_tau/output_smallgrid_superstar/new_Results_l0'
            #logdir = maindir.rstrip('new_Results_l0') + dirs.lstrip(maindir).strip('_final-').rstrip('.txt')
            output_filename = maindir + '/' + os.path.join(file)
            output_final = getchis(dirs,output_filename)
```

.

# Bibliography


Aerts, Conny, Jørgen Christensen-Dalsgaard, & Donald W Kurtz (2010). *Asteroseismology.* Springer Science & Business Media.

Andrae, René et al. (2018). "Gaia Data Release 2-First stellar parameters from Apsis". In: *Astronomy & Astrophysics* 616, A8.

Antoci, V et al. (2011). "The excitation of solar-like oscillations in a $\delta$ Sct star by efficient envelope convection". In: *Nature* 477.7366, p. 570.

Antoci, Victoria Laura (2011). "Solar-like oscillations in Delta Scuti stars". PhD thesis. uniwien.

Antoci, V et al. (2007). "Is 44 Tauri an exceptional case among the $\delta$ Scuti stars?" In: *Astronomy & Astrophysics* 463.1, pp. 225–232.

Antoci, V et al. (2014). "The role of turbulent pressure as a coherent pulsational driving mechanism: The case of the $\delta$ Scuti star HD 187547". In: *The Astrophysical Journal* 796.2, p. 118.

Asplund, Martin et al. (2009). "The chemical composition of the Sun". In: *Annual review of astronomy and astrophysics* 47, pp. 481–522.

Badnell, Nigel R et al. (2005). "Updated opacities from the Opacity Project". In: *Monthly Notices of the Royal Astronomical Society* 360.2, pp. 458–464.

Balona, LA et al. (2011). "Kepler observations of Am stars". In: *Monthly Notices of the Royal Astronomical Society* 414.1, pp. 792–800.

Borucki, W, D Koch, N Batalha, et al. (2009). *Transiting Planets (IAU Symp. 253), ed.*

Breger, M. & P. Lenz (Sept. 2008). "Amplitude variability and multiple frequencies in 44 Tauri: 2000-2006". In: *Astronomy & Astrophysics* 488, pp. 643–651. arXiv: `0807.3219`.

Brown, AGA et al. (2018). "Gaia Data Release 2-Summary of the contents and survey properties". In: *Astronomy & astrophysics* 616, A1.

Cassisi, Santi et al. (2007). "Updated electron-conduction opacities: the impact on low-mass stellar models". In: *The Astrophysical Journal* 661.2, p. 1094.

Christensen-Dalsgaard, J (1984). "What will asteroseismology teach us". In: *Space Research in Stellar Activity and Variability*, p. 11.

Christensen-Dalsgaard, Jørgen (2008a). "ADIPLS—the Aarhus adiabatic oscillation package". In: *Astrophysics and Space Science* 316.1-4, pp. 113–120.

— (2008b). *Lecture notes on stellar structure and evolution.* Aarhus Universitet. Institute for Fysik og Astronomi.

Cody, Ann Marie & Lynne A Hillenbrand (2014). “A pulsation search among young brown dwarfs and very-low-mass stars”. In: *The Astrophysical Journal* 796.2, p. 129.

Dupret, M-A et al. (2004). “Theoretical instability strips for $\delta$ Scuti and $\gamma$ Doradus stars”. In: *Astronomy & Astrophysics* 414.2, pp. L17–L20.

Dupret, M-A et al. (2005). “Time-dependent convection seismic study of $\delta$ Sct stars”. In: *Monthly Notices of the Royal Astronomical Society* 361.2, pp. 476–486.

Dziembowski, W & M Królikowska (1990). “On the mechanism of mode selection in Delta Scuti stars”. In: *Acta Astronomica* 40, pp. 19–26.

Eggleton, Peter P (1971). “The evolution of low mass stars”. In: *Monthly Notices of the Royal Astronomical Society* 151.3, pp. 351–364.

Ferguson, Jason W et al. (2005). “Low-temperature opacities”. In: *The Astrophysical Journal* 623.1, p. 585.

Flower, P. J. (Sept. 1996). “Transformations from Theoretical Hertzsprung-Russell Diagrams to Color-Magnitude Diagrams: Effective Temperatures, B-V Colors, and Bolometric Corrections”. In: *The Astrophysical Journal* 469, p. 355.

Freedman, Richard S, Mark S Marley, & Katharina Lodders (2008). “Line and mean opacities for ultracool dwarfs and extrasolar planets”. In: *The Astrophysical Journal Supplement Series* 174.2, p. 504.

Gehmeyr, M & D Mihalas (1994). “Adaptive grid radiation hydrodynamics with TITAN”. In: *Physica D: Nonlinear Phenomena* 77.1-3, pp. 320–341.

Gilliland, Ronald L et al. (2010). “Kepler asteroseismology program: introduction and first results”. In: *Publications of the Astronomical Society of the Pacific* 122.888, p. 131.

Gough, DO (1996). “Astereoasteroseismology”. In: *The Observatory* 116, pp. 313–315.

Grevesse, N & A Noels (1993). “Cosmic abundances of the elements.” In: *Origin and Evolution of the Elements*, pp. 15–25.

Grevesse, N & AJ Sauval (1998). “Standard solar composition”. In: *Space Science Reviews* 85.1-2, pp. 161–174.

Grigahcène, A et al. (2005). “Convection-pulsation coupling-I. A mixing-length perturbative theory”. In: *Astronomy & Astrophysics* 434.3, pp. 1055–1062.

Heiter, U et al. (2002). “New grids of ATLAS9 atmospheres I: Influence of convection treatments on model structure and on observable quantities”. In: *Astronomy & Astrophysics* 392.2, pp. 619–636.

Henyey, LG et al. (1959). “A Method for Automatic Computation of Stellar Evolution.” In: *The Astrophysical Journal* 129, p. 628.

Herwig, Falk (2004). "Evolution and yields of extremely metal-poor intermediate-mass stars". In: *The Astrophysical Journal Supplement Series* 155.2, p. 651.

Houdek, G. et al. (Nov. 1999). "Amplitudes of stochastically excited oscillations in main-sequence stars". In: *Astronomy & Astrophysics* 351, pp. 582–596. eprint: `astro-ph/9909107`.

Iben Jr, Icko (1967). "Stellar evolution within and off the main sequence". In: *Annual Review of Astronomy and Astrophysics* 5.1, pp. 571–626.

Iglesias, Carlos A & Forrest J Rogers (1996). "Updated OPAL opacities". In: *The Astrophysical Journal* 464, p. 943.

Kippenhahn, Rudolf, Alfred Weigert, & Achim Weiss (1990). *Stellar structure and evolution*. Vol. 192. Springer.

Kjeldsen, Hans & Timothy R Bedding (2011). "Amplitudes of solar-like oscillations: a new scaling relation". In: *Astronomy & Astrophysics* 529, p. L8.

Koch, David G et al. (2010). "Kepler mission design, realized photometric performance, and early science". In: *The Astrophysical Journal Letters* 713.2, p. L79.

Lenz, Patrick (2009). "Pulsation models of selected delta Scuti stars". PhD thesis. Universität Wien.

Lenz, P et al. (2008). "An asteroseismic study of the $\delta$ Scuti star 44 Tauri". In: *Astronomy & Astrophysics* 478.3, pp. 855–863.

Lenz, P et al. (2010). "A $\delta$ Scuti star in the post-MS contraction phase: 44 Tauri". In: *Astronomy & Astrophysics* 509, A90.

Lesaffre, Pierre et al. (2006). "The C flash and the ignition conditions of Type Ia supernovae". In: *Monthly Notices of the Royal Astronomical Society* 368.1, pp. 187–195.

Matthews, Jaymie M (2007). "One small satellite, so many light curves: Examples of delta Scuti asteroseismology from the MOST space mission^ 1". In: *Communications in Asteroseismology* 150, p. 333.

McNamara, DH & JM Powell (1985). "RELATIONS BETWEEN (FE/H) AND DELTA-M 1 FOR F AND EARLY-G STARS." In: *Publications of the Astronomical Society of the Pacific* 97.597, p. 1101.

Michel, Eric et al. (2008). "First asteroseismic results from CoRoT". In:

Murphy, Simon J et al. (2019). "Gaia-derived luminosities of Kepler A/F stars and the pulsator fraction across the $\delta$ Scuti instability strip". In: *Monthly Notices of the Royal Astronomical Society.*

Nendwich, Johannes et al. (2004). "Interpolation of Stellar Model Grids and Application to the NEMO Grid". In: *arXiv preprint astro-ph/0406381.*

Nordlund, Å & RF Stein (1990). "3-D simulations of solar and stellar convection and magnetoconvection". In: *Computer Physics Communications* 59.1, pp. 119–125.

Paczynski, B (1969). “Envelopes of red supergiants”. In: *Acta Astronomica* 19, p. 1.

Palla, Francesco & Isabelle Baraffe (2005). “Pulsating young brown dwarfs”. In: *Astronomy & Astrophysics* 432.2, pp. L57–L60.

Pamyatnykh, AA (2000). “Pulsational instability domain of Delta Scuti variables”. In: *arXiv preprint astro-ph/0005276*.

Paxton, Bill (2004). “EZ to evolve ZAMS stars: A program derived from Eggleton’s Stellar Evolution Code”. In: *Publications of the Astronomical Society of the Pacific* 116.821, p. 699.

Paxton, Bill et al. (2013). “Modules for experiments in stellar astrophysics (MESA): planets, oscillations, rotation, and massive stars”. In: *The Astrophysical Journal Supplement Series* 208.1, p. 4.

Paxton, Bill et al. (2015). “Modules for experiments in stellar astrophysics (MESA): binaries, pulsations, and explosions”. In: *The Astrophysical Journal Supplement Series* 220.1, p. 15.

Paxton, Bill et al. (2018). “Modules for Experiments in Stellar Astrophysics (): Convective Boundaries, Element Diffusion, and Massive Star Explosions”. In: *The Astrophysical Journal Supplement Series* 234.2, p. 34.

Paxton, Bill et al. (2019). “Modules for Experiments in Stellar Astrophysics (MESA): Pulsating Variable Stars, Rotation, Convective Boundaries, and Energy Conservation”. In: *arXiv preprint arXiv:1903.01426*.

Paxton, Bill et al. (2010). “Modules for experiments in stellar astrophysics (MESA)”. In: *The Astrophysical Journal Supplement Series* 192.1, p. 3.

Pols, Omno R et al. (1995). “Approximate input physics for stellar modelling”. In: *Monthly Notices of the Royal Astronomical Society* 274.3, pp. 964–974.

Potekhin, Alexander Y & Gilles Chabrier (2010). “Thermodynamic functions of dense plasmas: analytic approximations for astrophysical applications”. In: *Contributions to Plasma Physics* 50.1, pp. 82–87.

Preston, George W (1974). “The chemically peculiar stars of the upper main sequence”. In: *Annual review of astronomy and astrophysics* 12.1, pp. 257–277.

Rogers, FJ & A Nayfonov (2002). “Updated and expanded OPAL equation-of-state tables: implications for helioseismology”. In: *The Astrophysical Journal* 576.2, p. 1064.

Royer, F, J Zorec, & AE Gómez (2004). “Rotational velocity distributions of A-type stars”. In: *Proceedings of the International Astronomical Union* 2004.IAUS224, pp. 109–114.

Samadi, R., M.-J. Goupil, & G. Houdek (Nov. 2002). “Solar-like oscillations in delta Scuti stars”. In: *Astronomy & Astrophysics* 395, pp. 563–571. eprint: `astro-ph/0208573`.

Saumon, D, G Chabrier, & HM Van Horn (1995). "An equation of state for low-mass stars and giant planets". In: *The Astrophysical Journal Supplement Series* 99, p. 713.

Seaton, MJ & Nigel R Badnell (2004). "A comparison of Rosseland-mean opacities from OP and OPAL". In: *Monthly Notices of the Royal Astronomical Society* 354.2, pp. 457–465.

Shibahashi, Hiromoto (1979). "Modal analysis of stellar nonradial oscillations by an asymptotic method". In: *Publications of the Astronomical Society of Japan* 31, pp. 87–104.

Smalley, B et al. (2011). "SuperWASP observations of pulsating Am stars". In: *Astronomy & Astrophysics* 535, A3.

Solano, E & J Fernley (1997). "Spectroscopic survey of $\delta$ Scuti stars-I. Rotation velocities and effective temperatures". In: *Astronomy and Astrophysics Supplement Series* 122.1, pp. 131–147.

Starrfield, Sumner et al. (2000). "The effects of new nuclear reaction rates and opacities on hydrodynamic simulations of the nova outburst". In: *The Astrophysical Journal Supplement Series* 127.2, p. 485.

Timmes, Frank X & F Douglas Swesty (2000). "The accuracy, consistency, and speed of an electron-positron equation of state based on table interpolation of the Helmholtz free energy". In: *The Astrophysical Journal Supplement Series* 126.2, p. 501.

Townsend, RHD, J Goldstein, & EG Zweibel (2017). "Angular momentum transport by heat-driven g-modes in slowly pulsating B stars". In: *Monthly Notices of the Royal Astronomical Society* 475.1, pp. 879–893.

Townsend, RHD & SA Teitler (2013). "GYRE: an open-source stellar oscillation code based on a new Magnus Multiple Shooting scheme". In: *Monthly Notices of the Royal Astronomical Society* 435.4, pp. 3406–3418.

Townsend, Richard (2013). *Gyre*. `https://bitbucket.org/rhdtownsend/gyre/wiki/Home`. [Online; accessed 13-November-2018].

Trampedach, Regner & Robert F Stein (2011). "The mass mixing length in convective stellar envelopes". In: *The Astrophysical Journal* 731.2, p. 78.

Turcotte, S. et al. (Aug. 2000). "The effect of diffusion on pulsations of stars on the upper main sequence — $\delta$ Scuti and metallic A stars". In: *Astronomy & Astrophysics* 360, pp. 603–616. eprint: `astro-ph/0006272`.

Walker, Gordon et al. (2003). "The MOST asteroseismology mission: Ultraprecise photometry from space". In: *Publications of the Astronomical Society of the Pacific* 115.811, p. 1023.

Wanner, Gerhard & Ernst Hairer (1996). *Solving ordinary differential equations II*. Springer Berlin Heidelberg.

Weiss, Achim & Helmut Schlattl (2008). "GARSTEC—the Garching Stellar Evolution Code". In: *Astrophysics and Space Science* 316.1-4, pp. 99–106.

Weiss, Achim et al. (2004). “Cox and Giuli’s Principles of Stellar Structure”. In: *Cox and Giuli’s Principles of Stellar Structure, by A. Weiss, W. Hillebrandt, HC. Thomas, H. Ritter. Cambridge, UK: Cambridge Scientific Publishers Ltd, 2004.*

Young, Patrick A & David Arnett (2005). “Observational tests and predictive stellar evolution. II. Nonstandard models”. In: *The Astrophysical Journal* 618.2, p. 908.

Zima, Wolfgang et al. (2007). “High-resolution spectroscopy of the $\delta$ Scuti star 44 Tauri: photospheric element abundances and mode identification”. In: *Astronomy & Astrophysics* 471.1, pp. 237–245.